December 11, 2018

Search for supersymmetry with the ATLAS detector using the recursive jigsaw technique in zero lepton final states.

Anum Qureshi
Supervisor : Assoc. Prof. Paul Jackson
Department of Physics, University Of Adelaide

A thesis presented for the Doctor of Philosophy in
Experimental High Energy Physics.

Contents

List of Figures

List of Tables

Abstract

In this thesis, I have presented the search for supersymmetry (SUSY) in Run II data at 13 TeV centre-of-mass energy using the ATLAS detector at the CERN Large Hadron Collider. SUSY searches are described using the supersymmetric partners of quarks (squarks) and gluons (gluinos). Firstly, prospects and then results are shown for an inclusive search for squark and gluino production in hadronic final states using the Recursive Jigsaw technique of variable construction. This novel method is described and simulation studies illustrate potential sensitivity to SUSY in signatures involving jets and missing transverse momentum. Benchmark points for squark and gluino pair production are studied for models with large mass splittings as well as with compressed spectra.

I certify that this work contains no material which has been accepted for the award of any other degree or diploma in my name, in any university or other tertiary institution and, to the best of my knowledge and belief, contains no material previously publish ed or written by another person, except where due reference has been made in the text. In addi tion, I certify that no part of this work will, in the future, be used in a submission in my name, for any other degree or diploma in any university or other tertiary institution without the prior approval of the University of Adelaide and where applicable, any partner institution responsible for the joint award of this degree. I acknowledge that copyright of published works contained within this thesis resides with the copyright holder(s) of those works. I also give permission for the digital version of my thesis to be made available on the web, via the Universitys digital research repository, the Library Search and also through web search engines, unless permission has been granted by the University to restrict access for a period of time.

Acknowlegments

I would like to express my very great appreciation for my Supervisor Dr. Paul Jackson who gave me an oppurtunity to learn and work and also for his guidance throughout. I would also like to acknowlege the University of Adelaide for the award of the Beacon Enlightenment scholarship. I would also like to thank the Department of Physics for the Southgate Fellowship travel grant which enabled me to attend the European School of High energy Physics (ESHEP). I learned Supersymmetry from Ben Allanach at this school and his lectures are frequently referenced in this work. I am grateful to all of those with whom I have had the pleasure to work during this thesis. Escpecially I would like to mention Damir who had to endure my questions and random musings.

I would like to mention my family who have always supported me with their love and encouragements. Your belief in me has always kept me strong. So thank you for that.

In the end, I wish to thank my husband, Jawad. Without his love, commitment and support, this would not have been possible. Though they were tiring and stressful, I will always remember these times. And my daughter Duaa, whose smile just lightens up my world and makes everything better.

To my family.

"Remember to look up at the stars and not down at your feet. Try to make sense of what you see and wonder about what makes the universe exist."

Stephen Hawking

Chapter 1

Introduction

Until now everything in the universe consists of a few basic building blocks called the fundamental particles with four forces governing them. The Standard Model of particle physics provides the best understanding of how these particles and forces (except for gravity) interact. It successfully explains all experimental results to date [1]. Modern day detectors have discovered everything that the Standard Model predicted and in many cases to a very high level of accuracy. The Higgs boson was the last gap to be filled. On fourth of July 2012, the CMS and the ATLAS collaborations announced that they had observed a new particle around the mass of 126 GeV, where the Higgs boson was predicted to be by the supersymmetric extensions of the Standard Model [2]. This particle has been found to be consistent with the Higgs boson's properties.

However, the Standard Model does not explain everything and there remain mysteries in the universe which still need to be tackled. For example, it does not include gravity, it does not explain the mass difference of the three

generation of quarks which is of approximately four orders of magnitudes and it also does not provide any candidate for the Dark Matter. Dark Matter is a non-luminous, non-reacting matter that constitutes 80% of the gravitating matter in the universe. For these reasons we believe that physics beyond the Standard Model exists at the TeV energy scale and using advanced detector techniques our goal is to search for the evidence of it's nature.

SUSY is one plausible extension of the Standard Model which attempts to rectify some of the failings identified above. In Chapter 3, I have discussed in detail these unexplained behaviors and their possible theoretical solutions given by SUSY.

In Part II, the Large Hadron Collider (LHC) and the ATLAS detector are outlined. Since June 2015, the LHC has started it's second run at 13 TeV centre-of-mass energy. The resulting data is studied and analyzed to find evidence for new physics beyond Standard Model. A section on ATHENA is included here, which is the framework for writing programming code in ATLAS. For my qualification task at ATLAS, I wrote a C++ code for a tool which is used in τ truth matching by the τ working group at ATLAS. This code basically parses the truth container for taus, creating a new "Truth-Taus" container plus decorating useful information like the visible four momentum. It also matches reconstructed taus to the truth taus from the new container connecting them via element links.

Our research group at the University of Adelaide is a part of a group of

scientists doing analysis studies on SUSY with the data collected by the ATLAS experiment at the LHC. Part III is dedicated software discussion that is used in my analysis. Detail description of a technique called the Recursive Jigsaw technique is given that is used exclusively by our physics analysis group. This method gives potential sensitivity to SUSY in signatures involving jets and missing transverse energy. Supersymmetric signal searches are done by looking for evidence for the existence of squarks and gluinos, which are supersymmetric partners of Standard Model particles quarks and gluons. Squark and gluino pair production for models with large mass splitting as well as compressed spectra are studied.

Part IV concludes with the exclusion reach discussion achieved by the analysis using the Recursive Jigsaw Technique.

Part I

Theoretical Framework

Chapter 2

The Standard Model

Standard model (SM) is a description of elementary particles and their interactions considered elegantly beautiful by the theorists because of it's mathematical foundation on quantum field theory (QFT). QFT incorporates quantum mechanics and special relativity in a consistent framework [3]. The fundamental entities are quantum fields and their excitations correspond to physically observable elementary particles which are the basic constituents of matter as well as the mediators of all the known interactions. It has been impressively experimentally accurate as well. In 2008, the measurement of the magnitude of electron magnetic dipole moment, the difference between the measured and predicted value was found to be less than 0.28 parts per trillion (10^{12}) [4]. The SM treats particles act as point-like down to the limit 10^{-18}m [5]. They have an internal angular momentum quantum number called "spin". The spin value quantifies particles as either "fermions" with spin in half integers or "bosons" with integer spins. Bosons and fermions have very different physical behaviour and physical properties. The main differ-

ence comes from the fact that fermions satisfy the Pauli exclusion principle, which states that two identical fermions cannot occupy the same quantum state, and therefore explaining the vast diversity of atoms while bosons can occupy the same quantum state. The SM postulates that all known Universe can be built from twelve fundamental fermions and twelve anti-fermions and interactions among them which are mediated by the bosons.

2.1 Particle content of the Standard Model

Particle physics was born with the discovery of the electron by J.J. Thomson in 1897 [6]. He correctly surmised that electron was a part of the atom and to explain the neutrality of atoms, he theorized that electrons were embedded in atom like plums in a pudding [7]. This was later corrected by Rutherford who discovered the proton as the central positive charge. Since only protons could not justify the mass of the nucleus, the neutron was proposed and discovered by Chadwick in 1932 [7]. It was then considered that all matter was composed of electrons, protons and neutrons and that was it. But what held the positively charged mutually repelling protons together in the nucleus? Yukawa proposed a particle 300 times heavier than an electron and one sixth of the mass of the proton which was exchanged between the neutron and proton. This particle would be the strong force mediator. The muon μ and later the pion π, which were discovered from the cosmic radiations, were thought at that time to be the Yukawa's "mesons" (medium weight particles) [8]. Antiparticles which were proposed as the "positive energy states of an oppositely charged particle" solution to the

Dirac's negative energy states and were discovered shortly later by Anderson from tracks left in a cloud chamber [9]. Neutrinos were theorized to be the invisible thief responsible for the missing energy in the beta decay [10].

Again with the discovery of Yukawa's meson, Dirac's antiparticles and Pauli's neutrinos, it was thought that elementary particle physics was all but finished. But with the start of the modern accelerator physics, a whole new plethora of particles were found. Gell-Mann used the "The Eightfold Way" to arrange the baryons (the heavy weight particles) and the mesons in octets and decuplets according to their charge and strangeness [11]. Now the question arose "why these bizarre patterns?". The quark model with it's three generations provided the answer. All Eightfold way supermultiplets can be made from the quark model quite naturally. The quark model was highly objectionable because it did not satisfy Pauli's exclusion principle and also no quark was ever seen. It was the discovery of the J/ψ particle in 1974 and it's successful explanation given by the quark model that restored the faith in it. It is now a well established theory. Since we are now exploring totally uncharted energy scales, we could discover absolutely anything.

For the force mediators; the photon was very controversial at the beginning because nobody wanted to believe in it when the wave nature of light was well established and Einstein for over 20 years fought a lonely battle for the light quantum. But eventually in face of undeniable evidence it had to be accepted [7]. On the other hand, the $W^{\pm}$ and the Z bosons, seen by the UA(1) experiment at CERN in 1983 [12], were widely accepted. They proved the unification of electroweak theory and were considered a "sigh of relief" [7].

The Higgs particle, the theorized scalar spin 0 boson, was discovered on 4 July, 2012 around a mass of around 125 GeV [2].

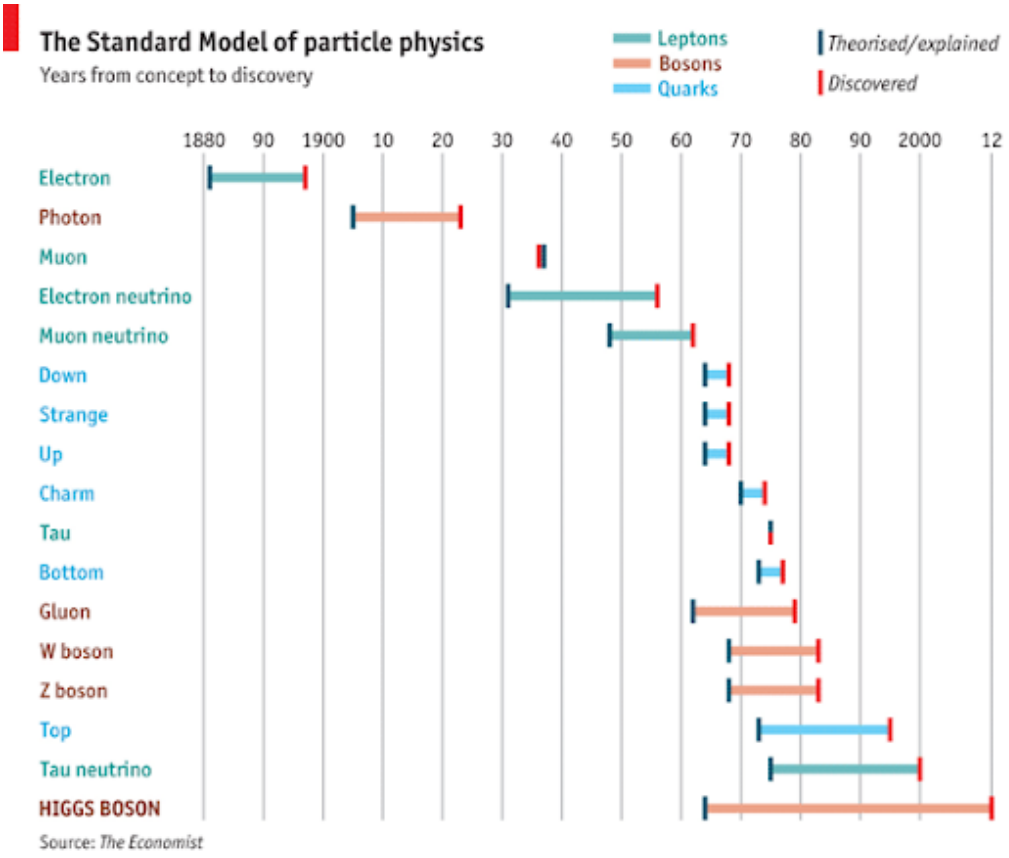

Figure 2.1: A timeline of the SM of particle physics [14].

Table 2.1: The SM fermions, spin-1/2 particles, with their corresponding masses taken from [15].

Leptons	Mass	Charge	Quarks	Mass	Charge
electron e	0.511 MeV	-1	up u	2.2 MeV	$+\frac{2}{3}$
e neutrino	< 2 eV	0	down d	4.87 MeV	$-\frac{1}{3}$
muon μ	105.658 MeV	-1	charm c	1.275 GeV	$+\frac{2}{3}$
μ neutrino	< 2 eV	0	strange s	95 MeV	$-\frac{1}{3}$
tau τ	1776.86 MeV	-1	top t	173.07 GeV	$+\frac{2}{3}$
τ neutrino	< 2 eV	0	bottom b	4.18 GeV	$-\frac{1}{3}$

Table 2.2: The SM bosons, integer spin particles with their corresponding properties taken from [15]

Particle	Mass	Charge	Spin
photon γ	$< 1 \times 10^{-18} eV$	0	1
W	80.370 GeV	± 1	1
Z	91.1876 GeV	0	1
gluon g	0	0	1
Higgs H	125.18	0	0

2.2 The gauge theory of the Standard Model

The QFT theory of SM, follows the gauge principle of invariance; localization of a global symmetry to obtain an interaction term from a free Lagrangian

which remains invariant under the symmetry transformation. This results in the inclusion of additional fields with appropriate kinetic and interactions terms in the action. This principle is used to describe the behaviours of elementary particles and the forces governing them.

2.2.1 Symmetries

Symmetries are a tool to learn about the QFT framework of the SM. A symmetry is a transformation that leaves the physical observable of a system unchanged. They play a very important role in understanding nature.

There are two general types of symmetries:

- Space-time Symmetries: These symmetries correspond to transformations on a field theory acting explicitly on the space-time coordinates:

$$x^{\mu} = x'^{\mu}(x^{\nu}) \tag{2.1}$$

  where $\mu,\ \nu = 0,1,2,3,4$.

  "Poincare" transformations (rotations and translations Lie group) defining special relativity and "general transformations" in general relativity are examples.

- Internal Symmetries: These are symmetries that correspond to transformations of the different fields in a QFT:

$$\phi^{a}(x) = M^{a}_{b}\phi^{b}(x) \tag{2.2}$$

  If M^{a}_{b} is a constant this is a "global symmetry" if it is space-time dependant this is a "local" symmetry. [3]

Symmetries are important because they:

- Define an elementary particle according to the behaviour of the different conserved quantum number under the transformations from the different symmetries like mass, spin, charge, colour, etc. This is the result of the "Noether Theorem" which states that each continuous symmetry implies a conserved quantity.

- Can determine the interaction among different particles based on the "gauge principle" like for instance if the theory is renormalizable or not.

- Can be hidden, the existence of hidden symmetries implies that the fundamental symmetries of nature may be huge despite the fact that we observe a limited amount of symmetry. This is because the only manifested symmetries we can observe are the symmetries of the vacuum we live in and not those of the full underlying theory. This opens-up an essentially unlimited resource to consider physical theories with an indefinite number of symmetries even though they are not explicitly realized in nature [3].

- Can be spontaneously broken. Consider the potential $V(\phi, \phi^*)$ of the form:

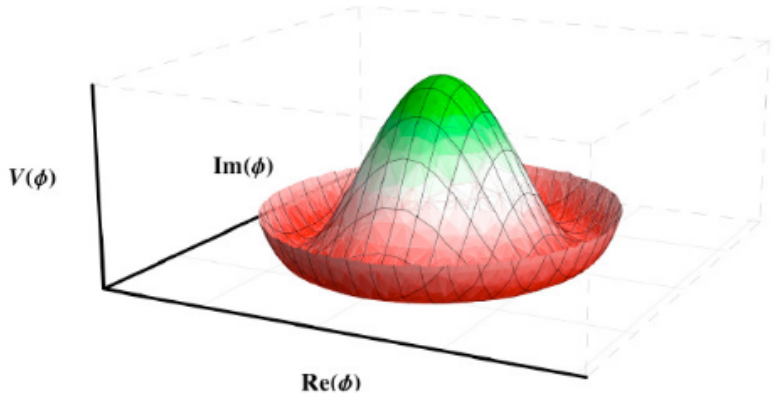

Figure 2.2: The Mexican hat potential for V = (a - bϕ^2)^2 [3].

If $V(\phi, \phi^*)$ is of the form $V(|\phi|^2)$, then it would be symmetric under the global symmetry $\phi \rightarrow exp(i\alpha)\phi$. This potential is written as:

$$V = a|\phi|^2 + b|\phi|^4 \text{ where } a,\ b\ \geq\ 0; \tag{2.3}$$

The minimum of this potential is at $< \phi > = 0$ and so is the vacuum expectation value.

If the potential is of the form:

$$V = (a - b|\phi|^2)^2 \text{ where } a,\ b\ \geq\ 0; \tag{2.4}$$

The ground state is not at zero, the symmetry on V is lost [3].

2.2.2 Quantum Electrodynamics; the theory of light

This theory deals with the interaction of charged leptons with the photons. The inception of Quantum Electrodynamics (QED) was the need for

scientists to reconcile Maxwell's equations with the quantum theory developed during the early twentieth century by Dirac [16], Heisenberg [17] and Pauli [18]. But all of them couldn't resolve the infinities occurring in the mathematical equations until Feynman developed renormalization and his renowned Feynman's rules [7].

To develop QFT for the photons, let's start with the Dirac Equation and develop a Lagrangian for the electrodynamics theory. Maxwell's equations result directly in a non-radiative environment. Dirac equation is given as:

$$i\hbar\gamma^{\mu}\partial_{\mu}\psi - mc\psi = 0 \tag{2.5}$$

where ψ is a four-element column matrix:

$$\psi = \begin{pmatrix} \psi_1 \\ \psi_2 \\ \psi_3 \\ \psi_4 \end{pmatrix} \tag{2.6}$$

called a "Dirac spinor".

Free point charges of spin 1/2 and momentum p = (E/c,$\mathbf{p}$), where E $=\sqrt{m^2c^4 + \ \mathbf{p}^2c^2}$ are represented by wave functions [7]:

Particle	**Antiparticle**
$\psi = ae^{-(i/\hbar)p.x}u^{(s)}(p)$	$\psi = ae^{(i/\hbar)p.x}v^{(s)}(p)$

(2.7)

where s = 1,2 for two states of spin for fermions.

The spinors $u^{(s)}$ and $v^{(s)}$ are orthogonal,

$$u^{\bar{(1)}}u^{(2)} = 0 \qquad v^{\bar{(1)}}v^{(2)} = 0 \tag{2.8}$$

(where $\bar{u} = \dagger u\gamma^0$ and $\bar{v} = \dagger v\gamma^0$)

normalized

$$u\bar{u} = 2mc \qquad v\bar{v} = -2mc \tag{2.9}$$

and show completeness:

$$\sum_{s=1,2} u^{(s)}u^{\bar{(s)}} = (\gamma^\mu p_\mu + mc) \qquad \sum_{s=1,2} v^{(s)}v^{\bar{(s)}} = (\gamma^\mu p_\mu - mc) \tag{2.10}$$

Let's define an anti-symmetric relativistic tensor $F_{\mu\nu}$ in such a way that it is composed of components of electric field $\mathbf{E}$ and magnetic field $\mathbf{B}$:

$$F_{\mu\nu} = \begin{pmatrix} 0 & -Ex & -Ey & -Ez \\ Ex & 0 & -Bz & By \\ Ey & Bz & 0 & -Bx \\ Ez & -By & Bx & 0 \end{pmatrix} \tag{2.11}$$

This field strength tensor also satisfies the Bianchi's identity:

$$\partial_\lambda F_{\mu\nu} + \partial_\mu F_{\nu\lambda} + \partial_\nu F_{\lambda\mu} = 0 \tag{2.12}$$

This identity gives two of the Maxwell's equations:

$$\Delta.\overrightarrow{B} = 0 \text{ and } \frac{\partial \overrightarrow{B}}{\partial t} = -\Delta \times \overrightarrow{E} \tag{2.13}$$

The $\overrightarrow{B}$ and $\overrightarrow{E}$ can be written in the form of the vector potential $A_\mu = (\phi, \overrightarrow{A})$, then $F_{\mu\nu}$ can be defined as

$$F_{\mu\nu} = \frac{\partial A_\nu}{\partial x_\mu} - \frac{\partial A_\mu}{\partial x_\nu} \tag{2.14}$$

Now if we determine a four-vector with charge density ρ and a current density $\mathbf{J}$:

$$J^\mu = (c\rho, \mathbf{J}) \tag{2.15}$$

One can get the remaining two Maxwell's equation by taking the derivative of the $F_{\mu\nu}$ tensor

$$\frac{\partial F_{\mu\nu}}{\partial x_\nu} = \frac{J_\mu}{c} \tag{2.16}$$

$$\Delta.\overrightarrow{E} = \rho \text{ and } \frac{\partial \overrightarrow{E}}{\delta t} = \Delta \times \overrightarrow{B} \tag{2.17}$$

In QED, A_μ becomes the representative field for photons. For a free photon, the current J_μ goes to zero and we can say from Eq. 2.11 that

$$\Box A^\mu = 0 \tag{2.18}$$

A plane wave solution for the above equation is given as

$$A^\mu(x) = ae^{-(i/\hbar)p.x}\epsilon^\mu(p) \tag{2.19}$$

Here ϵ is the polarization vector, since the photon is a massless particle it has two spin states and only two degrees of freedom.

Thus the free Lagrangian in the absence of any sources or interactions is given by

$$\mathscr{L} = -\frac{1}{4}F^{\mu\nu}F_{\mu\nu} \tag{2.20}$$

If we want to interact light with matter we introduce an A_μ coupling to either scalars or spinors. Something like this:

$$\mathscr{L} = -\frac{1}{4}F^{\mu\nu}F_{\mu\nu} - J_\mu A^\mu \tag{2.21}$$

where J_μ contains the functions for interacting matters. Equation of motion from above equation would be:

$$\partial_\mu F^{\mu\nu} = J_\nu \tag{2.22}$$

which gives us the conserved current $\partial^\mu J_\mu = 0$.

The Lagrangian from Dirac spinors is given as

$$\mathscr{L} = \bar{\psi}(i\gamma^\mu\partial_\mu - m)\psi \tag{2.23}$$

where ψ has gauge symmetry $\psi = \psi e^{-i\alpha}$ and $\bar{\psi} = \bar{\psi}e^{i\alpha}$ where $\alpha \in R$. This yields the conserved current $J^\mu = \psi\gamma^\mu\psi$. So the Lagrangian with interacting light and electrons is given as

$$\mathscr{L} = -\frac{1}{4}F^{\mu\nu}F_{\mu\nu} + \bar{\psi}(i\gamma^\mu\partial_\mu - m)\psi - e\bar{\psi}\gamma^\mu A_\mu\psi \tag{2.24}$$

where e is a coupling constant. This Lagrangian is invariant under gauge transformations where $A_\mu \to A_\mu + \partial_\mu\lambda$ and $\psi \to \psi e^{-ie\lambda}\psi$ for an arbitrary function $\lambda(x)$. We can prove that by defining a new term called the "covariant derivative" such as $D_\mu = \partial_\mu + ieA_\mu$.

$$D_\mu\psi \to \partial_\mu(e^{-ie\lambda}\psi) + ie(A_\mu + \partial_\mu\lambda)(e^{-ie\lambda}) = e^{ie\lambda}D\psi \tag{2.25}$$

The covariant derivative has picked up a phase but we see that the Lagrangian is invariant since D is sandwiched between ψ and $\bar{\psi}$ and $\bar{\psi}$ transforms as $\bar{\psi} = e^{ie\lambda(x)}\bar{\psi}$. Finally the compact QED Lagrangian written in terms of covariant derivative is:

$$\mathscr{L} = -\frac{1}{4}F^{\mu\nu}F_{\mu\nu} + \bar{\psi}(iD - m)\psi \tag{2.26}$$

Since this Lagrangian does not change under phase transformations it is U(1) gauge symmetric under QED.

2.2.3 Quantum Chromodynamics; the theory with colours

In Quantum Chromodynamics (QCD), quarks, the coloured fermions, interact through gluons. Since gluons have the same role of propagators as photons in QED, they are represented by the coloured four-vector potential A^a_μ here. The a index is for the colour factor and ranges from 1-3. We have the same fermionic Lagrangian but now the fermions transform as

$$\psi^i_b \to \psi^i_c e^{-i(\frac{\lambda^a}{2}.\theta(x)^a)} \tag{2.27}$$

where $\theta(x)^a$ is a real function with a = 1,2, ... 8 and $\lambda^a_{bc}/2$ are the generators for the SU(3) group symmetry. These are called Gell-Mann matrices after his extensive efforts in QCD [7]. Apart from colours, QCD also has six flavours $i = u, d, c, s, t, b$.

The "covariant derivative" then transforms as

$$D_\mu = \partial_\mu + ig_s\frac{\lambda^a}{2}A^a_\mu \tag{2.28}$$

where g_s is the coupling constant for strong force.

The field strength tensor also gets an extra term

$$F^a_{\mu\nu} = \frac{\partial A^a_\nu}{\partial_\mu} - \frac{\partial A^a_\mu}{\partial_\nu} + g_s f^a_{bc} A^b_\mu A^c_\nu \tag{2.29}$$

This term comes from trying to make the source free Lagrangian $\mathscr{L} = -\frac{1}{4} F^{\mu\nu}_a F^a_{\mu\nu}$ invariant under the SU(3) gauge. This extra term gives the gluons self interactions through three or four point vertices. Because gluons carry colour, their self interactions are the source of all the key differences between QCD and QED such as colour confinement i.e only colour singlet states can exist. It is this phenomena that causes quarks to hadronize to form baryons and mesons. The asymptotic freedom is another specialty of QCD which states that the interaction strength g_s between quarks becomes smaller as the distance between them gets shorter. This happens because of self interacting gluons anti-screening effects at short distances.

The term f^a_{bc} are called the structure constants and come from the commutations relations between Gell-Mann's matrices

$$[\frac{\lambda_a}{2}, \frac{\lambda_b}{2}] = i f^a_{bc} \frac{\lambda_c}{2} \tag{2.30}$$

The structure constants are anti-symmetric and we have 8 x 8 x 8 structure constants in total. But most of them are zero and the rest are:

$$\begin{aligned} f^1_{23} = 1, \qquad f^1_{47} = f^2_{46} = f^2_{57} = f^3_{45} = f^5_{16} = f^6_{37} = \frac{1}{2} \\ f^4_{58} = f^6_{78} = \frac{\sqrt{3}}{2} \end{aligned} \tag{2.31}$$

The full QCD Lagrangian is then written as

$$\mathscr{L}_{QCD} = -\frac{1}{4} F^{\mu\nu}_a F^a_{\mu\nu} + \bar{\psi}^i_c (i \not{D}_\mu - m_q) \psi^i_b - \frac{1}{2} g_s (\partial_\mu A^a_\mu)^2 \tag{2.32}$$

where $\not{D}_\mu$ is the covariant derivative mentioned in Eq.2.28. This Lagrangian is invariant under SU(3) symmetry and describes three equal mass Dirac fields which are the three colours of the same flavour, interacting with eight massless vectors.

2.2.4 The broken Symmetry of ElectroWeak theory

There are six leptons in the SM, which can be placed into three generations:

$$\begin{pmatrix} e \\ \nu_e \end{pmatrix}, \begin{pmatrix} \mu \\ \nu_\mu \end{pmatrix}, \begin{pmatrix} \tau \\ \nu_\tau \end{pmatrix} \tag{2.33}$$

There is the electron (e), muon (μ), and tau (τ), each of which has an associated neutrino (ν_e;ν_μ;ν_τ). Each of the leptons has an electromagnetic charge = -1, while the neutrinos all have $q_{EM} = 0$. Often in an experimental context, lepton is used to denote the stable electron and metastable muon, due to their clean experimental signatures. Taus are often treated separately, due to their significantly shorter lifetime of $\tau \sim 10^{-13}$ seconds. There are also six quarks in the SM : up, down, charm, strange, top, and bottom. Quarks are similarly organized into three generations:

$$\begin{pmatrix} u \\ d \end{pmatrix}, \begin{pmatrix} c \\ s \end{pmatrix}, \begin{pmatrix} t \\ b \end{pmatrix} \tag{2.34}$$

These are often distinguished as "up-type" quarks and "down-type" quarks at the high energies of LHC. Each up-type quark has charge $q_{EM} = 2/3$, while the down-type quarks have q_{EM} = -1/3.

All quarks and leptons carry a weak charge. In 1954, Chen Ning Yang and Robert Mills used Non-Abelian groups to describe the strong and weak

force but it was clear that the Yang-Mills equations describe massless spin one particles [19]. Glashow [20] showed that the disparity between electromagnetic and weak forces can be overcome by introducing extremely massive mediating particles. But following the pattern of local gauge invariance from the previous sections, the coupling of the three SU(2) $W_{\mu}^{1,2,3}$ bosons and U(1) boson B_{μ} we get massless gauge bosons not massive ones.

$$L = -\frac{1}{4}W_{a}^{\mu\nu}W_{\mu\nu}^{a} - \frac{1}{4}B^{\mu\nu}B_{\mu\nu} + \bar{\psi}(i\gamma^{\mu}D_{\mu} - m)\psi \tag{2.35}$$

where the $W^{\mu\nu}$ are the three (a = 1,2,3) gauge bosons associated with the SU(2) symmetry group for the weak force and $B_{\mu\nu}$ is the one gauge boson for the electromagnetic force from U(1) gauge group. The covariant derivative is given as

$$D_{\mu} = \partial_{\mu} - ig_{w}\sigma_{a}.W_{\mu}^{a} - ig_{Y}Y.B_{\mu} \tag{2.36}$$

where g_w and g_y are the coupling constants for $SU(2)_L$ and $U(1)_Y$ giving us the $SU(2)_L \times U(1)$ symmetry, the subscript here points to the fact that weak force just involves left handed particles that form doublets under the $SU(2)_L$. The singlet right handed particles are left alone under the weak force. The W_{μ} are zero for right handed eigenstates. The field strengths of $B_{\mu\nu}$ and $W_{\mu\nu}^{a}$ are given by

$$\begin{aligned} B_{\mu\nu} &= \partial_{\mu}B_{\nu} - \partial_{\nu}B_{\mu} \\ W_{\mu\nu} &= \partial_{\mu}W_{\nu}^{a} - \partial_{\nu}W_{\mu}^{a} - g_{w}\epsilon^{abc}W_{\mu}^{b}W_{\nu}^{c} \end{aligned} \tag{2.37}$$

In 1964, Brout-Englert-Higgs gave the "spontaneously broken symmetry mechanism" or the "Higgs Mechanism" as it was later referred to, where they

introduced an assumption that the universe is filled with a spin-zero field, called a Higgs field, which is a doublet in SU(2) and with a nonzero U(1) hypercharge, but a singlet in colour space. The gauge bosons and fermions can interact with this field, and in this interaction they acquire mass. In this mechanism the symmetry of the Lagrangian is not broken but the symmetry of the ground state is. In 1967, Weinberg and Salam formulated Glashow's model as "spontaneously broken gauge theory" to get massive bosons [21].

The Higgs potential is written as

$$V_h = \mu^2 \phi^\dagger \phi - \lambda (\phi^\dagger \phi)^2 \tag{2.38}$$

The ground state occurs at the minimum value for this potential when $(\phi^\dagger \phi) = \frac{\mu^2}{2\lambda}$. The symmetry is spontaneously broken by the choice of the ground state. Without loss of generality, we can choose the Higgs field to point in the real direction, and write the Higgs field in the following form:

$$\phi = \frac{1}{\sqrt{2}} e^{\frac{i}{\nu}\sigma_a \theta_a} \begin{pmatrix} 0 \\ \nu + h(x) \end{pmatrix} \tag{2.39}$$

We choose a gauge to rotate away the dependence on θ_a such that we can write simply

$$\phi = \frac{1}{\sqrt{2}} \begin{pmatrix} 0 \\ \nu + h(x) \end{pmatrix} \tag{2.40}$$

If we plug V_h and ϕ back into the electroweak Lagrangian in the ground state where h(x) = 0, we get the following mass relevant terms (dropping the Lorentz indices):

$$\mathscr{L}_M = \frac{1}{8} \left| \begin{pmatrix} gW_3 + g'B & g(W_1 - iW_2) \\ g(W_1 + iW_2) & -gW_3 + g'B \end{pmatrix} \begin{pmatrix} 0 \\ \nu \end{pmatrix} \right|^2 = g^2 \nu^2 \left[W_1^2 + W_2^2 + (\frac{g'}{g} B - W_3)^2 \right] /8 \tag{2.41}$$

Defining the Weinberg's angle $\tan\theta_W = g'/g$ and the force carrying fields as:

$$\begin{aligned} W^{\pm} &= \frac{1}{\sqrt{2}}(W_1 \mp W_2) \\ Z^0 &= cos\theta_W W_3 - sin\theta_W B \\ A^0 &= sin\theta_W W_3 + cos\theta_W B \end{aligned} \tag{2.42}$$

Putting them back in the above Lagrangian we get the following masses for the bosons:

$$\begin{aligned} m_W^2 &= \frac{1}{4}\nu^2 g^2 \\ m_Z^2 &= \frac{1}{4}\nu^2(g^2 + g'^2) \\ m_A^2 &= 0 \end{aligned} \tag{2.43}$$

Then the EW Lagrangian we have discussed is given as:

$$\begin{aligned} \mathscr{L} = \partial_\mu h \partial^\mu h - \lambda\nu^2 h^2 - \lambda\nu h^3 - \frac{\lambda}{4}h^4 \\ -\big(\frac{h}{\nu} - \frac{h^2}{2\nu^2}\big)(2m_W^2 W_\mu - W^{\mu+} + m_Z^2 Z_\mu Z^\mu) \\ -\frac{1}{4}A_{\mu\nu}A^{\mu\nu} - \frac{1}{4}Z_{\mu\nu}Z^{\mu\nu} - \frac{1}{2}A^-_{\mu\nu}A^{\mu\nu+} \end{aligned} \tag{2.44}$$

The Higgs mechanism also gives mass to the fermions. The terms in the Lagrangian corresponding to the the Higgs couplings to the first generation fermions take the form:

$$\mathscr{L} = -\lambda_e \bar{l}_L^i \phi_i e_R - \lambda_d \bar{q}_L^i \phi_i d_R - \lambda_u \epsilon_{ij} \bar{q}_L^i \phi_j^* u_R + \text{hermitian conjugate} \tag{2.45}$$

where l_L and q_L are the left-handed lepton and quark doublets and e_R, d_R and u_R are the electron, d- and u-quark right-handed singlets. λ_e , λ_d and λ_u correspond to the electron, d- and u-quark Yukawa couplings of fermions with

Higgs particle and they are related to the fermion masses by $m_f = \lambda_f \nu/\sqrt{2}$. The parameter $\nu \sim 246$ GeV comes from the Higgs vacuum expectation value and is the scale responsible for all the masses of the SM particles. The Yukawa couplings are written in a diagonal format, but this is not simultaneously diagonal with the weak eigenstates. The 3x3 unitary Cabbibo-Kobayashi-Maskawa (CKM) matrix V_{mn} (where m is a quark transitioning to a n quark) is therefore introduced to translate between the quark masses and flavour bases, allowing the charged current interactions with the $W^{\pm}$ to transform flavour states. The SM gives no predictions for the Yukawa couplings.

2.3 The absolutely amazing theory of Almost Everything

Finally the SM theory describing all known particles and their interactions can be summarized as (without including flavour and colour indices):

$$\mathscr{L} = i\bar{\psi}(i\sigma^{\mu}\mathscr{D}_{\mu})\psi + h.c - \frac{1}{4}F^{\mu\nu}F_{\mu\nu} + |D_{\mu}H|^2 + \mathscr{L}_{M(B)} + \mathscr{L}_X^{int}(H) - V(H) \tag{2.46}$$

where the first term is the fermion Lagrangian with the left handed Dirac spinor members of a SU(2) doublet or the right handed singlet. D_{μ} is the appropriate covariant derivative for the SM theory. $\mathscr{L}_{\mathscr{M}(\mathscr{B})}$ includes the mass terms for the $W^{\pm}$, Z and Higgs bosons. The last two terms explain the Higgs interactions and vacuum expectation value.

SM is a beautifully eloquent theory of almost everything in nature. It has stood the test of time for almost fifty years and has been precisely mea-

sured up to next-to-next-to-leading order perturbation terms in QCD and no anomalies have been seen yet.

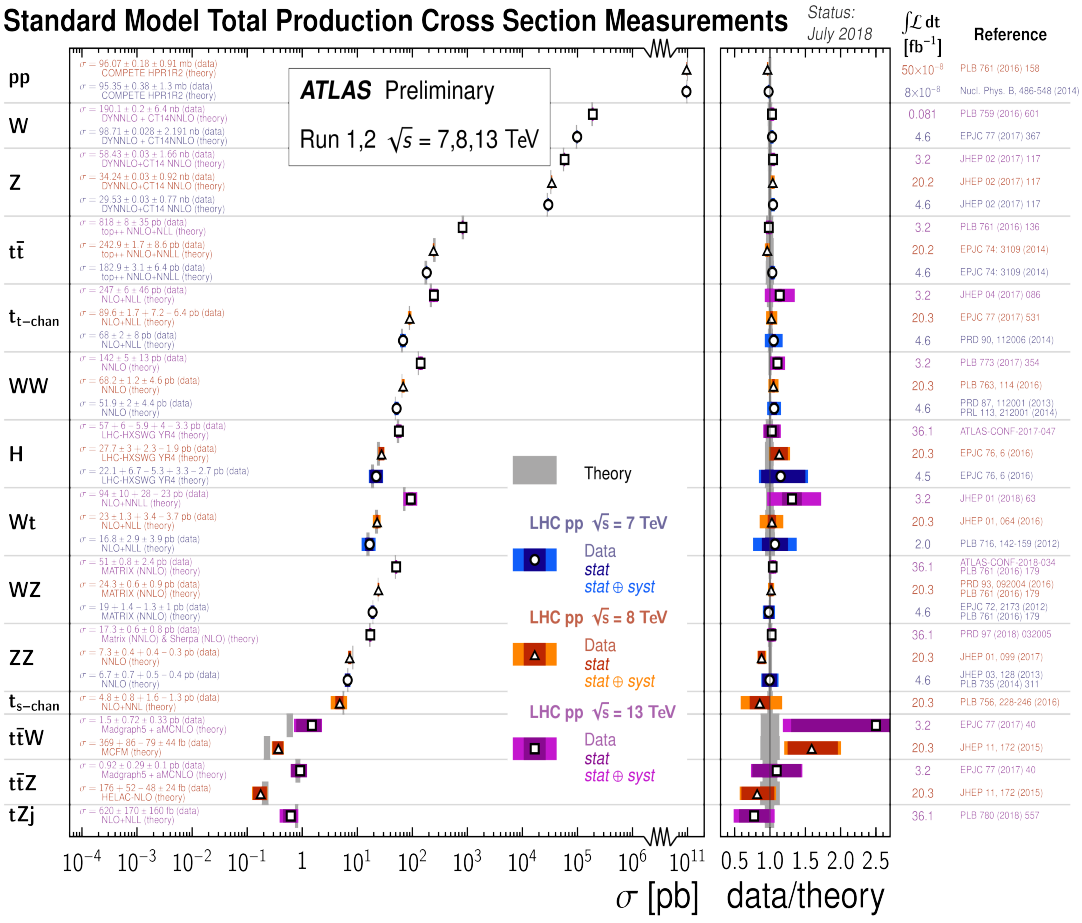

Figure 2.3: SM total production cross section measurements, corrected for leptonic branching fractions, compared to the corresponding theoretical expectations. All theoretical expectations were calculated at next-to-leading order or higher [22].

Although experimentally consistent, there are key concepts that it fails

to explain which will be discussed in the next chapter.

Chapter 3

Supersymmetry and it's Motivations

SUSY extends the Poincare symmetry of the SM in a very natural way by taking in a single multiplet with not only transformations among space-time but also among different spin states. Spin is an internal symmetry of the SM. Thus the spin 0 particles are put together in multiplets together with spin $\frac{1}{2}$ particles, spin $\frac{1}{2}$ with spin 1 and so on. SUSY defines a symmetry which relates together particle in a "superfield" with same masses and couplings but spin difference of one-half unit between them [3].

3.1 A simple supersymmetric Lagrangian

The most common superfield is the chiral superfield (also known as the Weyl superfields) which contains a complex scalar S, the two component chiral fermion ψ and the non-dynamical complex scalar F which is used to

parametrize SUSY breaking. For example a superfield for a right handed top multiplet would be $T_R = (\tilde{t}_R, t_R, F_{t_r})$ bringing together the top quark and it's supersymmetric partner the stop quark. Now since we want our supersymmetric potential to be holomorphic i.e. there is no charge conjugation so we use the Majorana fermions ζ where $\zeta^c = \zeta$ and since the F function has no kinetic term, we ignore it for now [23].

$$\begin{aligned} \mathscr{L} = -\partial_\mu S^* \partial_\mu S - i\bar{\zeta}\bar{\sigma}^\mu \partial_\mu \zeta - \frac{1}{2} m(\zeta\zeta + \bar{\zeta}\bar{\zeta}) \\ -cS\zeta\zeta - c^* S^* \bar{\zeta}\bar{\zeta} - |mS + cS^2|^2 \end{aligned} \tag{3.1}$$

where c is an arbitrary coupling constant and σ_μ are Pauli's matrices where $\bar{\sigma_\mu} = (1, -\sigma_\mu)$ [24].

This Lagrangian is invariant under supersymmetric transformations and converts bosons S into fermions ζ and *vice versa*. The scalar potential is the last term in the Lagrangian and it is positive definite. So this is an unbroken superymmteric Lagrangian with vacuum expectation value at 0.

Since we haven't observed any bosonic partners to the fermions, SUSY if it exists should be a broken symmetry. We call it "softly broken supersymmetry" because we want it to have low energy interactions that are around TeV scale.

Now we introduce another type of superfields called the "vector superfields". These consists of a massless gauge boson A_μ described by a field strength $F^A_{\mu\nu}$, a two component Majorana fermion field a "gaugino" denoted by λ_A and a non dynamical scalar D. This scalar also parametrizes SUSY breaking, "D-term supersymmetry breaking" corresponds to this D [25]. An example of gluon superfield is $G = (g, \tilde{g}, D_g)$ this multiplet combines together

the gluon and the "gluino".

3.2 The MSSM

The simple concept of SUSY is to introduce a symmetry between bosons and fermions, still observing the $SU(3) \times SU(2)_L \times U(1)_Y$ gauge symmetry, resulting in the prediction of super-partner particles that accompany the existing SM particles . The Minimal supersymmetric model (MSSM) realizes SUSY in a way that we have minimum number of super-particles states and new interactions consistent with the SUSY theory. For each particle of the SM, MSSM gives us another particle with a different spin denoted by a tilde over the particle symbol. For scalar particles of quarks and leptons we have squarks ($\tilde{q}$) and sleptons ($\tilde{e}_{\mathrm{L}}$, $\tilde{\nu}_{\mathrm{L}}$). There are squarks and sleptons for all three generations but for simplification we have just used the first generation in the Table. 3.1. The superfield Q for quarks and squarks is represented by the supermultiplet:

$$\begin{pmatrix} \text{left chiral squark SU(2) doublet } (\tilde{q}_L) \\ \text{left chiral quark SU(2) doublet } (q_L) \end{pmatrix} \tag{3.2}$$

where the left chirality is from convention.

Similarly the left handed superfield L for leptons and sleptons is given by:

$$\begin{pmatrix} \text{left chiral sleptons SU(2) doublet } (\tilde{e}_L) \\ \text{left chiral leptons SU(2) doublet } (e_L) \end{pmatrix} \tag{3.3}$$

The second and third row also show the anti-quarks $\bar{u}_R$ and their super-partners $\tilde{\bar{u}}_R$.

One important feature of the MSSM is that although the SM has one Higgs doublet, in SUSY two separate $SU(2)_L$ doublets of Majorana fermionic fields forming chiral supermultiplets called the "higgsinos" are required. Introducing one Higgs $SU(2)_L$ doublet produces anomalies in the $SU(2)_L \times U(1)_Y$ sector. We need another one with exactly opposite $U(1)_Y$ quantum numbers to cancel the first ones leaving an anomaly free theory. Two Higgs doublet are also required to give up and down type quark masses in a SUSY theory.

For fermionic super-partners of gauge bosons we have gluinos ($\tilde{g}$), $\tilde{W}^{\pm}$ and $\tilde{Z}^0$ and photinos $\tilde{\gamma}$.

Table 3.1: Chiral supermultiplet fields in the MSSM [26].

Names		spin 0	spin 1/2	$SU(3)_c$, $SU(2)_L$, $U(1)_y$
squarks, quarks	Q	$(\tilde{u}_L, \tilde{d}_L)$	(u_L, d_L)	**3**, **2**, 1/3
($\times$ 3 families)	$\bar{U}_R$	$\tilde{\bar{u}}_L(\tilde{u}_R)$	$\bar{u}_L \sim (u_R)^c$	$\bar{3}$, **1**, -4/3
	$\bar{D}_R$	$\tilde{\bar{d}}_L(\tilde{d}_R)$	$\bar{d}_L \sim (d_R)^c$	$\bar{3}$, **1**, 2/3
sleptons, leptons	L	$(\tilde{\nu}_{eL}, \tilde{e}_L)$	(ν_{eL}, e_L)	**1**, **2**, -1
($\times$ 3 families)	$\bar{E}_R$	$(\tilde{e}_R)$	$\bar{e}_L \sim (e_R)^c$	**1**, **1**, 2
higgs, higgsinos	H_u	(H_u^+, H_u^0)	$(\tilde{H}_u^+, \tilde{H}_u^0)$	**1**, **2**, 1
	H_d	(H_d^0, H_d^-)	$(\tilde{H}_d^0, \tilde{H}_d^-)$	**1**, **2**, -1

Table 3.2: Gauge supermultiplet fields in the MSSM [26].

Names	spin 1/2	spin 1	$SU(3)_c$, $SU(2)_L$, $U(1)_y$
gluinos, gluons	$\tilde{g}$	g	**8**, **1**, 0
winos and bino, W,Z bosons	$\widetilde{W}^{\pm}, \widetilde{Z}^0$	$W^{\pm}$, Z^0	**1**, **3**, 0
photino, photon	$\tilde{\gamma}$	γ	**1**, **1**, 0

The "superpotential" of the MSSM is given as

$$W_{MSSM} = \mu H_u H_d + \sum_{ij} (Y_u)_{ij} H_u Q_{L,i} \bar{U}_{R,j} + \sum_{ij} (Y_d)_{ij} H_d Q_{L,i} \bar{D}_{R,j} + \sum_{ij} (Y_{L_{ij}} H_d L_{L,i} \bar{E}_{R,j}) \tag{3.4}$$

where Y_u, Y_d and Y_L are the Yukawa coupling constants for the up type quarks, the down type quarks and the leptons respectively [27]. The first term is not of the form $H_u H_u^*$ because complex conjugation breaks the holomorphicity of the SUSY Lagrangian and hence we need two Higgs doublets.

The above mentioned potential is not the most general one for the MSSM consistent with all gauge symmetries. We could include the following operators in the superpotential:

$$W = W_{MSSM} + \alpha U_R D_R \tilde{D}_R + \beta Q_L L \tilde{D}_R \tag{3.5}$$

However, these two couplings generate the proton decay $p \to \pi^0 e^+$ which can be estimated from dimensional analysis to be

$$\tau \approx \alpha^2 \beta^2 \frac{m_{\tilde{d}_R}^5}{m_p^4} \approx (\frac{m_{\tilde{d}_R}}{1\text{TeV}})^5 10^{-10} \text{sec} \tag{3.6}$$

Since proton is experimentally proven to be stable for $\tau^{exp} > 1.4 \times 10^{34}$ years [28], then these operators in Eq.3.5 should not be included in the superpotential.

R-parity is a way to ensure these types of operators are forbidden in MSSM [27]. In this way the bosons and their superpartner fermions behave in opposite way. In MSSM, baryonic number and leptonic number is not conserved, the quantity that is conserved is R-parity. R-parity (R_p) is a discreet Z_2 symmetry defined for each particle as

$$R_p = (3B + L + 2S)^{-1}, \tag{3.7}$$

where B, L and S are the baryonic number, the leptonic number and the spin of each particle. For all SM particles R_p is +1 and for their super-partners it is equal to -1.

The conservation of R_p in SUSY results in two important consequences:

- SUSY particles are always produced in pairs.
- The lightest supersymmetric particle (LSP), is stable.

3.3 MSSM and the softly broken supersymmetry

The MSSM is in actuality a misnomer because it is an extension of the SSM Lagrangian with the "soft terms" added to include symmetry breaking. These are called soft terms because they can be added to the Lagrangian without disrupting the cancellation of the quadratic divergences. This is done by introducing soft mass terms for the scalar members of the chiral multiplets and for the gaugino members of the vector supermultiplets in the Lagrangian. The dimensions of these mass terms must be three or less so we can have either bi-linear mixing terms (B-terms) or the trilinear scalar mixing terms (A-terms). The full set of the soft terms are:

- Scalar mass terms: $m^2\tilde{q}_L^*\tilde{q}_L$, $m^2 H_u^* H_u$.
  These terms give the masses for squarks, sleptons and the Higgs fields.
- Gaugino mass terms: $M\lambda^a\lambda_a$.

These are the mass terms for the gluino, the wino, the zino and the bino.

- Trilinear scalar A-terms: $A_{\alpha\beta\gamma}\phi^{\alpha}\phi^{\beta}\phi^{\gamma}$.

  With the A terms the scalar partners of the left- and right-handed fermions can mix when the Higgs bosons get vacuum expectation values and so they are no longer mass eigenstates

- B terms: BH_uH_d.

  This term only exists for the Higgs terms and mixes the scalar components of the 2 Higgs doublets. The $\mu H_1 H_2$ term is interpreted in the same way although it is a holomorphic mass term because it's value cannot be determined by the SSM [24].

The scalar and the gaugino mass terms have the desired effect of breaking the degeneracy between the SM particles and their SUSY partners. The $\mu H_1 H_2$ term and the soft terms are where all the interest in MSSM lies. But introducing these extra terms has come at a huge expense of a large number of unknown parameters (known as MSSM-124) even with having all the gauge couplings fixed.

The phenomenological MSSM (pMSSM) has reduced the parameters to 19 under the assumptions of no new source of CP violation, no flavour changing neutral currents and the universality of first and second generation. But still the parameter space is too large and difficult to exclude.

3.4 Minimal Super Gravity Supersymmetry Model

The constrained MSSM (cMSSM) also known as Minimal Super gravity model (mSUGRA) is the standardized method for choosing soft terms. It is highly unlikely the nature follows the mSUGRA model even if SUSY exists but it gives benchmark points for experimentalists to use and a bare bone structure for other theories to be compared against.

The soft terms given by mSUGRA are:

- Universal scalar masses $m_\phi^2 = m_0^2$
- Universal gaugino masses $M_a = M_{1/2}$
- Universal A-terms $A_{\alpha\beta\gamma} = AY_{\alpha\beta\gamma}$
- $\tan\beta = \frac{h_u^0}{h_d^0}$ where $\tan\beta$ is the ratio of the up-type vev and the down-type vev. If $\tan\beta$ has a high value it is implied that the physical Higgs is mostly the up-type higgs.
- sign(μ) term, the sign of the higgsino mass parameter [27].

The universality conditions here are taken at the Grand Unification Theory (GUT) scale of $M_{GUT} = 2 \times 10^{16}$ GeV as we presume they come from super string theories. The physical Lagrangian is renormalized to evolve these parameters from GUT scale to TeV scale using radiative breaking of electroweak symmetry the renomalization group equations. This can be done by using the program called SOFTSUSY written by Ben Allanach [27], as shown in the graph below:

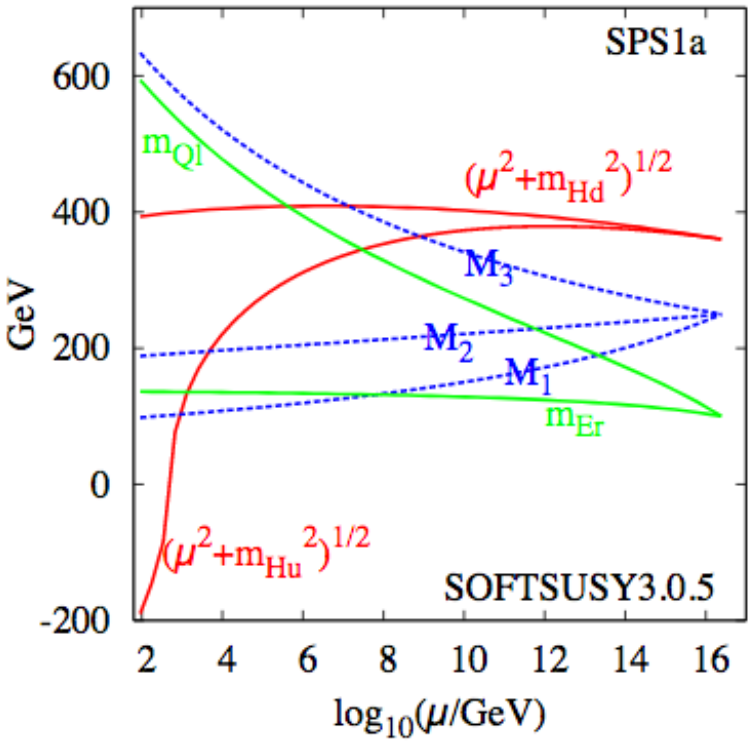

Figure 3.1: The evolution of the soft parameters in the MSSM. Note how the coloured particles (M_3) and Q_L rapidly grow in mass whereas the wino (M_2) and bino (M_1) decreases slightly. Also note that crucially the up-type Higgs mass becomes negative at small energies, inducing radiative electroweak symmetry breaking [27].

The discovery (or exclusion) of weak-scale SUSY is one of the highest physics priorities for the LHC. We target the pair production of gluinos ($\tilde{g}$) and first and second generation squarks ($\tilde{q}$), given their large expected cross section for early SUSY searches in the proton-proton (p-p) collisions at LHC. According to the imposition of R-parity these particles decay to the lightest supersymmetric particle, the neutralino ($\tilde{\chi}_1^0$) which is stable and thus escapes

detection. This undetected $\tilde{\chi}_1^0$ results in missing transverse energy (E_T^{miss}) where as the rest of the cascade, originating from the decays of the $\tilde{q}$ and $\tilde{g}$ results in final states with multiple jets and possibly leptons.

3.5 Motivations for Supersymmetry

There are various phenomenological motivations at weak scale as well as technical motivations at any energy scale for SUSY. Some of these are explained below:

3.5.1 Symmetrical Extension of the Standard Model

SM dynamics are based on symmetries which makes us think that nature likes them. SUSY is the unique combination of the Poincare algebra and the internal symmetries of the S-matrix of the SM under the plausible assumptions of the QFT. Theoretical physicists tried combining these two symmetries into one big group $SU(6)$ but that didn't work, resulting in Coleman and Mandula's theorem stating there was no trivial way to to combine space-time and internal symmetries [29]. Until in 1975, Haag, Lopuskanski and Sohnius using SUSY found a loophole in their theorem and combined fermionic and bosonic symmetry in the super-Poincare algebra [30].

Haag, Lopuskanski and Sohnius' Theorem: *The most general symmetry of the S-matrix is the direct product of super-Poincare and internal symmetries.*

$$G = G_{\text{super}-\text{poincare}} \times G_{\text{internal}} \tag{3.8}$$

The super-Poincare algebra is the extension of the poincare algebra that incorporates SUSY; it turns bosons into fermions and fermions into bosons. In this way, SUSY gives us an extension of the SM symmetries and therein lies it's attractiveness.

3.5.2 Superstrings and Supergravity

The Lagrangian for Einstein's general relativity is given by

$$\mathcal{L}_{GR} = 16\phi^2 M_P^2 \int d^4x\sqrt{g}\mathcal{R} \tag{3.9}$$

General relativity is an effective theory up to the scale Planck Mass M_P equal to $\sqrt{(\frac{Gh}{c^3})} = 2.4 \times 10^{18}$ GeV. At energies below M_P, general relativity works fine, for energies above this it cannot compute anymore because we start getting $((R)^2, (R)^3...)$ terms from loop diagrams and no way to determine their coefficients. This is called the problem of the quantum gravity [30].

One of the ways to solve this problem is by using string theory. String theory uses SUSY to cut off the divergences of quantum gravity and give finite answers. So according to string theory nature always looks supersymmetric at M_P the quantum gravity energy scale. SUSY is also a very important feature of the superstring theory (or, more technically, M-theory) which is the leading "theory of everything", a self-contained mathematical model that describes all fundamental forces and forms of matter [31].

3.5.3 The Hierarchy Problem also known as the "The Weak scale instability problem"

The hierarchy problem is the most important reason SUSY is still here after many defeats in the experimental area. This could be considered the most problematic issue with the SM phenomenology. There is a huge difference between the weak scale and the Planck scale $m_h/M_p \approx 10^{-17}$ so much smaller than 1. In QFT, the Higgs particle receives quantum loops from the heaviest particles i.e the top quark loop, the W loop and the Higgs self coupling, divided by 4π. The question of why the hierarchy is stable with respect to the quantum corrections is called the "technical hierarchy problem" [3]. It is not exactly a problem with SM in it's energy domains but a sensitivity of Higgs particle to any new physics beyond the SM. We know that the electroweak symmetry is broken by a vacuum expectation value for the Higgs at $\nu = 246$ GeV. For the Higgs particle mass calculations, the classical potential is written as

$$V_H = -\mu^2|\phi| + \phi|\phi|^4 \tag{3.10}$$

where the Higgs mass is dependant on the classical values of the μ and ϕ. As in any quantum theory, the parameters in this Lagrangian are going to be affected by quantum corrections. If the SM is cut off by a scale Λ, the quantum corrections are estimated by the term μ^2 which is $\approx \lambda^2$ [30].

If the SM is valid up to the GUT (M_p) scale, quantum corrections to the Higgs potential are then enormous. We would then expect the Higgs mass to be around the GUT scale not at the weak scale that it was discovered to

be at by the LHC.

So either we say that SM is a non-renormalizable theory or that there is some way that these extra quadratic divergences are being cancelled out by new physics that comes in at TeV scale . TeV SUSY gives an explanation for this with it's theorized super-partners canceling out these terms and giving the Higgs boson a definite mass and this also makes it very attractive because at this scale it can be probed at by the LHC.

3.5.4 Gauge-coupling Unification

The strength of the coupling constants for the three basic forces of nature i.e the strong force, the weak force and the electromagnetic force vary with distance between the particles (the top scale shown in the figure above) and energy (the bottom scale). These coupling constants are called the "running coupling constant" because of their varying strength.

If SUSY exists the supersymmetric partners of the color gluons, the gluinos, weaken the asymptotic freedom of the strong interactions and tend to make α_s effective coupling decrease and approach the other coupling constants more slowly. Thus their merger requires a longer lever arm. The weak SU(2) and and hypercharge U(1) couplings are affected by doubling the Higgs field in the supersymmteric models and their is a sixfold enhancement of the asymmetric Higgs field contribution to the running of weak and hypercharge couplings. This causes a small, accurately calculable change in the calculation and these coupling constants will converge at an energy scale of 10^{16} GeV. This accomplishes the theorist's dream of grand unification of the fundamental forces. Without SUSY, in the basic SM there is no single

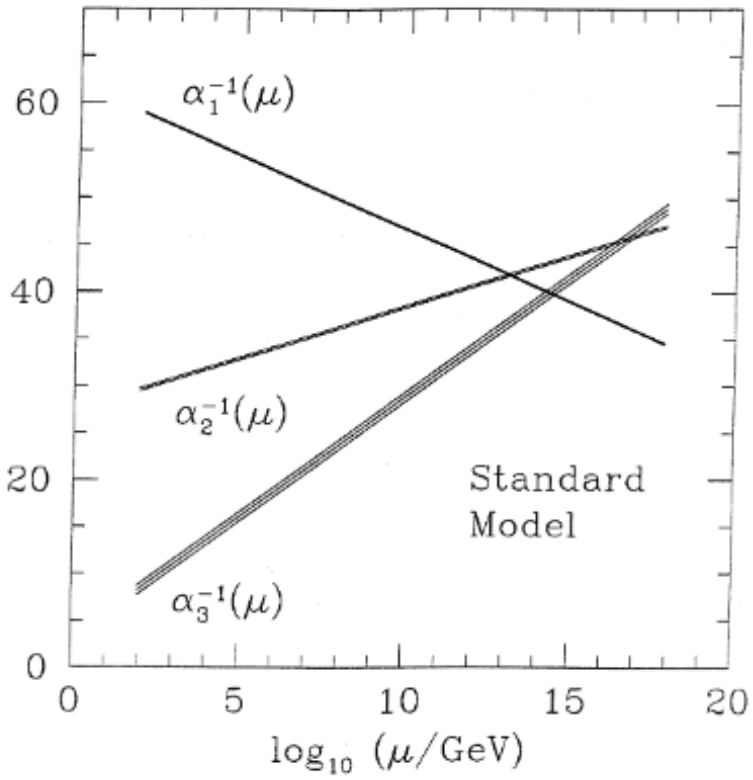

Figure 3.2: Evolution of SM effective (inverse) couplings toward small space-time distances, or large energy-momentum scales [32].

point at which the convergence occurs [32].

3.5.5 Dark Matter Candidate

One more flaw with the SM is that it does not allow any new particle such as WIMPs (Weakly interacting massive particles) which could provide a candidate for the dark matter. In SUSY after electroweak symmetry breaking under the gauge $SU(3) \times U(1)$ symmetry a range of particles (the neutralinos $\tilde{\chi}_1^0, \tilde{\chi}_2^0, \tilde{\chi}_3^0, \tilde{\chi}_4^0$) are produced in the MSSM which is a very attractive solution to this scenario.

The neutralinos are the physical mass states formed by the the two higgsinos, zino and the photino mixing.

$$\begin{pmatrix} \tilde{\chi}_1^0 \\ \tilde{\chi}_2^0 \\ \tilde{\chi}_3^0 \\ \tilde{\chi}_{34}^0 \end{pmatrix} = \begin{pmatrix} a_{11} & a_{12} & a_{13} & a_{14} \\ a_{21} & a_{22} & a_{23} & a_{24} \\ a_{31} & a_{32} & a_{33} & a_{34} \\ a_{41} & a_{42} & a_{43} & a_{44} \end{pmatrix} \begin{pmatrix} \tilde{B} \\ \tilde{Z} \\ \tilde{H}_u \\ \tilde{H}_d \end{pmatrix} \tag{3.11}$$

Moreover, it actually provides a candidate the "neutralino ($\tilde{\chi}_1^0$)" particle at a mass scale consistent with the thermal relic abundance calculations [27].

SUSY is also motivated by solutions to several theoretical problems, for providing many desirable mathematical properties, and for ensuring sensible behavior by the SM at high energies.

3.6 Constraints on SUSY

In this section, I am going to discuss various experimental factors aside from direct searches that have put constraints on SUSY analyses.

3.6.1 Flavour changing neutral currents

Flavour changing neutral currents (FCNC) are very much suppressed and rare in the SM. These can be mediated by new heavy particles which can affect the branching ratio and the angular distributions. These variables can also be used to put constraints on the SUSY models. Figure.3.3 shows a class of Feynman diagrams drawn for CP violating processes called "penguin diagram" for new physics (NP) and SM mediating FCNC.

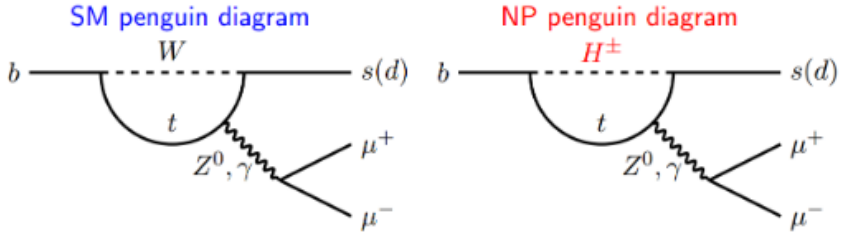

Figure 3.3: Feynman diagrams showing FCNC with SM particles (left) and SUSY Higgs doublet (right) [3].

The LHCb detector has been using a range of angular observables to detect these FCNC in the B hadrons decays. Angular observables are of particular interest because they have less theoretical uncertainties. In 2015, LHCb found a local deviation with respect to the SM prediction, with a significance corresponding to 3.7σ [33] in one observable P_5' as shown in Fig.

3.4. The experimental limits on the SUSY parameter space are also shown here.

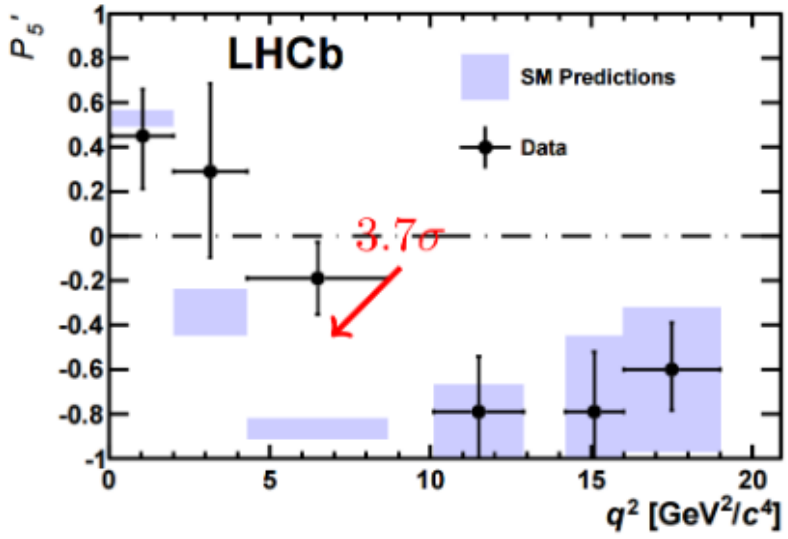

Figure 3.4: Excesses seen at LHCb in the angular distribution observable P_5' [33].

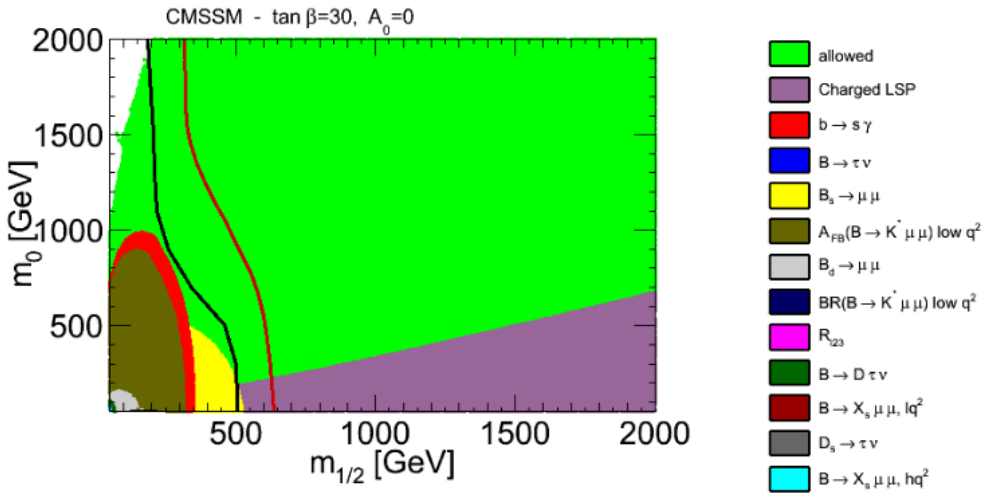

Figure 3.5: Constraints put on SUSY parameter space as result of B anomalies [34].

3.6.2 Magnetic moment of muon

Photon-muon interaction leads to the calculation of the magnetic moment of muon given by the Dirac equation as

$$\overrightarrow{M} = g_\mu \frac{e}{2m_\mu} \overrightarrow{S} \tag{3.12}$$

where at tree level $g_\mu = 2$.

This can be measured very precisely by storing muons in a ring with magnetic fields and measuring the "precession frequency" of their spins. The anomalous factor $a_\mu = \frac{g_\mu - 2}{2}$ comes from loops in the tree diagram as shown in Fig. 3.6:

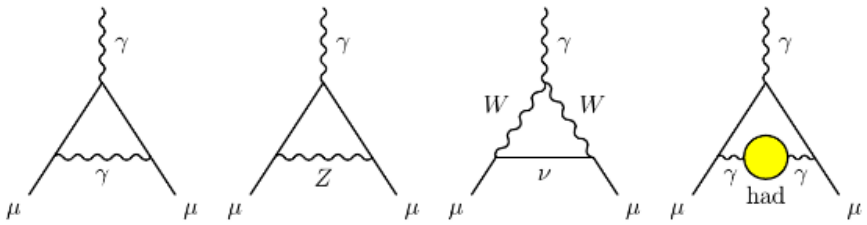

Figure 3.6: Loop diagrams from SM particles explaining a_μ [3].

There is a measurement discrepancy of 3.6σ in the $\Delta a_\mu = a_\mu^{exp} - a_\mu^S M$ and it has been there for 20 years [3]. Figure.3.7 shows the χ^2 fit performed over the mSUGRA parameters discussed in Section 3.4. There are other constraints from $b \to s\gamma$, M_h, electroweak precision parameters $M_W, sin^2\theta_{eff}$ and limits from WMAP and CDF experiments, which are included here.

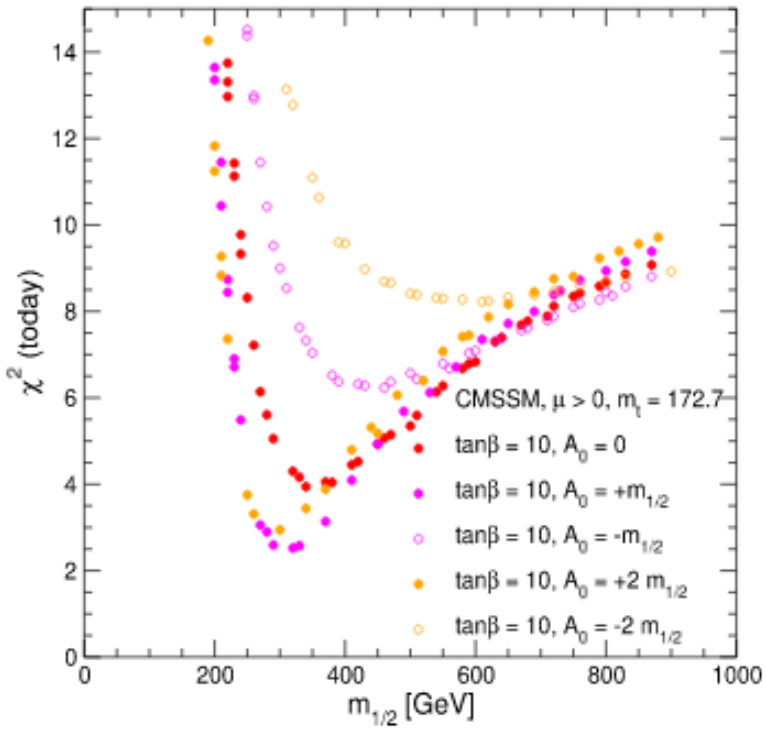

Figure 3.7: Likelihood function χ^2_{tot} for the observable $a_\mu, b \rightarrow s\gamma,\ M_h, M_W, sin^2\theta_{eff}$ in the cMSSM for $\tan\beta = 10$ and various values of A_0. m_0 is chosen to yield the central value of the relic density constraint [35].

3.6.3 Astrophysical Constraints

Then there are the astrophysical constraints on the SUSY parameter space due to the compatibility of SUSY models with the observed Dark Matter relic density. Also, since the neutralino is the R-parity conserving SUSY candidate for weakly interacting massive particles of the dark matter and is a combination of the photino, higgsinos and the wino, this can be used to put limits on many SUSY models. In Fig. 3.8, cMSSM model is illustrated in $m_0 - M_{1/2}$ plane. There is a region mentioned as "bulk region" it corresponds to low values for m_0 and $m_{1/2}$ and no restrain on $\tan\beta$ where $0.1 < \lambda_\chi h_2 < 0.3$. At large value of m_0 and/or $m_{1/2}$ the stau $\tilde{\tau}$ becomes nearly degenerate with the neutralino and they may annihilate into one another. This region is mentioned as "coannihilation region" in the Fig. 3.8. At large values of $\tan\beta$ and $m_{1/2}$ the psuedo scalar mass m_A rapidly drops and a funnel like region is formed with $2m_\chi = m_A$, this is shown by the s-channel annihilation Feynman diagram. Finally there is a region at a very high m_0 where the value of μ starts to fall and the neutralino becomes more higgsino like called the "focus point" [36].

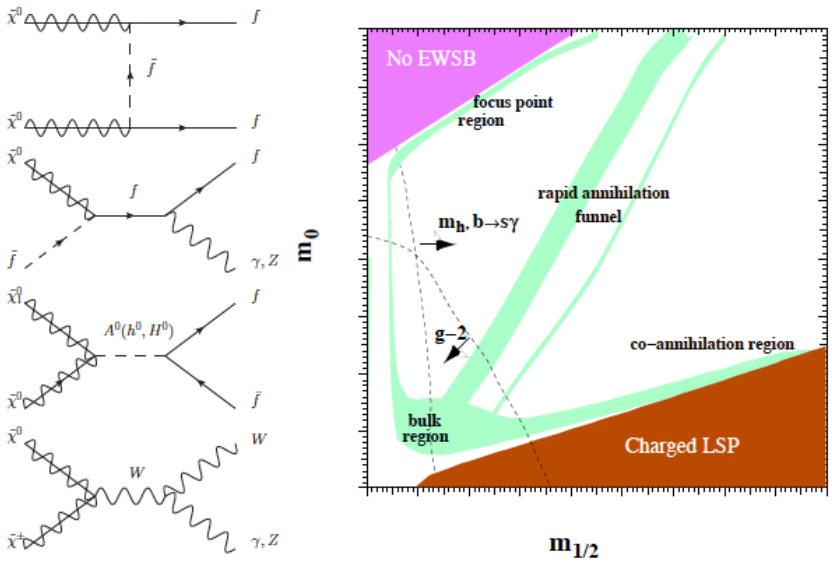

Figure 3.8: (left) Feynman diagrams of possible mechanisms for reduction of the DM relic density. These diagrams (from top to bottom) correspond to the following regions on the CMSSM plane: the bulk region, the co-annihilation region, the funnel region and the focus point [37]. (right) A schematic diagram of the cMSSM with all the constrained and allowed regions [36].

After applying the above mentioned indirect and cosmological constraints as well as the constraints from the direct searches from detectors, the allowed region in the parameter space of cMSSM are [38]:

$$m_0 \geq 100\,\text{GeV},\ m_{1/2},\ \mu \leq 2TeV,\ -3m_0 \geq A_0 \leq 3m_0, 1 \geq \tan\beta \leq 70 \quad (3.13)$$

3.7 Summary

In this part, I have discussed the theoretical basis for my analysis. The successes of the SM and also it's weaknesses were covered. How could SUSY explain away these weaknesses and give models for GUTs and in general help us in understanding nature as a whole, were also touched on. At the end, I have discussed the various factors which put limitations on the SUSY searches. Further on, I will explain my analysis technique which will work inside these constraints to look for supersymmetric particles at the ATLAS detector.

Part II

Technology and Tools

Chapter 4

The Large Hadron Collider and the ATLAS detector

The knowledge of physics laws at the sub-nuclear level (10^{-13} cm or smaller) is in the most part a result of collider experiments where we analyze the outcomes of high-energy collisions of elementary particles. The LHC is the largest and the highest energy particle collider ever built. It started working in September 2008. It was built by the European Organization for Nuclear Research (CERN) to probe the energy frontiers and to answer the various unresolved questions of particle physics, including the existence of the then hypothesized Higgs boson and of the large family of new particles predicted by SUSY.

Inside the LHC, two beams of protons are accelerated and collided with each other at extremely high energies at TeV scale. This produces an avalanche of particles that can be seen in the simulation of an event by the Sherpa generator in Fig. 4.1

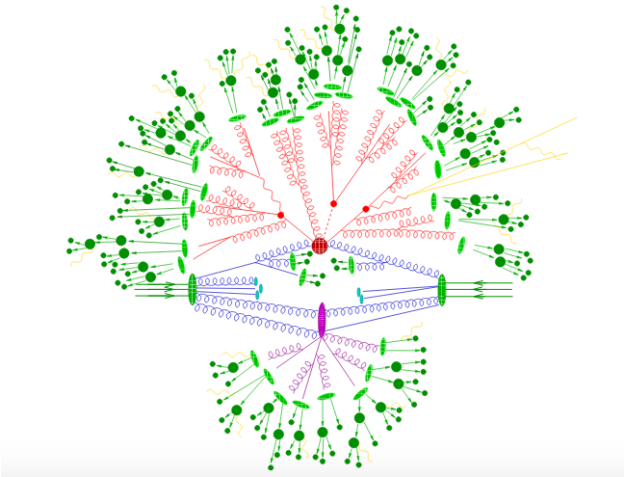

Figure 4.1: Pictorial representation of a *tth* event as produced by an event generator. The hard interaction (big red blob) is followed by the decay of both top quarks and the Higgs boson (small red blobs). Additional hard QCD radiation is produced (red) and a secondary interaction takes place (purple blob) before the final-state partons hadronize (light green blobs) and hadrons decay (dark green blobs). Photon radiation occurs at any stage (yellow) [39].

These proton beams; one moving clockwise and the other anti-clockwise; are smashed together in a 27 km radius tunnel underground the Swiss-Franco border near Geneva, Switzerland. They are guided along the circumference by super-conducting magnets. This allows us to study the physics at extremely small size scales and high energies.

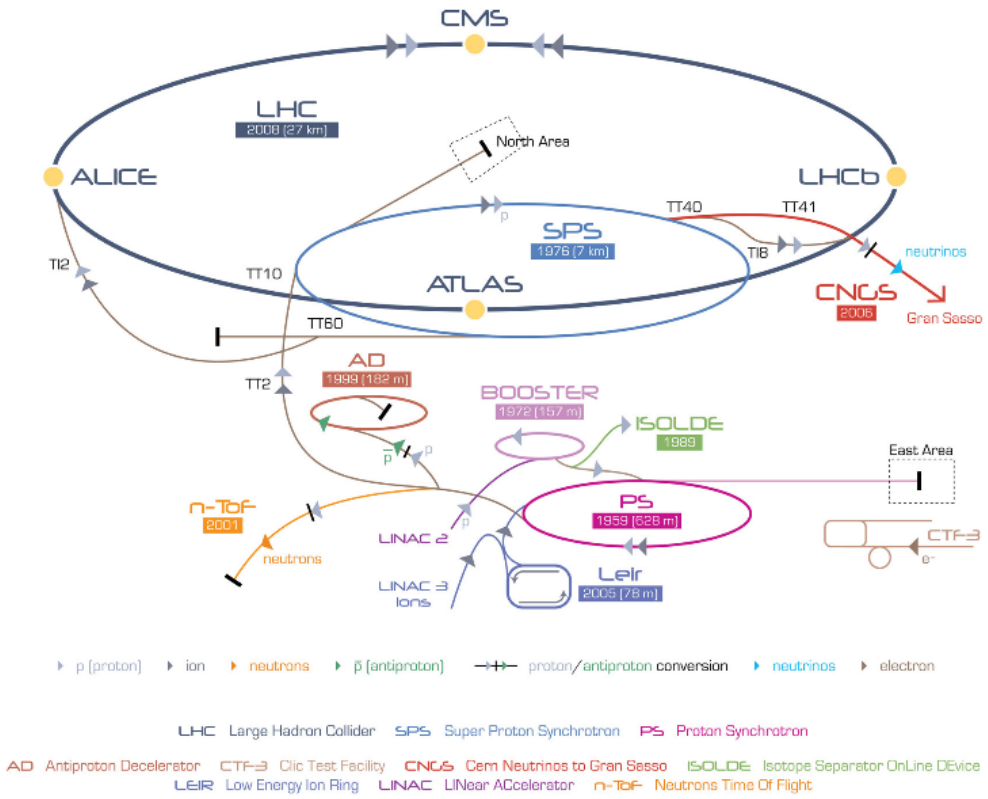

Figure 4.2: The Large Hadron Collider ring [40].

The LHC performs p-p collision at four points along it's ring. To analyze the particles produced by the collisions, the LHC has four main detectors

at these four points, that are CMS, ATLAS, LHCb and ALICE as shown in Fig. 4.2. The LHC is designed to produce beam collisions at centre-of-mass energy of $\sqrt{s} = 14$ TeV. In 2010-2011, a collision energy of 7 TeV was achieved, ramping up to 8 TeV in 2012. In 2015, the LHC restarted operations, colliding protons at 13 TeV. After the third technical stop in 2021, LHC will operate at the intended $\sqrt{s} = 14$ TeV centre-of-mass energy.

Protons are injected into the LHC after they go through a series of particle accelerators and linear colliders. First, these protons are produced in a linear collider called **Linac 2**. They are ejected from the hydrogen atoms and accelerated to 50 MeV. These protons are then transferred to the next particle accelerator called the **PS Booster** which accelerates them to 1.4 GeV. The next accelerator after that is the **Proton Synchrotron** which accelerates them to 25 GeV. After that to the **Super proton Synchrotron (SPS)** where they are further accelerated to 450 GeV. After that they are finally injected into the LHC which accelerates them to the TeV ranges.

The protons move through the ring in bunches. Every bunch has $\sim 10^{11}$ protons and there is the capacity for 2808 bunches in every beam. These bunches of protons are 16 μm in width and few centimeters in length to ensure the maximum number of collisions. Bunches of protons cross 40 million times a second. But the collisions don't happen for all the protons, every bunch crossing provides us with almost 25 interactions. When any protons collide the process is called an "event".

An important parameter to consider for any accelerator complex is called

the "Luminosity" defined as:

$$L = \frac{N_b^2 n_b^2 f_{rev} \gamma_r}{4\pi \epsilon n \beta^*} F \tag{4.1}$$

where N_b is the number of protons per bunch, n_b is the number of bunches, f_{rev} is the revolution frequency, γ_r is the relativistic gamma factor, ϵn is the normalized transverse beam emmittance, β^* is the beta function of the beam at the collision point and F is the geometric luminosity reduction factor since the beams cross under a certain angle at the interaction points [41]. We calculate the performance of the accelerator using "integrated luminosity" and "instantaneous luminosity". The instantaneous luminosity is directly proportional to the rate of collisions whereas the integrated luminosity is proportional to the total number of collisions collected. Luminosity in a detector can be increased by making improvements to the criteria in Eq.4.1. Fig. 4.3 and Fig. 4.4 show the integrated luminosity recorded the year 2015 and 2016 respectively.

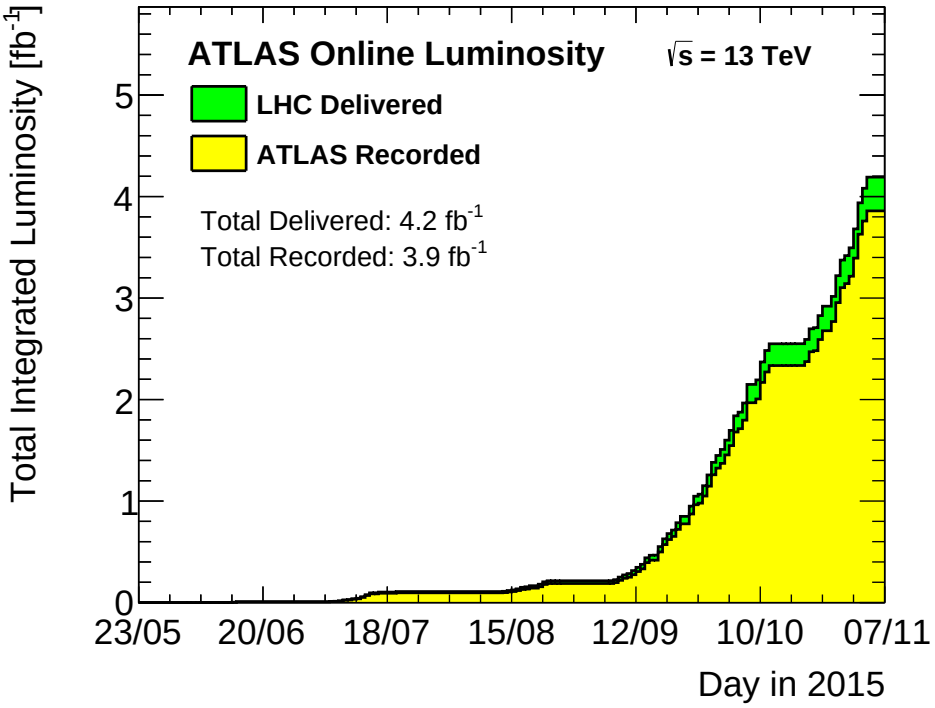

Figure 4.3: Cumulative luminosity versus time delivered to ATLAS (green) and recorded by ATLAS (yellow) during stable beams for p-p collisions at 13 TeV centre-of-mass energy in LHC Run 2 for the year 2015 [42].

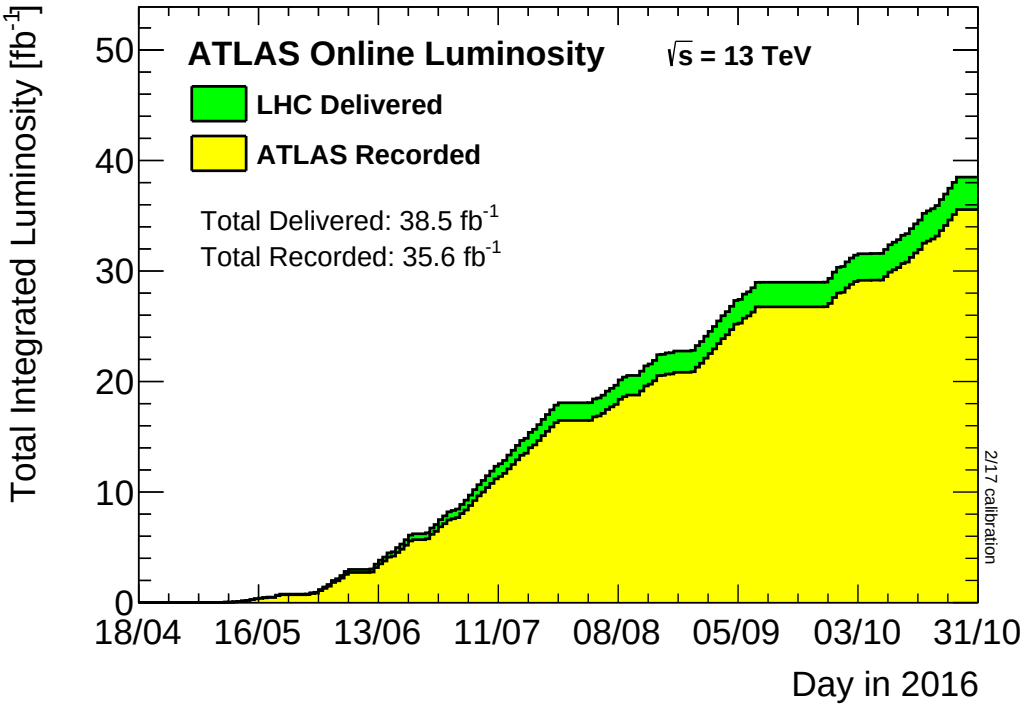

Figure 4.4: Cumulative luminosity versus time delivered to ATLAS (green) and recorded by ATLAS (yellow) during stable beams for p-p collisions at 13 TeV centre-of-mass energy in LHC Run 2 for the year 2016 [42].

4.1 The ATLAS detector

ATLAS (A Toroidal LHC ApparatuS) is a multipurpose detector, i.e., looking for new particles, trying to learn about the basic forces of nature and exploring about the unknown like the extra dimensions and dark matter candidates. It's main purpose is to look for the Higgs boson, but now that it has been discovered, further investigations will tell us about it's properties

and thereby about the question of the "origin of mass".

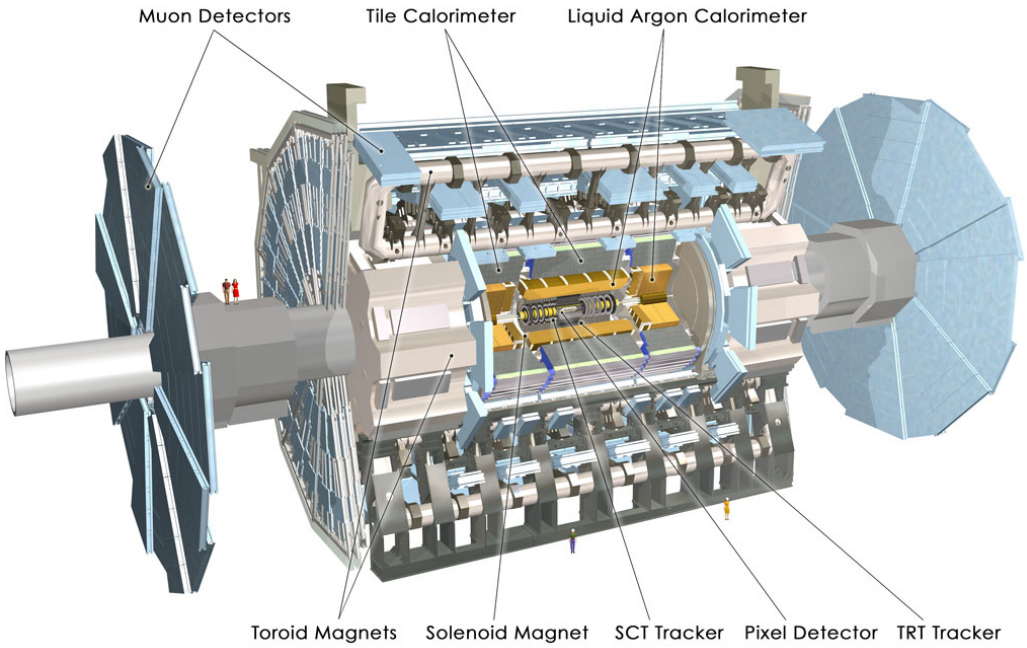

Figure 4.5: The ATLAS detector [43].

The ATLAS detector is 25 m in height and 46 m in width. It's overall weight is 7000 tones with approximately 100 million electronic channels and $\sim$ 3000 km of cables. It consists of four parts which are arranged in concentric forward-backward symmetric cylindrical layers, around the interaction point as can be seen in Fig. 4.5, these are:

- The Muon system, which is the outer blue region in Fig. 4.5, for detecting and measuring the momenta of highly penetrating muons. The muon spectrometer (MS) has separate trigger and very high precision tracking chambers with a total trigger coverage of $|\eta| < 2.4$ and muon identification and momentum measurement for $|\eta| < 2.7$.

- The Calorimeters, that are used for measuring the energies of the particles produced by the p-p collision. Jets are reconstructed using the energy deposits in the hadronic calorimeters. A scintillator/tile calorimeter is used for hadronic coverage for $|\eta| < 1.7$. The electromagnetic calorimeters consist of the high granularity liquid argon (LAr) sampling calorimeters using lead as an absorber. This calorimeter has acceptance covering $|\eta| < 3.2$.

- The Magnet system, that is composed of two large superconducting magnet systems, i.e., the outer toroidal magnetic field outside the calorimeters and within the muon system and the inner solenoid which surrounds the Inner Detector. These magnetic fields are fundamental for the momentum measurement.

- The Inner Detector, the main function of this part of the ATLAS detector is to measure the momentum of the outgoing charged particle and the primary and secondary vertex determination in a particle dense environment. Electron identification is also primarily done here. It consists of three parts: the Pixel Detector which is a high granularity silicon pixel detector, the Semiconductor Tracker which consists of silicon microchips and outside both of these is the Transition Radiation tracker which is made of drift tubes with transition radiation material (Ref. [43]). This part of the detector provides precise tracking of particles for $|\eta| <2.5$.

- The End-caps and forward regions, which go from $1.5 < |\eta| <4.9$, are instrumented with LAr calorimeters which are used for both electro-

magnetic and hadronic measurements.

The information coming from these different sub-detectors is then recorded using the coordinate system with a origin at the Primary vertex, the z-axis points along the beam pipe , the y-axis points upwards and the x-axis points towards the centre of the LHC ring and is perpendicular to $\overrightarrow{y}$ and $\overrightarrow{z}$. The azimuthal angle ϕ is used for describing angles around the beam axis i.e. in the xy-plane and the polar angle θ describes the angles from the beam axis i.e. in the yz-plane. More commonly used operator is η a function of θ:

$$\eta = -ln(\tan\frac{\theta}{2}) \tag{4.2}$$

where η is 0 perpendicular to $\overrightarrow{z}$ at the primary vertex (PV) and ∞ along the beam axis. Distances in η are Lorentz invariant under longitudinal boost in $\overrightarrow{z}$ direction. Angular distances from the PV are calculated in the $\eta\phi$-plane using the equation [44]:

$$\Delta R = \sqrt{(\Delta\phi)^2 + \Delta\eta)^2} \tag{4.3}$$

In 2012, a data set with integrated luminosity of 20.3 fb^{-1} at a centre-of-mass energy of 8TeV was recorded by the ATLAS experiment. Before the Run-II of LHC in 2015, ATLAS went through several upgrades which include the installation of the Insertable B-Layer in the pixel detector, a smaller beampipe, additional muon end-cap chambers, and some new trigger hardware. Also, significant improvements to the algorithms for physics object reconstruction are done, which were applied to 13 TeV data for the first time. During Run-II 2015+2016 ATLAS recorded $L = 36.1$ fb^{-1} of data at a centre-of-mass energy of 13 TeV. This is the data set used for this analysis

as described in chapter 9.

ATLAS has a rich physics program where a large number of physics analysis are being done. These analyses include precise measurements of known SM processes like top-physics, electroweak-physics and the search for the Higgs boson. Also, experimental searches are on-going to look for physics beyond the SM, e.g. new physics like SUSY and other extensions of the SM.

Chapter 5

Physics Object Definition in ATLAS

Reconstruction of particles is a process that converts the electrical signals recorded by the different detector elements into collections of measurements associated to different particles produced by the p-p collision. There are several layers of the reconstruction procedure of data. The first level of reconstruction objects are called the "tracks" and the "clusters". Tracks are the trajectories of the charged particles through the detector. The Inner Detector (ID) and the Muon Spectrometer (MS) in ATLAS are used to produce track collections. These charged particles leave behind signals called "hits". Track reconstruction provides us with the primary vertex, the direction and the momentum of a charged particle.

When electromagnetic and hadronic particles pass through the calorimeters they interact with the specific materials used in the construction of these calorimeters and produce a cluster of secondary electromagnetic or hadronic

particles which in turn produce tertiary particles. Electromagnetic particles e.g electrons and photons produce dense and narrow showers and are produced in the electromagnetic calorimeter. Whereas the wide spread hadronic showers are measured in the hadronic calorimeter. Cluster reconstruction is done in both of these calorimeter and these data are then submitted to higher level reconstruction algorithms for particle identification.

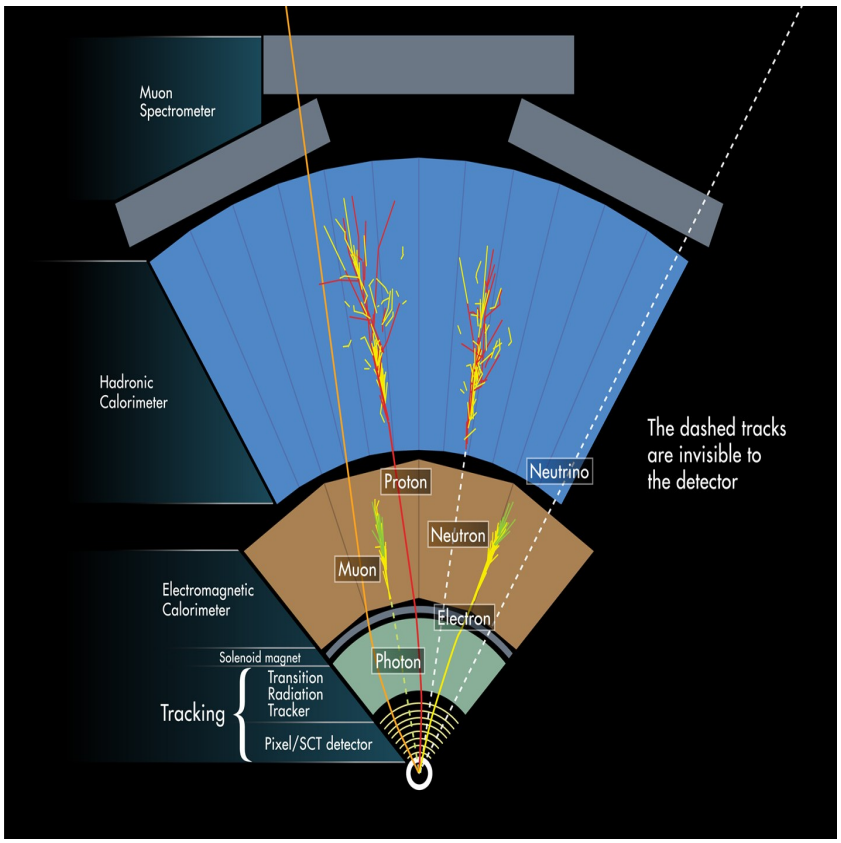

Figure 5.1: A transverse cut of the ATLAS detector to show different particle's signature in different detector components [45].

Figure 5.1 shows a transverse cut of the ATLAS detector differentiating between it's different components. It can be seen that different types of particles produced at the interaction point, leave different types of responses when transversing through various parts of the ATLAS detector. The reconstruction of these particles is described below:

5.1 Muons

Charged leptons like electrons and muons leave clear signals in the ATLAS detector and they are very efficiently measured. Highly energetic muons travel through the whole ATLAS detector to the MS and are measured there. They are reconstructed by matching tracks in the ID and the MS. Muons produced from the W and Z bosons decay have large momenta $\sim$ 15 GeV and are called isolated muons because they have no surrounding activity. Muons are also produced from hadronic decays of mesons including heavy flavor decays. These have different criteria for selection and reconstruction. All muon candidates have to have at least one hit in the Pixel detector and at least six hits in the SCT and the TRT. In MS, the muon candidates are then fit together using the hits from segments in different layers using a global χ^2 fit. Muons are labeled differently depending on the reconstruction algorithms used which in turn depend on the combined ID-MS information provided [46].

The SUSY working group definitions of muons which are used in the analysis here are of signal and baseline leptons. Baseline muons are used with

a transverse momentum $p_T > 7$ GeV, $\eta > 2.7$, $d_0 > 3$ and $z_0 < 0.5$. Default muon identification is performed by applying quality requirements that suppress background, mainly from pion and kaon decays, while selecting prompt muons with high efficiency and robust measuerments. Also for this analysis, selections are applied on cosmic muons to remove cosmic radiation background.

5.2 Electrons

Electrons traveling through the detector, produce a track in the ID and a shower in the electromagnetic calorimeter as can be seen in the Fig. 5.1. They are very efficiently reconstructed by the ATLAS detector where the signal and the background is separated very cleanly. Electrons produced from the decay of W and Z bosons for our control regions are often selected using an isolation criteria. Isolation reduces the number of electrons selected that arise from heavy hadron decays and fake electrons from hadrons that mimic electron signatures. The isolation requirement is that for the total transverse momenta of tracks with in a cone of $\Delta R = 0.2$ around the electron candidate is to be less than 10% of the transverse momenta of the electron.

Prompt electrons from the central detector region $\eta < 2.47$ are selected using a likelihood based identification (LH) [47]. There are four operating points used by the analysis in ATLAS that cover the various required prompt-electron signal efficiencies and corresponding background rejection factors. These are $VeryLoose$, $Loose$, $Medium$ and $Tight$ corresponding to electron efficiencies of $> 93\%$, 93%, 88% and 80% respectively. We use the "TightLH"

operating point for electron identification in our analysis.

5.3 Taus

Tau leptons are also charged leptons but they have a short life time (0.3 ps) and decay into other charged particles (electrons and muons plus neutrinos, or hadrons and a neutrino) and are not directly observed. The leptonic taus have a very definite signal but the hadronic taus don't have a very good reconstruction because it suffers from a large amount of background. Neutrinos on the other hand are not detected at all because they have very small weak interactions. They are inferred using the overall transverse momentum imbalance called the "missing transverse energy" E_T^{miss}. Tau leptons (τ) are the heaviest of the charged leptons, and the only leptons that can decay into hadrons (with a branching fraction of about 65%). The hadronic decays consist of an odd number of charged particles, and zero or more neutral particles, and a tau-type neutrino (ν_τ) as shown in the Table.5.1. Tau identification is important in searches for the SM Higgs boson decaying into $\tau^+\tau^-$ as well as the supersymmetric searches for heavier Higgs decays.

Table 5.1: Tau decay channels and their branching ratios. Charged hadrons are denoted by the symbol $h^{\pm}$ and although for simplicity τ^- is shown, the processes are valid for the charge conjugate [48].

Decay Mode	Resonance	$\mathscr{B}(\%)$
Leptonic Decays		35.2
$\tau^- \to e^- \bar{\nu}_e \nu_\tau$		17.8
$\tau^- \to \mu^- \bar{\nu}_\mu \nu_\tau$		17.4
Hadronic Decays		64.8
$\tau^- \to h^- \nu_\tau$		11.5
$\tau^- \to h^- \pi^0 \nu_\tau$	$\rho(770)$	25.9
$\tau^- \to h^- \pi^0 \pi^0 \nu_\tau$	$a_1(1260)$	9.5
$\tau^- \to h^- h^+ h^- \nu_\tau$	$a_1(1260)$	9.8
$\tau^- \to h^- h^+ h^- \pi^0 \nu_\tau$		4.8
Other		3.3

Electrons and muons from tau decays can not be distinguished from primary electrons and muons. Tau jets are reconstructed by the anti k_t algorithm with a distance parameter R = 0.4, $p_t > 10$ GeV and $|\eta| < 2.5$ [49]. Tau decay vertex is identified as ID track vertex with the largest momentum fraction from tracks within the jet core $\Delta R < 0.2$. Tau jets also show a distinctive one-prong and three prong structure and tau identification is optimized separately for both of them. Boosted Decay Tree (BDT) theorems are utilized by the τ working group to reject quark and gluon initialized jets. Three tau identification categories are used: *loose*, *medium*, *tight* with efficiencies of 0.6 (0.5), 0.55 (0.4) and 0.45 (0.3) respectively, for 1-

prong (3-prong) decays [49]. For our analysis we use "medium taus" which is the default/recommended identification criteria for taus with $p_T > 20$ GeV, $|\eta| < 2.8$ and 1 or 3 number of tracks.

5.4 Photons

Photons are electrically neutral so they don't produce charged tracks in the ID but they do produce showers in the EM calorimeter. Photons can convert into electron positron pair which do leave tracks in the ID and a vertex that is displaced from the interaction point. Photon reconstruction is seeded by clusters with transverse energy greater than 2.5 GeV in the EM calorimeter. These clusters are than matched with tracks from the ID clusters without matching tracks are classified as unconverted photon candidates [50]. Clusters with matched tracks in the ID are considered as electrons candidates. If the photons are tracked back to a reconstructed vertex they are considered as "converted" photon candidates. To increase the photon reconstruction efficiency if we have one of the two tracks reconstructed and no hits in the innermost pixel layer we consider it as a photon candidate. Photon identification is based on two sets of identification criteria "loose" or "tight" each dependent on the independent requirements on shape variables defined in [50]. We have used the "tight" criteria here for our analysis with isolated photon $p_t > 25$ GeV, $|\eta| < 2.37$ and $|\eta|_{\text{clusters}} < 2.37$ and are used in the control region of the analysis CRγ.

5.5 Jets

Jets are reconstructed from particles that decay and produce showers in the hadronic calorimeter as shown in the Fig. 5.1. High momentum jets correspond to a final state quark or gluon. The reconstructed jet energy can be used to estimate the energy of the initiating parton in the p-p collisions. Jets are reconstructed using the anti-k_t algorithm from the $FASTJET$ package. The most commonly used radius parameter choice for the anti-k_T algorithm is $R = 0.4$ but $R = 0.6$ is also used when looking at the decay products of highly boosted massive objects called "large R jets".Three types of jets are reconstructed depending on the input, truth jets: from the event generator record of simulated events, *track jets*: from inner detector tracks or *calorimeter tracks*: reconstructed from the calorimeter clusters. Truth-particle jets must originate from hard-scatter vertex, and do not include muons and neutrinos nor particles from pile-up in order to ensure that they are produced from particles that leave significant energy deposits in the calorimeters.

Calorimeter jets or "topo-cluster" jets are built from clusters of adjacent calorimeter readout cells that contain a significant transverse energy above the noise. After that these jets are calibrated to an appropriate jet energy scale by two calibration schemes. In the "electromagnetic-scale" jet energy scale calibration scheme clusters are first calibrated to the electromagnetic scale, this is the basic signal scale accounting correctly for the energy deposited in the calorimeter by the electromagnectic showers. Then a η and p_T dependent scaling factor is applied to correct the jet energies to the level of hadronic showers. This scaling factor is derived from the `Geant4` simulations

and test-beam responses.

Topo-clusters may be calibrated further using the local cell signal weighting (LCW) method to estimate the jet energy scale calibration of the clusters prior to jet formation. This method is basically designed to improve the energy resolution of the reconstructed jets from EM scale by including the out-of-cluster energy deposits, the dead parts of the calorimeters, the pile-up corrections and the energy fluctuations in the calorimeter.

Global sequential calibration is also applied on these jets which corrects for the "jet flavour" meaning the jets originating from quarks differ in shape and calorimeter energy response to jets originating from gluons [51].

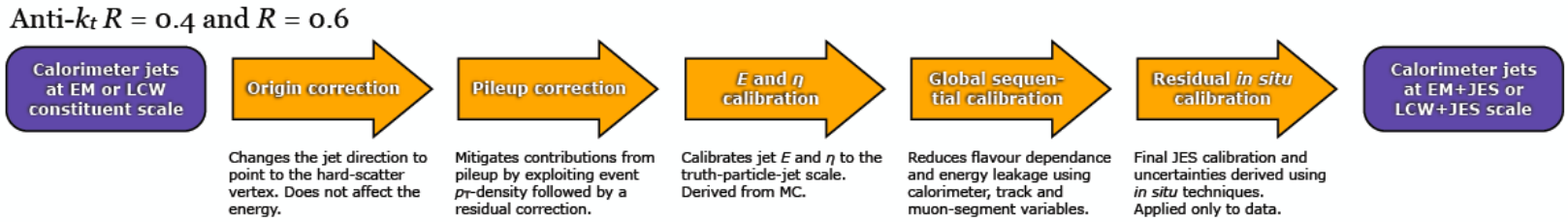

Figure 5.2: Overview of the ATLAS jet calibration described in this thesis. All steps are derived and applied separately for jets built from EM-scale and LCW calibrated calorimeter clusters, except for the global sequential calibration, which is only partially applied to LCW-jets [51].

For our analysis we have used anti-k_T EM topo cluster jets with R = 0.4, $p_T > 50$ GeV except for the leading one which has $p_T > 200$ GeV and with $|\eta| < 2.8$. If a jet four-momentum lies within a $R < 0.2$ cone relative to an electron or photon, the jet is discarded, and the electron or photon is retained to avoid double counting of physical objects as the photon/electron reconstruction is done at the same time as the jets [52]. Similarly if a lepton/photon is included in the $R < 0.4$ cone of the jets, the lepton/photon is discarded because they are likely to originate from a heavy flavour quark decay. Also, some cleaning cuts are applied to all the jets in an event called the "event cleaning". For this a track based variable is defined called the "jet charge fraction" (f_{ch}). This is calculated as the ratio of the scalar sum of the p_T of the tracks coming from the jet's primary vertex to the jet p_T. Another variable is defined for the "jet energy fraction in the layer with maximum energy deposit (f_{max})". The ratio of these two variables (f_{ch}/f_{max}) is a good discriminant between good and fake jets because the fake jets have low values for the f_{ch} variable [53].

5.6 b-jets

It is very hard to identify the type of parton that initiated the jet except for b-quarks. b quark jets or "b-jets" a sub-population of the above mentioned anti-k_T EM topo cluster, are identifiable because of their secondary vertex and several tracks coming from the long-lived B-hadron. This is called "b-tagging". The b-tagging algorithms use transverse Impact parameter d_0 and longitudinal Impact parameter z_0 to identify the secondary vertex as shown

in the Figure 5.3.

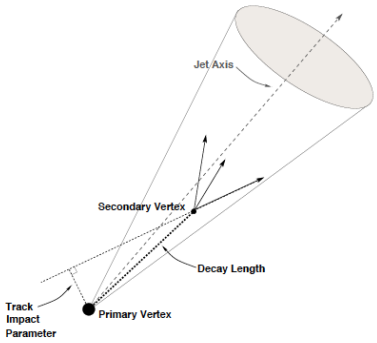

Figure 5.3: Schematic diagram of b-decay within a jet [54].

The b-tagging algorithm used for this analysis is $MV2c10$ a multi-variate method trained to discriminate b-jets against light flavour jets with a b-jet efficiency measurement of 77% [55]. The charm jets are also classified by this method but to a much lesser degree of success.

5.7 Missing transverse energy

Different algorithms have been developed at ATLAS for the reconstruction of the E_T^{miss} depending on where the energy is coming from whether the tracks from the ID, the energy deposits from the calorimeters or a combination of both. The E_T^{miss} reconstruction estimates the missing transverse momenta in the detector from the calibrated signals coming from muons(μ), electrons(e), photons (γ), hadronically decaying tau decays (τ) and the anti-k_T EM topo jets. The E_T^{miss} vector is calculated along the x and y axis as follows:

$$E_{x(y)}^{\text{miss}} = E_{x(y)}^{\text{miss},\mu} + E_{x(y)}^{\text{miss,e}} + E_{x(y)}^{\text{miss},\gamma} + E_{x(y)}^{\text{miss},\tau} + E_{x(y)}^{\text{miss,jets}} + E_{x(y)}^{\text{miss,soft}} \quad (5.1)$$

where each term is the negative vectorial sum of transverse momenta of tracks of charged particles or their energy deposits [56]. The value for E_T^{miss} and it's direction ϕ^{miss} are then calculated as

$$\begin{aligned} E_T^{\text{miss}} &= \sqrt{(E_x^{\text{miss}})^2 + (E_y^{\text{miss}})^2} \\ \phi^{\text{miss}} &= \tan^{-1}((E_x^{\text{miss}}), (E_y^{\text{miss}})) \end{aligned} \tag{5.2}$$

The E_x^{miss} and the E_y^{miss} terms are expected to be Gaussian distributions for $Z \to ll$ events [57]. But their tails are definitely non-Gaussian and we do not want to loose information so we use root-mean-square (RMS) to estimate the resolution [56]. The object definitions for E_T^{miss} terms are the ones mentioned above. The order of terms here is important to minimize double counting of the physical objects. These terms are called the *hard* terms of the E_T^{miss}. The $E_{x(y)}^{\text{miss,soft}}$ term includes all contributions from the tracks or energy deposits that are not classified into the hard terms. The default SUSY working group operating point for E_T^{miss} is the "loose" working point with $\text{jet}_{p_T} > 20$ GeV and $\text{jet}_\eta < 2.4$. The uncertainty in the E_T^{miss} comes from the sum of all the uncertainties included in the calculation of E_T^{miss} and varies for all analysis. For our analysis we use only the systematics from the tracks and not from the calorimeters.

There are also those types of particles that are produced in the collisions but do not directly interact with the detector because of their short lifetime. They are reconstructed using signature decay modes. Z bosons can be detected using the two reconstructed electrons/muons or the W boson is detected reconstructing the electron/muon, neutrino decay. We calculate their masses and momenta without directly observing them. The same tech-

niques are used for Higgs boson detection using $H \to ZZ^{(*)} \to llll$ and $H \to WW^{(*)} \to l\nu l\nu$ decays (where $l = e, \mu$) [45].

5.8 Systematic Uncertainties

Lepton reconstruction inefficiencies can arise from the mis-modelling of the leptons as well as selection inaccuracies. These are corrected to match the data by using scale factors. These scale factors are calculated from the data efficiencies in the $Z \to \mu\mu$ or $Z \to ee$ and $W \to e\nu$ channels as a function of the lepton kinematics [37]. Jet energy scale (JES) uncertainties are corrections in the jet energy scale for calorimeter non-compensation and energy loss in dead material. This scale factor is calculated as the ratio of the reconstructed jet transverse momentum to the truth simulated jet transverse momentum $p_T^{\text{reco}}/p_T^{\text{truth}}$. Truth (generator-level) jets are obtained by applying the anti-k_t algorithm to the stable particles in simulated events that have a lifetime of $c\tau < 10$ mm. The effect of this uncertainty is assessed by varying p_T, η, pile-up and nearby dependent calibration by $\pm\sigma$. The width of the jet response distribution or the jet's energy resolution (JER) is also a important systematic uncertainty. This is calculated by by taking the ratio of the width σ_{p_T} to the mean value, p_T, of a Gaussian fit to the jet energy response distribution.

Combining all the uncertainty sources, the total uncertainty amounts to around 1% at medium p_T in central detector region but can be larger where statistics are sparse. The b-jet scale factors and their uncertainties are also calculated in the same way as the JES with up and down variations around σ.

The uncertainties in E_T^{miss} come from summing up the uncertainties in all the terms included in the E_T^{miss} final term calculation. However the uncertainty on the soft term is specified by how well it is modeled in simulation. In an event where the true E_T^{miss} is zero, the p_T^{hard} should be totally be balanced with p_T^{soft} but detector resolution effects give a Δp_T^{miss} here as shown in Fig. 5.4. This systematic uncertainty is calculated from the maximal disagreement between the 2015+2016 data plus parton shower models for a certain set of p_T^{hard} bins [56].

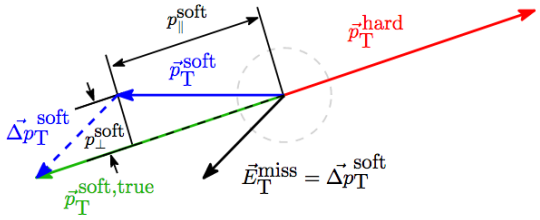

Figure 5.4: Sketch of the track-based soft term projections with respect to p_T^{hard} for the calculation of the track based soft term systematic uncertainties [56].

Integrated luminosities of a dataset also have an assigned uncertainty from the counting rates measured by the ATLAS luminosity detectors. The uncertainty on the measured luminosity is 2.1% for the 2015 and 3.4% for the 2016 data set.

Chapter 6

Trigger Techniques used at ATLAS

6.1 Pile-Up

During the 2015+2016 data taking ATLAS recorded number of events to the order of 10^{15}. Number of protons in a bunch crossing are 10^{11} squeezed down to 64 microns at the interaction point. This is to ensure multiple interactions per bunch crossing, which results in overlapping data from different p-p collisions. This is called "Event Pile-Up" or just "Pile-up" and this phenomena produces particularly challenging complications for reconstruction and identification softwares as can be seen in display event for the first beam collisions of 2015 recorded by the ATLAS detector.

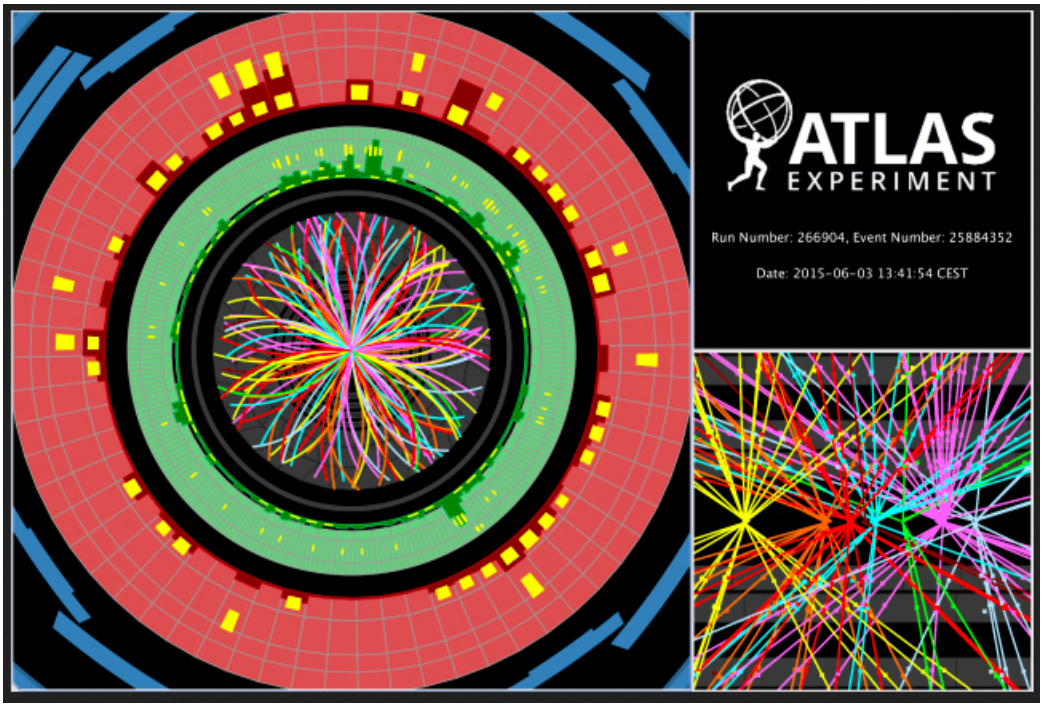

Figure 6.1: Display of a p-p collision event recorded by ATLAS on 3 June 2015, with the first LHC stable beams at a collision energy of 13 TeV. Tracks reconstructed from hits in the inner tracking detector are shown as arcs curving in the solenoid's magnetic field. The yellow rectangles along with the red and green bars indicate energy deposits in the liquid argon and scintillating-tile calorimeters. Tracks originate from several vertices, indicating multiple p-p interactions (also known as pile-up) recorded in one event [58].

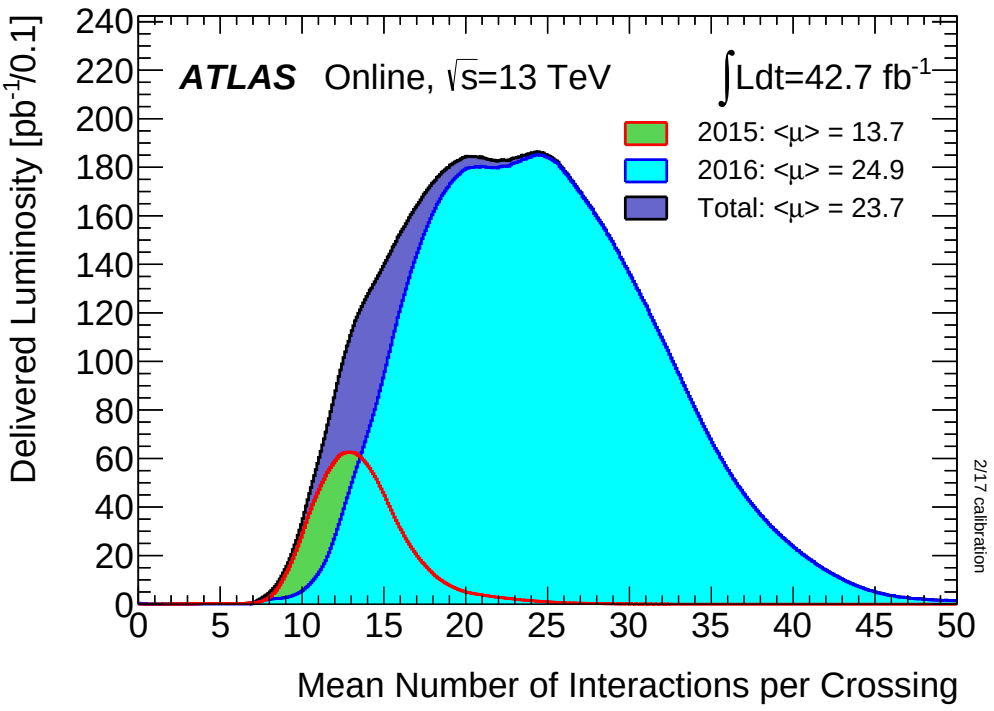

Figure 6.2: For 2015+2016, all data delivered to ATLAS during stable beams is shown, and the integrated luminosity and the mean μ value are given in the figure. The mean number of interactions per crossing corresponds to the mean of the poisson distribution of the number of interactions per crossing calculated for each bunch. It is calculated from the instantaneous per bunch luminosity as $\mu = L_{\text{bunch}} \times \sigma_{\text{inelastic}}/f_r$ where L_{bunch} is the per bunch instantaneous luminosity, $\sigma_{\text{inelastic}}$ is the nelastic cross section which we take to be 80 mb for 13 TeV collisions and f_r is the LHC revolution frequency [42].

There are two types of pile-up; in-time and out-of-time pile-up. In-time pile-up happens when multiple p-p collisions take place in the same bunch crossing as the same time. We end up with large number of tracks, clusters, excessive energy in the calorimeters and the reconstruction of the primary event of interest is muddled. In-time pile-up has a significant effect on identification of electrons, jets and the measurement of missing E_T.

Out-of-time pile-up happens when data from the previous bunch crossing overlaps with the current bunch crossing. Out-of-time pile up primarily disrupts the EM calorimeter energy measurements when energy deposits from the previous bunch crossing add up in the current bunch crossing's energy. They give a long tail to signal shaping time and decrease the energy resolution.

6.2 TDAQ scheme in ATLAS

Since the higher the mass of the particle we want to produce the smaller it's cross section is. To counteract that we produce large numbers of events to achieve significant quantities of these rare occurrences. At the LHC we produce almost 1 billion p-p collisions per second. If all of the data produced were to be recorded it would fill 100,000 CDs per second [59].

ATLAS online software, is the software that is used during data taking to monitor the state of the data acquisition and the quality of physics data when the beam is running. The ATLAS Trigger and Data Acquisition (TDAQ) consists of the HLT and the Data Acquisition system (DAQ). DAQ transports

selected events from the HLT to the mass storage. The online software is the subsystem of TDAQ. It encompasses configuration of TDAQ, the control framework and the monitoring of the Trigger-DAQ but it does not include the processing and transportation of physics data. It is essentially the "glue" that holds the various sub-systems together [60].

6.2.1 TDAQ performance in Run 1

To reduce the total data flow without losing interesting physics events ATLAS used a trigger system organized in three levels: level one called L1, level two L2 and then the Event Filter (EF). These three levels are shown in the Fig. 6.3. The L1 trigger, a hardware based trigger that was designed to reduce the event rate from 40MHz to 75kHz. This trigger selection is based on high p_T clusters and tracks from calorimeters and MS respectively. The $\phi\eta$ coordinates are provided here referred as the $Region\ of\ Interest(ROI)$ in the Fig. 6.3. The L1 trigger needed to be very fast so the reconstruction algorithms are implemented directly in the L1 hardware. The Level-1 is composed of the calorimeter trigger, the muon trigger and the Central Trigger Processor (CTP), which serves the Level-1 results to the detectors [60].

The L2 trigger, a software based trigger, it reduced the event selection per second from 75 kHz to 1 kHz. It selected 1 in 15 events to proceed to the EF. Algorithms that process data at the rate of 50ms per event to reconstruct leptons, photons and jets from the data coming from L1 were implemented here. L2 trigger decisions are based on these reconstructed objects.

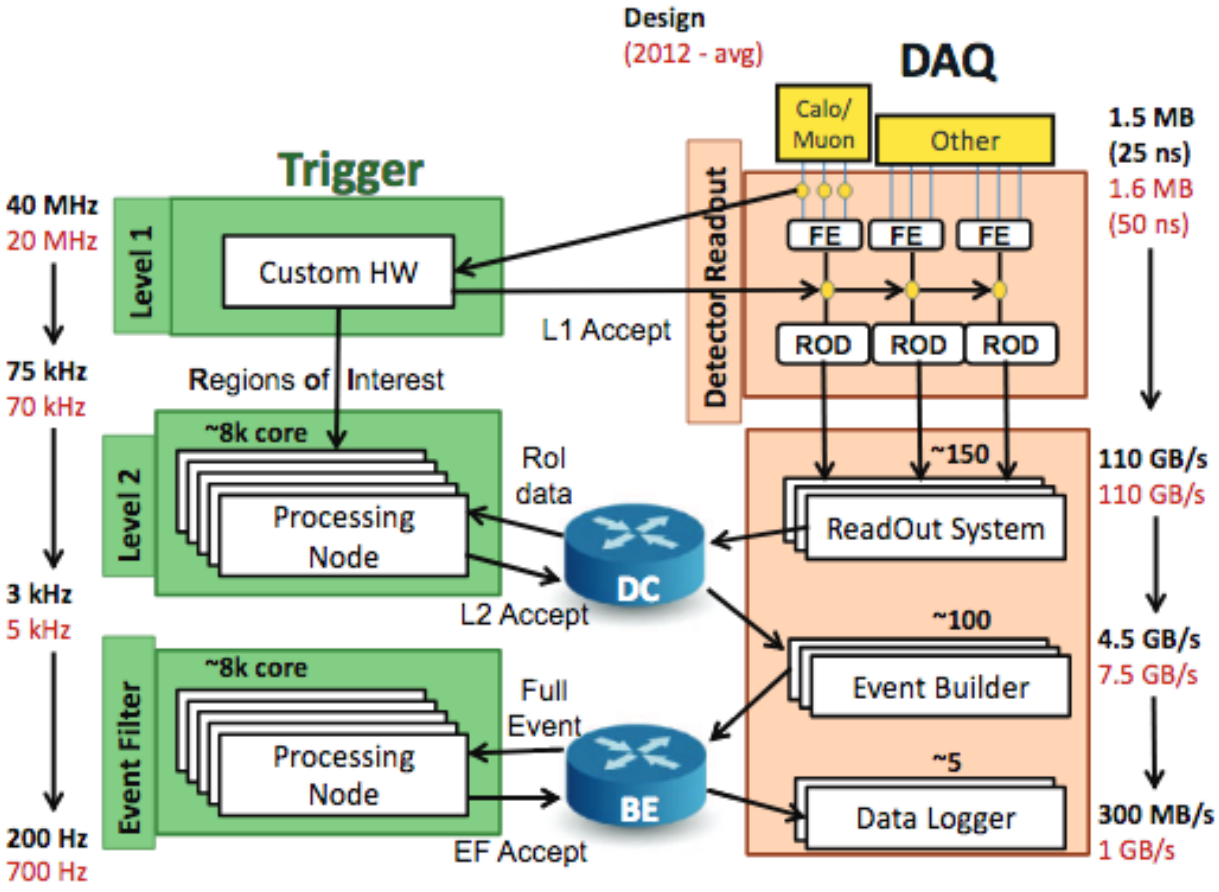

Figure 6.3: TDAQ architecture. The trigger path is sketched on the left, while the data acquisition one on the right. The design parameters are reported for each component in black, while in red are reported the average values in 2012 [60].

The Event Filter EF, the final stage in the trigger scheme, further reduced the data stream by using information of more complex reconstruction algorithms such as Bremsstrahlung recovery for electrons and vertex finding. It selected one in ten events coming from the L2 trigger, reducing the event rate to 1 kHz to 100 Hz. All events that passed the event filter are written to tape and stored at CERN and are available for physics analysis [56].

The ReadOut System (ROS) receives event fragments from the detector readout via $\approx$ 1600 optical links upon Level-1 acceptance [60].

The TDAQ system is based around two data networks, the Data Collection (DC) and the Back-End (BE), for different data traffics. By the time Run 1 ended, most of the components of the TDAQ system were operating beyond their predicted design values. Increased pile-up rates proved to be a big challenge to the TDAQ system highly effecting the HLT processing time and thus the computing power of the TDAQ system [60]. For this we needed upgrades to the ATLAS trigger system.

6.2.2 Trigger updates for Run-II

Since for Run-II, we operated the LHC at higher centre-of-mass energy and smaller bunch spacing of 25 ns, we expected higher luminosities and pile-up. To cope with these changes for Run-II, the three staged trigger system has been turned to a two staged system i.e L1 and the High level trigger (HLT) as shown in Fig. 6.4. L1 has new custom-made electronics, that finds regions of interest faster using coarse information from MS and calorimeters. The maximum acceptance rate has increased from 75 to 100 kHz. A new fast

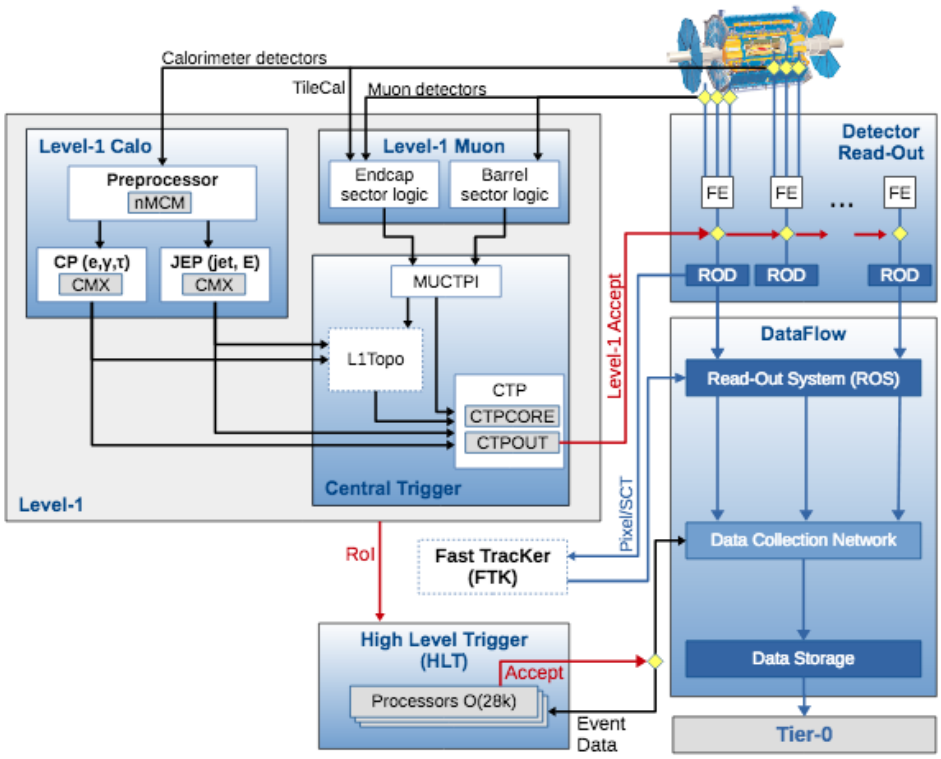

Figure 6.4: The ATLAS TDAQ system in Run-2 with emphasis on the components relevant for triggering [61].

tracking system (FTK) has been added to the L1 trigger hardware which would be operational from 2018. The FTK system provides global ID track reconstruction at L1 using associative memory chips for pattern recognition [61]. This FPGA-based track fitter performs a fast linear fit before inputting the tracks to HLT making track reconstruction procedures usable at much higher event rates. Two FPGA-based processor modules (L1-Topo) are also added to make event selection more robust and sophisticated.

The L2 and the EF farms are merged into a single HLT, changing it's entire architecture. This significantly reduced CPU and network usage, while providing a flexible combination of fast and detailed processing as shown in Fig. 6.4. To deal with the higher input flux from L1 and also to increase the output rate, the ROS system has also been upgraded.

The reconstruction and identification of physics object at trigger level is critical, inefficiencies in their reconstruction or too high kinetic thresholds could compromise a BSM discovery as well as precision measurements for SM parameters. For an efficient trigger we need a lower threshold and a higher particle selection efficiency. With the Run-II improvements on the TDAQ system and the better CPU management multivariate techniques are now being used at the trigger level which have lead to higher trigger efficiencies as shown in Fig. 6.5.

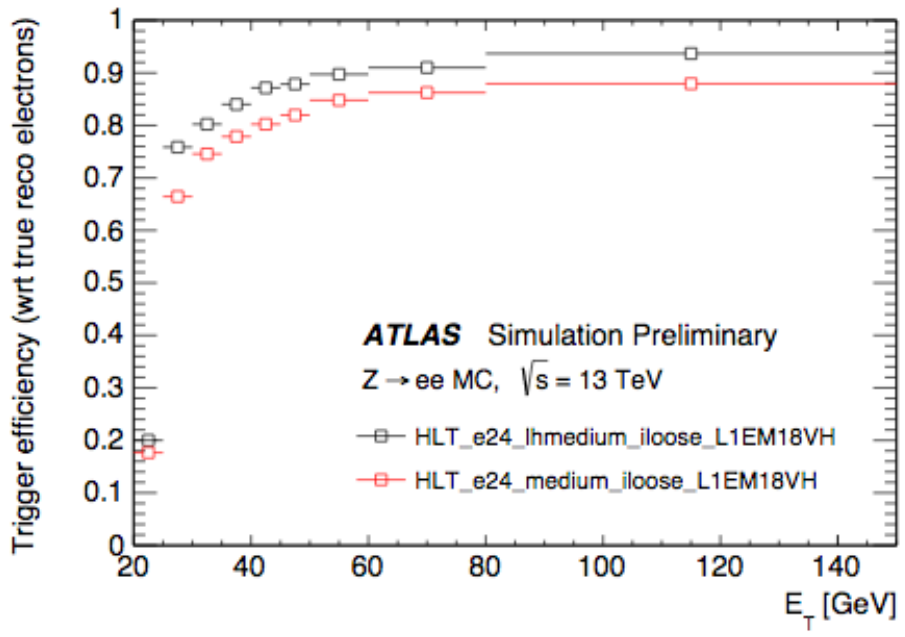

Figure 6.5: Comparison of the likelihood-base and the cut-base HLT electron triggers efficiency as a function of the offline electron candidates transverse energy E_T with respect to true reconstructed electrons in $Z \rightarrow ee$. The HLT_e24_medium_iloose_L1EM18VH trigger is the Run-1 algorithm requiring an electron candidate with $E_T > 24$ GeV satisfying the cut-based medium identification, while HLT_e24_lhmedium_iloose_L1EM18VH trigger corresponds to the Run-2 algorithm using the likelihood-based lhmedium electron identification. Both trigger chains also require the same track isolation selection and are seeded by the same level-1 trigger (L1EM18VH) [61].

The events selection for this analysis was done using a trigger logic that accepts events with a missing transverse momentum above 70 GeV (for data collected during 2015) or 90 to 110 GeV (depending on data taking period for

data collected in 2016). The trigger was 100% efficient for this event selection. Auxiliary data samples used to estimate the yields of background events were selected using triggers requiring at least one isolated electron with $p_T > 24$ GeV), muon ($p_T > 20$ GeV) or photon ($p_T > 120$ GeV) for data collected in 2015. For the 2016 data, the background events were selected using triggers requiring at least one isolated electron or muon ($p_T > 26$ GeV) or photon $p_T > 140$ GeV).

Chapter 7

ATHENA Software framework

The ATLAS collaboration has developed a software and middleware that enables data access to all physics analysis group independent of their geographical location. ATLAS offline software is called Athena. Offline software runs on the data once it's stored to produce objects for analysis. Athena has a C++ control framework in which data processing and analysis is performed. A framework is a skeleton of an application where programmers plug in their code. It provides common functionality and communication between different components. Athena framework is based on the GAUDI component architecture that was originally developed by LHCb. Athena is then the sum of this kernel framework, together with ATLAS-specific enhancements. Athena is used to refer to the framework and the name GAUDI is used to refer to the architecture upon which this framework is based.

7.1 ATHENA classes

The main Athena classes are divided into four categories:

- **Tools** should always inherit from a tool interface. Any function that should be visible from the outside has to be defined in the interface. Any additional public functions that are only defined in the tool (and not in the interface) can only be seen within a package.

- **Data Objects** are lightweight packages, intended only as containers of the information. Any analysis or calculation should again be implemented in a tool.

- **Algorithms** An algorithm is a C++ class that implements Athena. It takes input, manipulates it and gives us the results. All physics related tasks are implemented in Athena as algorithms.

- **Services** refer to classes that facilitate and provide utilities to algorithms and are globally available [62].

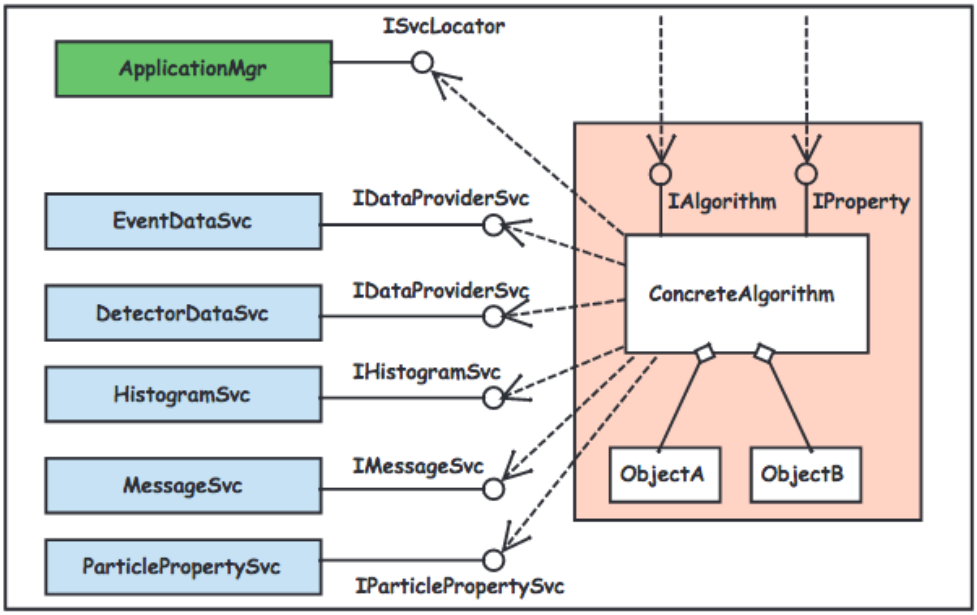

Figure 7.1: The main components of the ATHENA framework as seen by an algorithm object [62].

Scripts for the run-time control of code execution in Athena are written in Python. These scripts are called the "Job Options". The algorithms are configured and sequenced at run time using job options. A standard Athena job consists of three steps:

- Initialization: Loading of services and algorithms
- Execution: A list of algorithms run sequentially on each event, this is called the Event Loop.
- Finalization: Algorithms are terminated and data objects (results of the algorithms that can serve as an input to the subsequent algorithms) are deleted.

7.2 Definition of ATHENA Algorithm

This section is referenced from [62].

In algorithm base class we have, the initialization of certain internal pointers, include directives, forward declarations and private member variables, a constructor and a destructor, the IAlgorithm interface, a subalgorithm identification and a whole series of declaring properties.

- **Constructor and Destructor** The constructor takes two arguments, the first is the name that will identify the algorithm object being instantiated and the second is a pointer to the interface.

- **The IAlgorithm Interface** Three methods must be initialized by the interface class initialize(), execute() and finalize() virtually which are implemented by the derived algorithm classes. Derived algorithm classes are the ones that are specifically designed for a purpose. These derived classes implement the methods of the IAlgorithm interface, and declare the algorithm's properties of the Algorithm base class.

- **Service accessor methods** In the initialize section of the algorithm, we declare accessor methods which return pointers to key service interfaces. These services are only accessible after the algorithm has been initialized. The services which they refer to are recognizable easily by names.

- **Creation of sub algorithms** These are defined as StatusCode create subalgorithm function specified by a type and name.

- **Declaration and setting of properties** Here the algorithm must declare it's properties to the framework using the declareProperty() method. The Algorithm base class then uses the setProperties() method to tell the framework to set these properties to the values defined in the job options file.

- **Filtering**

  If we have a list of algorithms (sequence) where we wish to execute these algorithms in a way to see a particular reconstruction signal for example. Each algorithm may make a filtering decision, based on some characteristics of the event which we decide, that can either allow or bypass processing of the downstream algorithms in the sequence. The filter decision may also cause a branch whereby a different downstream sequence of Algorithms will be executed for events that pass the filter decision relative to those that fail it.

ATLAS Software is organized into a hierarchical structure of "Projects" and "Packages". Inside each project, software is divided into packages. The main domain for packages are generators, inner detector software, common tracking software etc. A package is the basic unit of the offline software. Each package has a name, a path and a "Tag number" as a suffix at the end of it's name. This tag number distinguishes different versions of that package. Each version of a project has a "release number" and there is an overall Release number that identifies a complete collection of packages. Package Tags are updated frequently but production of a whole new release happens after few months [63].

7.3 Monte-Carlo Event Generators

Several phenomena happen after the p-p collisions which need to be emulated in the simulation of an event to understand the physics behind them. A schematic illustration is shown in the Fig. 7.2 below:

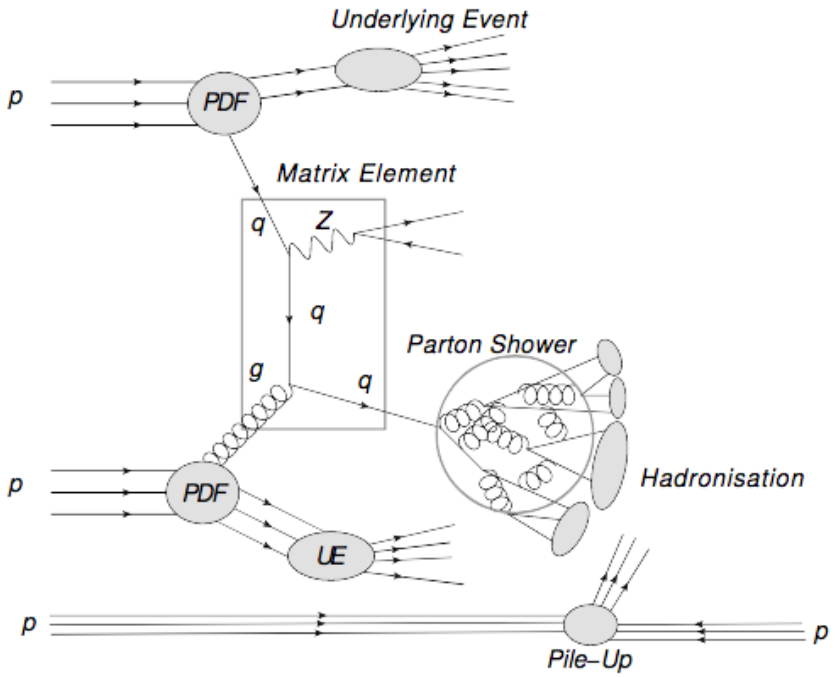

Figure 7.2: Schematic picture of a p-p collision. Shown are the incoming protons and their parton content described by the PDFs, the partonic interaction given by the ME, the PS and hadronization of the quarks and gluons in the event and additional activity in the event originating from the underlying event and pile-up [64].

At ATLAS, a detailed Monte Carlo (MC) simulation is performed for the signal and the background processes to include all of the QCD interactions and underlying W, Z and *top* events. Using the factorization theorem [65] we could divide the differential cross section in separate parts mentioned in the Fig. 7.2. **Parton distribution functions (PDFs)** of the incoming partons and their contents are an important factor for calculating a p-p interaction cross section. The PDFs give the probability of finding a parton with a certain fraction of proton's momenta inside the proton. Different strategies can be used in measurements for calculations of PDF and these choices influence the predictions of the simulation generators. The **Matrix Element** describes the hard scattering processes using the QCD and QED with the help of the Feynman rules. They are not normally not calculated beyond next-to-leading orders (NLO) in the generators due to computer power contraints. **Proton showers** connect the matrix element calculations at the parton level with the observed hadrons. Hadronization is the formation of hadrons when the new partons cannot be further described by the parton showers. The **underlying event** provides additional interactions other than parton showers and hadron scattering [64].

All these effects are included in the Monte-Carlo (MC) generators from the hard short-distance physics to the long wavelengths of hadronization and hadron decays. General purpose detector start from low-order (LO or NLO) descriptions of the perturbative hard physics and then attempt to include the "most significant" corrections, such as higher-order matrix-element corrections and parton showers, resonance decays and finite-width effects, underlying event, beam remnants, hadronization, and hadron decays [66].

The main five MC generators used in this analysis are:

- **SHERPA** Originated in studies of the matching of hard-emission matrix elements with parton showers at NLO precision level. Therefore it is a preferred generator for processes with additional jets.
- **HERWIG** Originated in perturbative coherence studies, is used for angular-ordered parton shower productions [66].
- **PYTHIA** This is a multi-purpose generator that does hadronization studies at LO matrix element level. The proton showers and underlying events are implemented using Lund's string fragmentation model [66].
- **POWHEG** also provide NLO matrix element calculations. It then gets the proton shower description by interfacing with PYTHIA.
- **MADGRAPH**5_*MC*@**NLO** provides matrix element calculations up to LO [64]. Similarly to POWHEG it is then interfaced with PYTHIA or HERWIG. It is used for systematic uncertainties calculations.

7.4 Full MC production chain

For MC events production a Full Chain of steps needs to be taken from Generation to production of Analysis Object Data (AOD), this is called 'Full Simulation' shown in the Fig. 7.3. Input for 'simulation' stage comes from the event generators like PYTHIA and HERWIG in the "Event Generation" stage. Data objects representing Monte Carlo truth information (HepMC) from the generators are read by simulation and processed. Digitization is the

process whereby the GEANT4 Hits from the simulation are then subjected to the response of the detector to produce Digitized hits, as produced in the Raw Data from the real detector. Hits produced by the simulation can be directly processed by the digitization algorithm and transformed into Raw Data Objects (RDOs). During the reconstruction, the digitized RDOs, such as times and voltages, are reconstructed into tracks and energy deposits as Event Summary Data (ESD) files. ESD are very big data files and are obsolete now. Analysis Object data (AOD) files or Derived Analysis object data (DAOD) files are their summary and smaller in size are commonly used in analyses.

ATLFAST the ATLAS Fast MC production chain is an approach implemented parallel to digitization and reconstruction to decrease the huge CPU usage cost, in the integrated simulation framework (ISF). This uses techniques like "frozen showers" and "fast simulation of a particles interaction with the ATLAS (FATRAS)" to enables the production chain to simulate in detail only the parts of the event which are relevant to the analysis being done and use the faster alternatives for the rest [68].

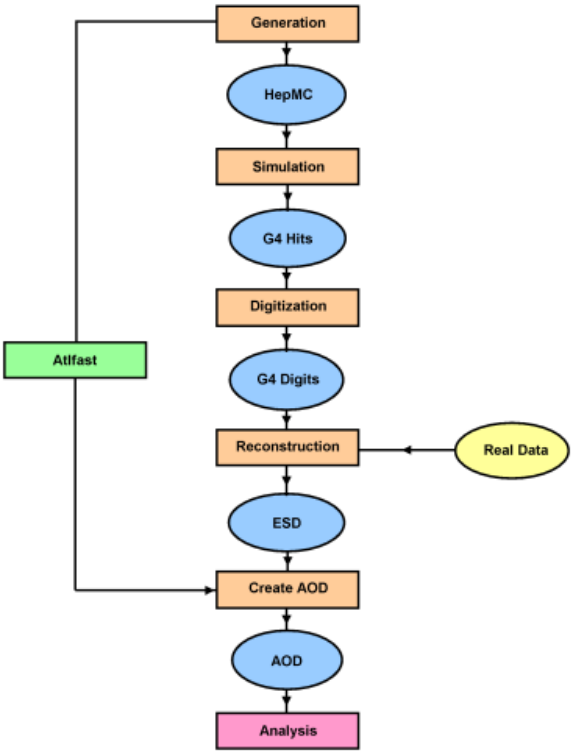

Figure 7.3: Schematic representation of the Full Chain Monte Carlo production [67].

Part III

From m_T to Recursive Jigsaw

Truth is found neither in the thesis nor the antithesis, but in an emergent synthesis which reconciles the two.

Georg Wilhelm Friedrich Hegel

Chapter 8

Mass bound Variables

If we ever discover NP at the LHC the first order of business would be to measure the mass of the new particle. This deceptively simple task turned out to be a notoriously difficult challenge which we are trying to explain in this chapter. Almost all mass measuring techniques which have been developed through the years follow these three steps:

- The postulation of a decay topology applied on the NP production process of the particle whose mass is being measured.
- Identification of the final state variables or observables which will be most successful in distinguishing the signal from the background. Basically the typical set of observables from the detector are the four-momenta of objects which together with their topology and probabilities hypothesis can be used to make inferences on the masses of the particles.
- Using these variables we can put constraints on the measurements of the

desired particle mass. For example kinematic endpoints or a fit to the shape of a differential distribution from a large number of events [69].

There are some general ambiguities like combinatoric ones with identical pair production of particles like in R-parity conserving SUSY signals and we are not sure which decay chain they belong to, the initial state radiations (ISR), intermediate state particles that leave the identities of particles in the final state permuted or if the decay topology matches the reality. These ambiguities are resolved differently by different mass measuring techniques which will be discussed in the next sections.

8.1 Near or On-Shell Particles Mass Measurement

On or near threshold particle production can be observed with using variables that scale approximately at the energy scale of the event. For SUSY-like events where we have on-shell massive particles decaying to two invisible particles per each step in a long decay chain, we can try to identify and calculate the unknown individual four-momenta and energies of all the decay products and construct an invariant mass peak. We can then do a "bump hunt" for NP over the relatively smooth background continuum. This method is independent of any type of assumptions on the interactions, the decay topology and the intermediate particle produced [69].

The definition for "effective mass" (M_{eff}) in terms of scalar sum of the transverse momenta of jets and the missing transverse momenta p_T^{miss} is given

as:

$$M_{\text{eff}} = \sum_{N} |P_{T,N}| + p_T^{\text{miss}} \tag{8.1}$$

where N is analysis specific [69].

Another variable used for on shell mass measurement techniques very similar to M_{eff} is the H_T defined as the sum of the transverse momenta of all the jets in the final state:

$$H_T = p_{T(1)} + p_{T(2)} + p_{T(3)} + p_{T(4)} + ... \tag{8.2}$$

Another variable for measuring invariant masses for above mentioned SUSY-like particles produced on shell which also takes no assumptions about the underlying event structure and is generally model independent is the $\sqrt{s}_{\text{min}}$ defined in ref. [70] as,

$$\sqrt{s}_{\text{min}}(M_{\text{inv}}) = \sqrt{E^2 - P_Z^2} + \sqrt{(E_T^{\text{miss}})^2 + M_{inv}^2} \tag{8.3}$$

$\sqrt{s}_{\text{min}}$ is a function of M_{inv} the sum of masses for all the final state invisible particles, an unknown parameter. Although $\sqrt{s}_{\text{min}}$ is defined in a fully inclusive manner and takes in longitudinal information as well, it is highly effected by ISR and multiple parton interactions.

These mass techniques although very simple since they don't require individual momentum or masses of the invisible particles in the final state. In their model independency they loose any specific characterization of the event and become sub-optimal for more complex event topologies [71].

8.2 Mass measurement for two body Visible and Semi-invisible decays

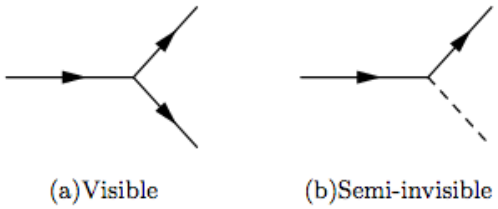

Figure 8.1: Topologies for two body visible decay and two body visible and invisible particle decay [69].

The first figure in the diagram 8.1 is a visible two body decay similar to $Z \rightarrow e^+e^-$. The mass of Z is calculated using the sum of squares of the fully visible four-momenta of the daughter particles in Eq.8.4:

$$M_z^2 = (\mathbf{p}_{e^+} + \mathbf{p}_{e^-})^2 \tag{8.4}$$

This formula however cannot be applied to calculate mass of a particle that has invisible or weakly interacting particles in it's decay chain. For example for $W \rightarrow l\nu$ the neutrino goes unobserved and gives rise to missing momenta. This means to observe the mass of W the four-vectors missing momentum needs to be studied. For LHC, the boost along the beam axis of the collision centre-of-mass is not known, constraining the information that can be gathered about the missing momentum. To decrease the number of unknown degrees of freedom for the missing energy a projection of the energy

or momentum is done into the plane transverse to the beam [73]. The experiment UA(1) discovered the W particle using the the explicit construction of the transverse mass M_T [74],

$$M_T^2 = 2(E_{(T,vis)}E_{(T,inv)} - \mathbf{p}_{(T,vis)}\cdot\mathbf{p}_{(T,inv)}) \leq M_W^2 \tag{8.5}$$

where $E_{(T,inv)}^2 = \mathbf{p}_{(T,inv)}^2$. The equality in the equation Eq.8.5 is only possible when both the lepton and neutrino are produced with the same rapidity [69]. As $M_T \leq M_W$ the mass of the W boson is determined from the endpoint of the population boundary called the "kinematic edge". This distribution is shown in Fig. 8.2.

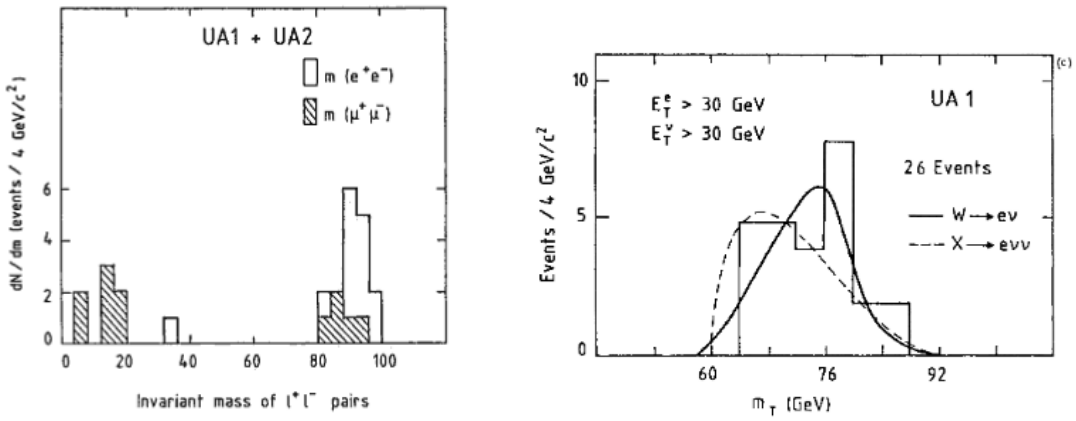

Figure 8.2: (left) Dilepton invariant mass distribution for $Z \to l^+l^-$. (right) The transverse mass distribution showing a peak at the W mass. The two curves show the results of a fit to the hypothesis $W \to e\nu$ and $X \to e\nu\nu$ [12].

M_T though has model dependence as the precise fraction of events which occur with M_T close to M_W are dependent on how the W boson decays and

the physics behind the production of the W boson and can only be applied when one parent particle is decaying in one or more step to one invisible particle.

8.3 Mass measurement for Identical semi invisibly decaying particles

In R-parity conserving SUSY signals we have two identical pair produced particles decaying to two LSPs and visible SM particles as shown in Fig. 8.3. For these cases we cannot use the transverse mass variable anymore.

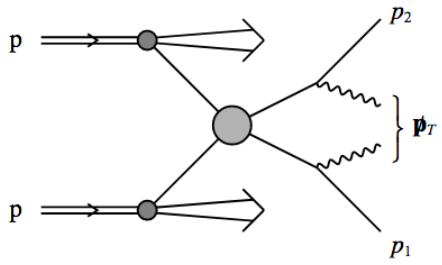

Figure 8.3: A generic illustration of hadron collisions which leads to the production of particles that decay to visible particles p_1 and p_2 and the invisible particles that contribute to the missing transverse energy [72].

When we have a pair of particles being produced in the collision which individually decay to visible and invisible parts, combinatorial ambiguities arise, since it is no longer generally possible to associate a particular visible particle with one or other of these decay chains. Also, the missing transverse

momenta is the sum of the transverse momentum of both invisible particles and constraints are applied which link the two chains together.

Squark production also follows the pattern shown in the Fig. 8.3,

$$\tilde{q} \rightarrow q\tilde{\chi}_1^0 \tag{8.6}$$

for arbitrary momenta we can write,

$$m_{\tilde{q}}^2 = m_q^2 + m_{\tilde{\chi}_1^0}^2 + 2(E_{T,q}E_{T,\tilde{\chi}_1^0}\cosh(\Delta\eta) - \mathbf{p}_{T,q}\mathbf{p}_{T,\tilde{\chi}_1^0}) \tag{8.7}$$

where

$$E_T = \sqrt{\mathbf{p}_T^2 + m^2} \tag{8.8}$$

$$\eta = \frac{1}{2}\ln[(E + p_Z)/(E - p_Z)] \tag{8.9}$$

and $\Delta\eta$ is the rapidity difference between q and $\tilde{\chi}_1^0$ and is a Lorentz invariant quantity.

As $\cosh(\Delta\eta) \geq 1$,

$$m_{\tilde{q}}^2 \geq m_T^2(\mathbf{p}_{T,q}\mathbf{p}_{T,\tilde{\chi}_1^0}) \approx m_q^2 + m_{\tilde{\chi}_1^0}^2 + 2(E_{T,q}E_{T,\tilde{\chi}_1^0}\cosh(\Delta\eta) - \mathbf{p}_{T,q}\mathbf{p}_{T,\tilde{\chi}_1^0}) \tag{8.10}$$

Since mentioned before $p_T^{\text{miss}} = \mathbf{p}_{T,\tilde{\chi}_{1,a}^0} + \mathbf{p}_{T,\tilde{\chi}_{1,b}^0}$

$$m_{\tilde{q}}^2 \geq \max\left\{m_T^2(\mathbf{p}_{T,q(a)}\mathbf{p}_{T,\tilde{\chi}_{1,a}^0}), m_T^2(\mathbf{p}_{T,q(b)}\mathbf{p}_{T,\tilde{\chi}_{1,b}^0})\right\} \tag{8.11}$$

and since the splitting in the p_T^{miss} is unknown

$$m_{\tilde{q}}^2 \geq M_{T2} \equiv \min_{\sum_{p_T^{miss}}}\left[\max\left\{m_T^2(\mathbf{p}_{T,q(a)}\mathbf{p}_{T,\tilde{\chi}_{1,a}^0}), m_T^2(\mathbf{p}_{T,q(b)}\mathbf{p}_{T,\tilde{\chi}_{1,b}^0})\right\}\right] \tag{8.12}$$

where minimization is over all combinations of $p_T^{\text{miss}} = \mathbf{p}_{T,\tilde{\chi}^0_{1,a}} + \mathbf{p}_{T,\tilde{\chi}^0_{1,b}}$. M_{T2} is a lower bound on the maximum of the two transverse masses of the parent particles over an unknown split between $\tilde{\chi}^0_{1,a}$ and $\tilde{\chi}^0_{1,b}$.

8.3.1 Mitigating the upstream component

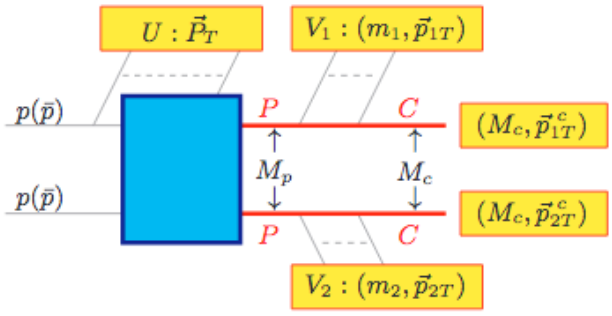

Figure 8.4: The generic event topology where the visible objects that are the upstream jets, the parent particles V_i and the total transverse momentum of the missing particles M_c are mentioned in yellow [75].

In general, the parent pair may be accompanied by a number of additional upstream objects like initial state radiation jets (ISR) or decays of even heavier particles up the decay chain. To remove these effects from the momenta measurements, 1 dimensional decomposition is applied on the M_{T2} into $M_{T2\perp}$ and $M_{T2||}$ where $M_{T2||}$ is constructed from components parallel to the upstream momenta (ISR) and $M_{T2\perp}$ is perpendicular to it and thus has no dependence on it [69]. This method also allows a direct measurement of the child particle $m_{\tilde{\chi}^0_1}$ and thus result in a true parent mass $m_{\tilde{q}}$ from the above example [75].

However like M_{eff}, M_{T2} does not depend on the physics process used in generating it and a priori, it cannot be said that M_{T2} could be useful for the mass measurement of the physics process being studied. Even if we can formulate $m_{\tilde{\chi}}$, M_{T2} function dependence on $m_{\tilde{\chi}_1^0}$ cannot be predicted. In general $M_{T2}(\tilde{\chi}_1^0)$ could rise, fall, or even be stationary w.r.t $\tilde{\chi}_1^0$ [76].

8.3.2 Contraverse Mass Variable M_{CT}

To remove the dependence of M_{T2} on $\tilde{\chi}_1^0$, the variable M_{CT} was suggested [77]. Consider that parent particles p_i are produced in a centre-of-mass rest frame F_0 and then are boosted to different frames F_0 and F_1 where the boost applied here is equal and opposite in direction to F_0. The quantity that is invariant in such a contralinear boost is called the contraverse mass M_{CT} given as [77],

$$M_{CT} \equiv [E(p_1) + E(p_2)]^2 - [\mathbf{p}(p_1) + \mathbf{p}(p_2)]^2 \tag{8.13}$$

$$= m^2(p_1) + m^2(p_2) + 2[E(p_1)E(p_2) + \mathbf{p}(p_1)\mathbf{p}(p_2)]. \tag{8.14}$$

This insensitivity to the boost in the contralinear direction is desirable in the for the magnitude of those boosts would be unknown and immeasurable if there are invisible daughter particles produced [69]. M_{CT} does not give the mass of the particle decaying to p_1 and p_2 but in the absence of visible ISR and if the visible particles are massless, it gives an endpoint at,

$$M_{CT}^{\max} = \frac{m_{\text{parent}}^2 - M_{\text{inv}}^2}{M_{\text{inv}}} = 2k^* \tag{8.15}$$

where k^* is the momentum of the daughter particle in the frame of parent particle. This gives an equation of constraints between parent and daughter

particle masses and as described in [77], that if we could do this analysis at various stages along the symmetric decay chain all the masses could be determined [78].

If the visible particles are identical which is the case we are studying here $m(v_1) = m(v_2) = m(v)$, the above equation is given as [79],

$$M_{CT}^{\max}(m(v)^2) = \frac{m(v)^2}{m_{\text{parent}}} + \frac{m_{\text{parent}}^2 - M_{\text{inv}}^2}{M_{\text{inv}}}. \tag{8.16}$$

The measurement of the gradient and intercept of the function $M_{CT}^{\max}(m(v)^2)$ allows the mass of the parent and the invisible daughter to be measured independently [79].

To avoid the smearing of the endpoint of the above Eq.8.16 due to upstream radiation $M_{CT\perp}$ was suggested in [80] which is invariant under the boost acquired from the recoil against the upstream transverse momentum. Another variant of M_{CT} similar in construction to M_{T2} was introduced in [81],

$$M_{CT2} = \min_{\sum_{p_T^{\text{miss}}}}(\max\{M_{CT}, M'_{CT}\}). \tag{8.17}$$

This variable has a Jacobian which increases the density of events near the endpoint $M_{CT}^{\max}$ [69]. But this turned out not to be useful when the SM background was found to be peaking at this endpoint as well as shown in Fig. 8.5 [82].

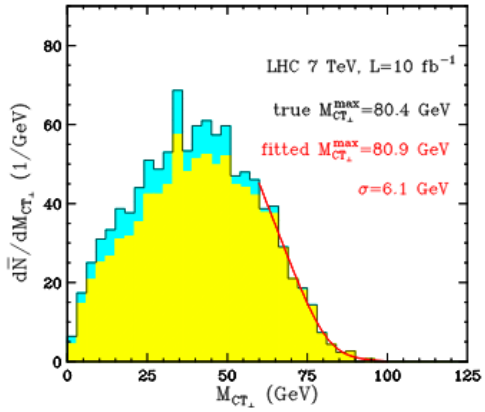

Figure 8.5: Zero-bin subtracted $M_{CT\perp}$ variable distribution after cuts, for $t\bar{t}$ dilepton events. The yellow (lower) portion is our signal, while the blue (upper) portion shows $t\bar{t}$ combinatorial background with isolated leptons arising from τ or b decays [80].

8.3.3 Separation of decay chains; Hemisphere m_{T2} vs m_{TGEN}

To resolve the combinatorial ambiguity about which side of the pair produced event decay chain the reconstructed final state particles were coming from two parallel methods were introduced. The "m_{T2} hemisphere method" which used the recursive hemisphere reconstruction algorithm defined in Ref. [84] as:

- Compute two initial axes, the first one is chosen as the direction of the highest momentum object and the second one as the as the direction of the object with the largest $p.\Delta R$ w.r.t to the first where the $\Delta R =$

$\sqrt{(\Delta\phi)^2 + (\Delta\eta)^2}$. The axes are chosen as the directions of the pair of objects which have the largest invariant mass.

- Associating objects (jets and leptons) to these axis where the object has the smallest angle to the object and the hemisphere squared masses are minimum.

- Recalculating the axes as the sum of the momenta of all the connected objects. In order to converge to a stable solution, the axes are only updated after a full iteration is performed.

- Iterating the association until no objects switch from one group to the other.

Ref. [83] used this grouping algorithm on the cascade decay products from a squark or a gluino to see the m_{T2} endpoint. The m_{T2} kinematic edge however was smeared by the misidentification of hemispheres as shown in Fig. 8.6 and the systematic uncertainties arising from the fitting functions.

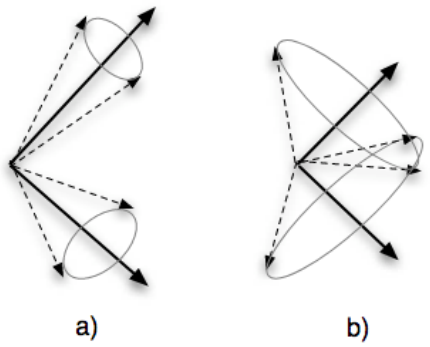

Figure 8.6: Kinematical configurations for (a) $m_{\text{vis}} \approx m_{\text{vis}}^{\text{min}}$ and (b) $m_{\text{vis}} \approx m_{\text{vis}}^{\text{max}}$. When m_{vis} is large the jets in the hemisphere are less collinear and the hemisphere algorithm likely misgroups the particles [83].

M_{TGEN} is the smallest value of the M_{T2} obtained after trying all possible combinations of visible momenta (excluding the effects of ISR and multiple parton interactions) between the two decay chains. The M_{TGEN} endpoint gives a constraint on the parent particle mass as a function of a hypothesized daughter particle masses like m_{T2}. However the time and computational cost for m_{TGEN} was a downside as the minimization of m_{T2} for each event had to be repeated 2^N time, where N is the number of partitions of the particles in that event, for the calculation of M_{TGEN} [85]. Also the bound was much lower than the true mass.

8.4 Razor variables

There are three kinds of frame relevant to decay chains in the LHC: the lab frame where the p-p collisions happen, the centre-of-mass frame for the pair

production PP to occur at rest and the two decay frames $P_a \rightarrow V_a I_a$ and $P_b \rightarrow V_b I_b$. The razor variable construction method assumes that we have massive parent particles produced at or near threshold because as mentioned before the PDFs fall of with centre-of-mass energy (CM).

For each event we preform a clustering of the selected leptons and jets in the event into two distinct hemispheres called "Megajets". The restframe of the visible system is defined by summing up the four-momenta of all the physics objects in all possible combinations. The combination that minimizes the sum of the invariant mass of the two megajets is selected. Then these collections are treated as single objects and have no overlap.

A Razor frame R is defined by the longitudinal boost β_L from the lab frame to where the visible decay products have equal and opposite z-momentum,

$$\beta_L = \frac{p_1^z + p_2^z}{E_1 + E_2} \tag{8.18}$$

where p_i^z are the z-th component of the momenta and E_i are the energies of the visible decay products [86]. In this R-frame: $2E_i = M_\Delta$. This is valid in the case where the parent particles are produced on threshold and CM frame $\approx$ lab frame.

The longitudinally boost invariant mass in R-frame is defined as:

$$M_R^2 = (E_1 + E_2)^2 - (p_1^z + p_2^z)^2 \tag{8.19}$$

which peaks near M_Δ for $p_1^z = -p_2^z$ similar to M_{CT}. Now to measure the transverse measure of the M_R variable motivated by the fact that the background with have no invisible component will have P_a and P_b back to

back:

$$(M_T^R)^2 = \frac{1}{2}\left[E_T^{\text{miss}}(p_{1T} + p_{2T}) - \overrightarrow{E}_T^{\text{miss}}.(\overrightarrow{p}_{1T} + \overrightarrow{p}_{2T})\right] \tag{8.20}$$

This variable has a kinematic edge at $M_T^R \leq M_\Delta$ for signal events. The dimensionless ratio of these two variables is:

$$R^2 = (\frac{M_T^R}{M_R})^2 \tag{8.21}$$

This is used for discriminating between QCD background and the signal where for signal $R \approx 1$ and for background $R \approx 0$. However in the case where $M_p \approx M_I$ the signal starts to look like background. The transition is gradual though and generally opens sensitivity to regions with low M_Δ [87].

8.5 Super-Razor variables

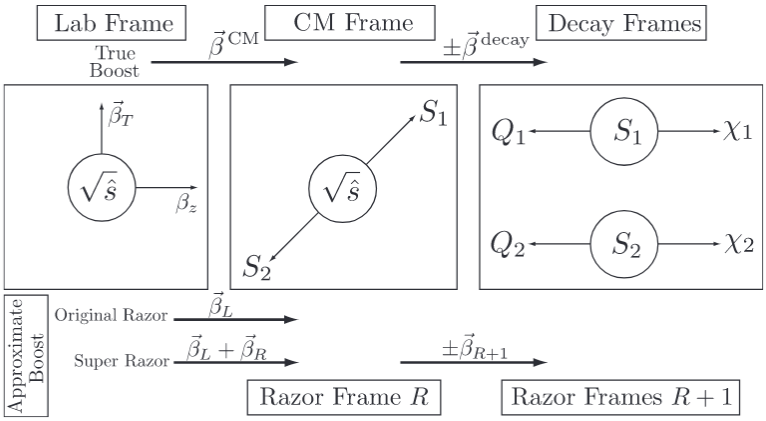

Figure 8.7: Sketch of the three sets of frames relevant to the razor reconstruction: the lab frame, the pair production frame and the two decay frames.The approximate razor frame identified with each physically relevant frame is also shown with the actual and approximate boosts from one frame to the next. By convention, we label each boost by the destination frame. Figure from [86].

Up till now in our razor frame construction techniques ISR and MPI were ignored. If these effects are included the parent particles are boosted ans no longer being produced on threshold. If we take the sum of transverse momenta of all decay products as show in the Fig. 8.7 last frame as:

$$\overrightarrow{J}_{\rm T} = -E_T^{\rm miss} + p_{T1}^{\rm vis} + p_{T2}^{\rm vis} \tag{8.22}$$

Now in this case to get to the razor frame or the pair production frame we add an additional boost factor which accounts for the recoil against the

ISR to the longitudinal boost from Eq.8.18 i.e.

$$\beta_R = \frac{-\overrightarrow{J}_T, p_z^r}{\sqrt{|\overrightarrow{J}_T|^2 + |p_z^r|^2 + \hat{s}_R}} \tag{8.23}$$

To simplify the reconstruction of the CM energy $\sqrt{\hat{s}_R}$ we make two assumptions:

- The invariant mass of the visible system is equal to the invariant mass of the invisible system.
- $\partial\sqrt{\hat{s}_R}/\partial p_z^R = 0$

We find,

$$\frac{\hat{s}_R}{4} = \frac{1}{2}\left(M_R^2 + \overrightarrow{J}_T.(\overrightarrow{p}_{T1}^{\text{vis}} + \overrightarrow{p}_{T2}^{\text{vis}}) + M_R\sqrt{M_R^2 + 2\overrightarrow{J}_T.(\overrightarrow{p}_{T1}^{\text{vis}} + \overrightarrow{p}_{T2}^{\text{vis})}}\right) \tag{8.24}$$

Then the boost from the pair production/R-frame to the decay frame is given as:

$$\beta_{R+1} = \frac{\overrightarrow{p}_{R1}^{\text{vis}} - \overrightarrow{p}_{R2}^{\text{vis}}}{E_{R1} + E_{R2}} \tag{8.25}$$

The p_{R1}^{vis} and p_{R2}^{vis} come from the R-frame. This equation 8.25 has the right symmetry that the boost to the decay frame of S_1 is the negative of the boost to the decay frame of S_2. The β_{R+1} and the $\sqrt{\hat{s}_R}$ are related to the M_Δ of the visible objects by the razor variable:

$$M_\Delta^R = \frac{\sqrt{\hat{s}_R}}{2\gamma_{R+1}} \tag{8.26}$$

where γ_{R+1} is the Lorentz factor associated with the boost β_{R+1}. This variable gives a kinetic edge at M_Δ as shown in Fig. 8.8 [86].

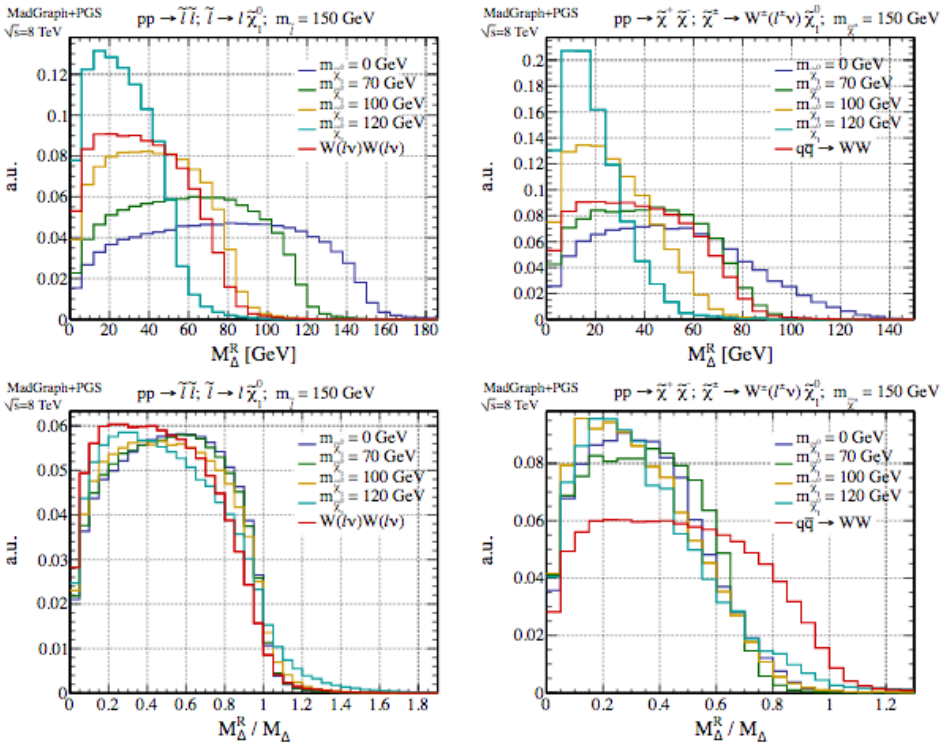

Figure 8.8: Upper row:Distributions of M_Δ^R or a 150 GeV slepton (left) or chargino (right) and a range of neutralino masses. Also shown is the W^+W^- background for which $M_\Delta = m_W$. Bottom row: Distributions of M_Δ^R normalized to M_Δ for selectrons (left) and charginos (right), again for a range of neutralino masses.

The total energy of the R-frame is the CM energy variable $\sqrt{\hat{s}_R}$ which can be divided in three parts:

$$\frac{\hat{s}_R}{4} = (M_\Delta^R)^2 + (p_{R1} + p_{R2})^2 + (E_{R1} - E_{R2})^2 \tag{8.27}$$

Using the above components we could write a dimensionless variable:

$$|cos(\theta_{R+1})|^2 = \frac{(E_{R1} - E_{R2})^2}{\hat{s}_R/4 - (M_\Delta^R)^2} = \frac{\hat{s}_R/4 - (M_\Delta^R)^2 - (p_{R1} + p_{R2})^2}{\hat{s}_R/4 - (M_\Delta^R)^2} \tag{8.28}$$

This angle is interpreted as the measure of the energy difference between the two visible particles which is useful in rejecting the background. Another variable $\Delta\phi_R^\beta$ is defined as the azimuthal angle between the sum of the visible particle momenta $p_{R1}+p_{R2}$ and the boost β_R in the R-frame. This variable is uncorrelated with the M_Δ^R, and $cos(\theta_{R+1})$ and is used in compressed spectra analysis and removing QCD background.

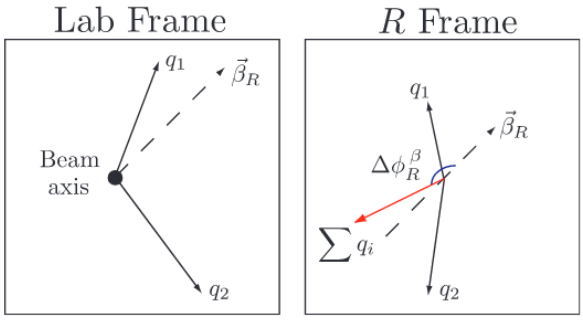

Figure 8.9: The definition of the azimuthal angle $\Delta\phi_R^\beta$ between the sum of visible momenta and the R-frame boost. The direction of the boost β_R from the lab frame to the R-frame is also shown here.

Although the mass variables M_Δ^R and $\hat{s}_R$ are somewhat similar to the mass variables discussed before, the angular variables $cos(\theta_{R+1})$ and $\Delta\phi_R^\beta$ are unique in their use of razor boosts. Using these set of variables we approximate the CM frame for the event and define an extra set of variable to analyze the system.

8.6 A comparison between $M_{CT\perp}$, M_{T2} and Super-razor variables

All three of the variables represent the M_Δ construction for the signal event with a sharp edge or end point at the true value. Both $M_{CT\perp}$ and M_{T2} are invariant for the effect when the parent particles are not produced on shell. The invariance in M_{T2} comes from the minimization and for $M_{CT\perp}$ it comes from the consideration of only the kinematics along the transverse axis perpendicular to $p_T^{\rm CM}$. In super-razor technique, for M_Δ^R we calculate the boost from the laboratory frame to the CM frame and by using only Lorentz invariant information in the determination of this transformation, the definition of the resulting reference frame is stable under variations of $p_T^{\rm CM}$.

Since $M_{CT\perp}$ only chooses events along one axis, half of the time it's value sits at zero. So effectively it uses only half of the dataset. M_{T2} has though fewer events sitting at zero but it increases for larger $p_T^{\rm CM}$ or for higher jet multiplicities or boosted topologies as shown in Fig. 8.10.

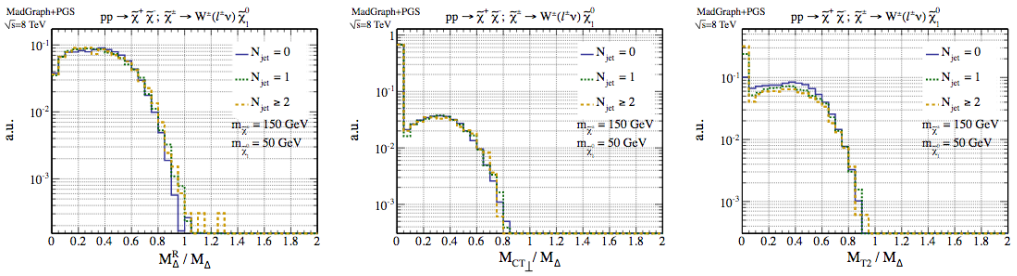

Figure 8.10: Distributions of M_Δ estimating variables for charginos with mass 150 GeV decaying into 50 GeV neutralinos and leptonically decaying W bosons, as a function of jet multiplicities. Variables include M_Δ^R (left), $M_{CT\perp}$ (center) and M_{T2} (right), all normalized to the true value of M_Δ for each sample [86].

Figure 8.11 shows the results of the analysis done in [86] for sleptons and charginos and comparing results for mass variables M_Δ^R,$M_{CT\perp}$ and M_{T2}. CMS analysis using M_Δ^R clearly outperforms $M_{CT\perp}$ while ATLAS analysis with M_Δ^R is slightly better than the one with M_{T2}.

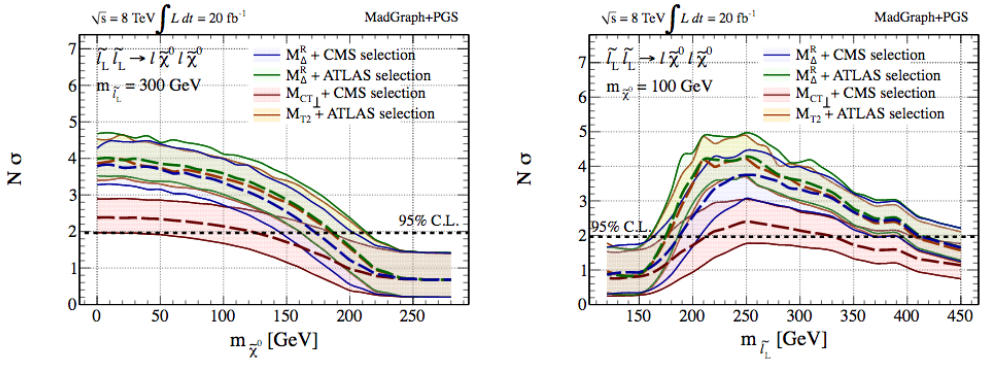

Figure 8.11: Expected exclusion limits in $N\sigma$ or left-handed selectrons decaying to leptons and neutralinos using $20 fb^{-1}$ of 8 TeV data as a function of neutralino mass with 300 GeV selectrons (left) or as a function of selectron mass with 100 GeV neutralinos (right). Expected limits are calculated for M_{Δ}^{R} using CMS (blue) and ATLAS (green) selection cuts and compared with exclusions from CMS $M_{CT\perp}$ (red) and ATLAS M_{T2} (orange) [86].

Chapter 9

Recursive Jigsaw Technique

The Z_2 symmetric phenomenology of R-parity conserving SUSY implies that there must be an even number of new particles produced and that they are produced in pairs. Furthermore, they decay through specific channels to the lightest weakly interacting particle that is stable and hence does not decay into SM particles. These detector invisible particles can be inferred from the missing energy calculations but there are many limitations in measuring the four-momenta of these particles. Crucial information about the identification and observation of these particles is lost due to these detector limitations. Various techniques were discussed in the previous Chapter which have been used to search for evidence of new particles in high energy physics experiments. In this Chapter, I will introduce the Recursive Jigsaw approach which is a phenomenological extension of the Super-razor technique but applies a different methodology.

Recursive Jigsaw (RJ) is an approach to construct a set of observables for the above mentioned under-constrained systems on an event-by event

basis. An *event* here refers to the collection of measurements collected corresponding to a p-p collision including the three momenta of the reconstructed particles, potential measurements associated with their masses, missing momentum and the CM energy of the interaction. A "decay tree" is imposed on the reconstruction of the event. This decay tree is an approximation of the particular Feynman diagram of the reaction we intend to observe. This is the principle discriminating factor between the NP and the background samples which would result in an incomplete reconstruction or else demonstrate an over or under abundance bias hopefully yield a difference in shape to the signal.

Implementing decay tree topologies not only describes an event but also give us an extra set of kinematic observables such as the masses and the decay angles between the different frames of reference appearing in a decay tree. This gives us more handles for observation of NP in an under-constrained system in addition to the momentum and energy measurements of final state particles.

A typical RJ reconstruction is given as:

- For each event, impose a decay tree following the signal topology.
- Proceed down the decay tree from the first known reference frame, the lab frame, to the rest frame/CM frame **PP** and through each intermediate frame and determine the boosts and angles relating them to each other.
- When unknowns are encountered in calculation of the observables, a *jigsaw rule* is applied to resolve the necessary information. These set

of interchangeable rules can be applied recursively at every stage as long as they are not so over-constrained that they prevent real solutions.

- In each of these newly constructed rest frames, all relevant momenta are defined and can be used to construct a basis of kinematic variables such-as multi-object invariant masses. In order to keep these variables uncorrelated, in RJ reconstruction we exploit the boosts relating the frames since the kinematic variables correspond to the frame they are defined in.

9.1 Kinematic and Combinatoric ambiguities in an invisible particle decay

Kinematic ambiguities refer to having no information on how to sum up the invisible particles to the missing transverse energy as there are restrictions to calculating the four-momenta. Combinatoric ambiguities arise when the invisible particles are indistinguishable and we do not know where in the decay chain they should be placed. We have discussed in the previous chapter that combinatoric ambiguities are generally resolved by choosing a particular quantity to minimize, taking all possible combinations into consideration. Recursive Jigsaw uses the same principle with *jigsaw rules* designed which can be combined recursively to treat both types of ambiguities.

In a final state with no charged leptons the objects observed in the detector are predominantly jets. We partition these jets as shown in Fig. 9.1 in a hemisphere to minimize the masses of the group constituents. Hence the

choice for which vectors are summed is made by finding the jets nearest in the phase space. This tends to join a hard jet with a soft near-by radiated jet. The given number of visible momenta in the frame will be summed together until only n distinct vectors remain. The same is done for the invisible system until m vectors remain.

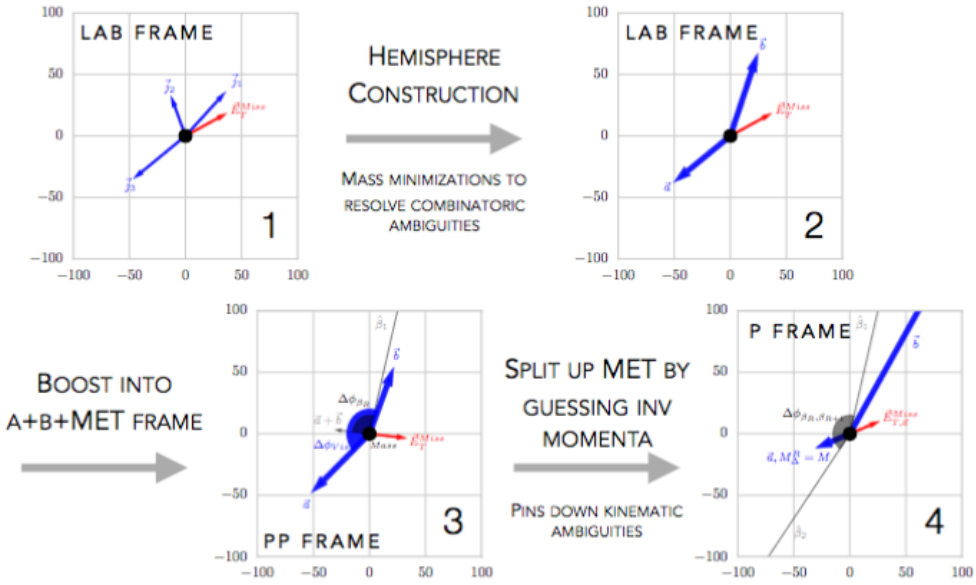

Figure 9.1: Hemisphere construction in RJ algorithm.

Using the *jigsaw rule* chosen here to minimize the masses of the reconstructed hemispheres resolved the ambiguities associated with this channel.

9.2 Jigsaw Rules

The RJ reconstruction is a framework for applying *jigsaw rules* like puzzle pieces on a chosen decay tree. Each *jigsaw rule* resolves ambiguities under

different constraints and assumptions, some of the general ones are stated below:

1. Mass resolution of Invisible particles: If the mass of an invisible particle, **I** is unknown it can be chosen to be the smallest Lorentz invariant function of visible four-vectors, that is sufficiently large to accommodate any other applied *jigsaw rules* which correspond to dividing **I** into other invisible particles for the case under study.

2. To remove dependency on the unknown degrees of freedom along the z axis: If the momentum of an invisible particle **I** is unknown in a reference frame **F** along an axis $\hat{n}_{||}$, it can be chosen so that the rapidity of invisible particle **I** is equal to the rapidity of the visible particle **V**.

$$p^F_{I,||} = p^F_{V,||} \frac{\sqrt{|p^F_{I,\perp}|^2 + m_I^2}}{\sqrt{|p^F_{V,\perp}|^2 + m_V^2}} \tag{9.1}$$

   where $\perp$ indicates plane perpendicular to $\hat{n}_{||}$. This choice is equivalent to minimizing M_{VI} w.r.t $p^F_{I,||}$.

   This is used to resolve the longitudinal boost of the lab frame to the rest frame $\beta^{\rm lab}_{\rm CM,z}$. Equating the $\beta^{\rm lab}_{\rm CM,z} = p^{\rm lab}_{v,z}/E^{\rm lab}_{\rm vis} = 0$ makes the $\beta^{\rm lab}_{\rm CM,z}$ invariant along the z direction. This also sets the $p^{lab}_{vis,z} = p^{lab}_{inv,z} = 0$ and equates the rapidity of the visible particle to the invisible particle.

3. Hemisphere minimization for two body invisible decay: If the internal degrees of freedom specifying how an invisible particle, $\mathbf{I} = I_a, I_b$ should be partitioned into two particles, they can be specified by choosing a

corresponding set of visible particles $\mathbf{V} = V_a, V_b$ and apply the constraint that the $M_{V_a I_a} = M_{V_b I_b}$. It is assumed that the four-vectors of the visible particles are known in the CM frame $\mathbf{F} = \mathbf{V}, \mathbf{I}$. If the visible particles V_a and V_b are massless, the minimum value of M_I required to guarantee that the individual invisible particles will not be tachyonic is m_V [88].

9.3 Inclusive Squark search $\tilde{q} \to q\tilde{\chi}_1^0$

For a squark pair production, as shown in the Fig. 9.2 we have two invisible particles in the final states. The decay tree imposed on this final is shown in the Fig. 9.3. The two visible particles or jets in this case have their four-momenta vectors measured in the detector. The E_T^{miss} of the system is interpreted as the sum transverse momentum of the two neutralinos:

$$E_T^{\text{miss}} = p_{I,T}^{\text{lab}} = p_{\tilde{\chi}_{1,a}^0,T}^{\text{lab}} + p_{\tilde{\chi}_{1,b}^0,T}^{\text{lab}} \tag{9.2}$$

where $\mathbf{I} = \tilde{\chi}_{1,a}^0,\ \tilde{\chi}_{1,b}^0$ sum of the two invisible particles.

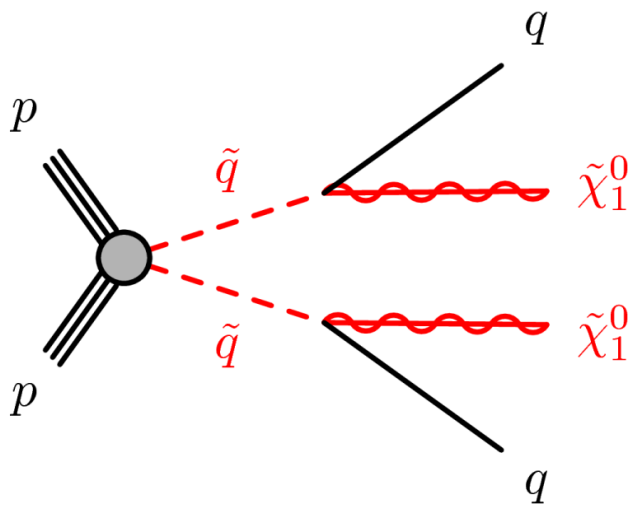

Figure 9.2: The decay topology for a squark pair production in the simplified model.

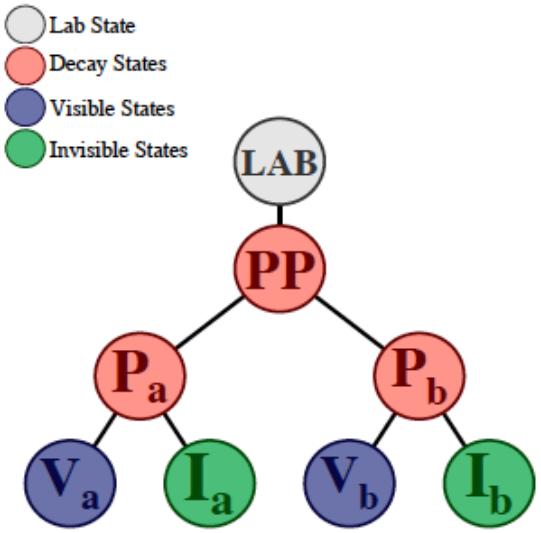

Figure 9.3: Decay tree topology for production with pair produced particles (P_a or P_b) decaying to one or more visible particles V_a and V_b and invisible particles I_a and I_b. The two sides are labelled differently to distinguish which decay particle is coming from which side of the decay tree.

With two invisible particles we have eight unknown degrees of freedom. The first "jigsaw rule" we apply here is that the rapidity of the visible system $\mathbf{V} = q_a, q_b$ is equal to the rapidity of the invisible system and the whole decay tree is essentially invariant under the longitudinal boost of the lab frame $\beta_{I,z}^{lab}$. This leaves us with mass of the neutralino system and how the transverse momentum is shared between the two invisible system to specify. To find a workaround this, we proceed to the rest frame/CM frame **PP**. In the **PP** frame shown in the Fig. 9.3 the momentum of the invisible system **I** is equal and opposite to the momentum of the visible system **V**. The momentum of the parent particles **P** are also equal and opposite in this frame. Using

only these constraints, there are many different ways to choose the unknown individual momenta of the two neutralinos. The RJ approach of reasoning is to consider these unknowns as the components of the velocities relating the two **P** rest frames to the **PP** (CM) frame [88]. Using the before-mentioned third "jigsaw rule"that the two pair produced squarks have the same mass $M_{V_a I_a} = M_{V_b I_b}$, their rest frame **P** velocities are given by:

$$\overrightarrow{\beta}_c = \overrightarrow{\beta}^{PP}_{Pa} = -\overrightarrow{\beta}^{PP}_{Pb} \tag{9.3}$$

The Euclidean mass M_c evaluated by taking the inner product of the four-vectors with a Euclidean metric is given as:

$$M_c^2 = 2(E^{\tilde{q}\tilde{q}}_{q_a} E^{\tilde{q}\tilde{q}}_{q_b} + \overrightarrow{p}^{\tilde{q}\tilde{q}}_{q_a} . \overrightarrow{p}^{\tilde{q}\tilde{q}}_{q_b}) \tag{9.4}$$

This is evaluated by taking the inner product of the four-vectors with a Euclidean metric and is invariant under the application of any contra-boost β_c.

The energy of each visible particle (jets) can be then be expressed in contra-variant terms in their respective squark production frame:

$$E^{\tilde{q}_i}_{q_i} = \frac{m^2_{q_i} + 1/2 M_c^2(p^{\tilde{q}\tilde{q}}_{q_a}, p^{\tilde{q}\tilde{q}}_{q_a})}{m^2_{q_a} + m^2_{q_b} + M_c^2(p_{q^{\tilde{q}\tilde{q}}_a}, p_{q^{\tilde{q}\tilde{q}}_a})} \tag{9.5}$$

Neglecting the individual jet masses, approximating the values of rest of the parameters to equal to one and setting the neutralinos masses to zero implies that $M_I = m_v$ where M_I is the approximated mass of neutralinos in the **PP** rest frame and m_v is the four-vectors of visible particles in the lab frame.

After the application of these "jigsaw rules", values for all of the unknowns in the event are specified. Kinematic quantities of interest are estimated by constructing a set of observables. The primary energy-scale-sensitive variables constructed for the squark analysis are denoted by H. The H variables are labeled with a superscript F and two subscripts n and m, $H^F_{n,m}$. The F represents the rest frame in which the momenta are evaluated and the subscripts n and m represent the number of visible and invisible momentum vectors considered, respectively. This means, given the number of visible momentum vectors in the frame, these are summed until only n remain.

These observables derive their name from H_T but are not necessarily evaluated in the lab frame, include contributions from the invisible momenta and need not be transverse. These are constructed with aggrgate momenta from the vectors mentioned above using the same mass minimization procedure used for the self-assembly of the decay tree. The purposeful obfuscation of information into aggregate momenta allows for the same event to be interpreted in several independent ways. Fundamentally, the efficacy of this approach comes simply from the triangle inequality $\sum |\overrightarrow{p}| \geq |\sum \overrightarrow{p}|$ such that each H variable encodes unique information.

The observables used in the squark search are:

- ${H_{1,1}}^{PP}$: scale variable as described above. Measures the momentum of missing particles in the PP frame and behaves similarly to E_T^{miss}.

- ${H_{\text{T}}}^{PP}_{2,1}$: scale variable as described above. Behaves similarly to effective mass, M_{eff} (defined as the scalar sum of the transverse momenta of the two leading jets and E_T^{miss}) for squark pair production signals with two-jet final states.

- $H_{1,1}^{PP}/H_{2,1}^{PP}$: provides additional information in testing the balance of the two scale variables, where in the denominator the $H_{2,1}^{PP}$ is no longer solely transverse. This provides excellent discrimination against unbalanced events where the large scale is dominated by a particular object p_T or by high E_T^{miss}.

- $p_{PP,\ z}^{\text{lab}}/(p_{PP,\ z}^{\text{lab}} + H_{\text{T}\ 2,1}^{PP})$: compares the z-momentum of all the objects associated with the PP system in the lab frame ($p_{PP,\ z}^{\text{lab}}$) to the overall transverse scale variable considered. This variable tests for significant boost in the z direction.

- $p_{\text{T j2}}^{PP}/H_{\text{T}\ 2,1}^{PP}$: the ratio of the transverse momenta of the second leading jet, evaluated in the PP frame ($p_{\text{T j2}}^{PP}$) to the transverse scale variable, with small values generally more background-like.

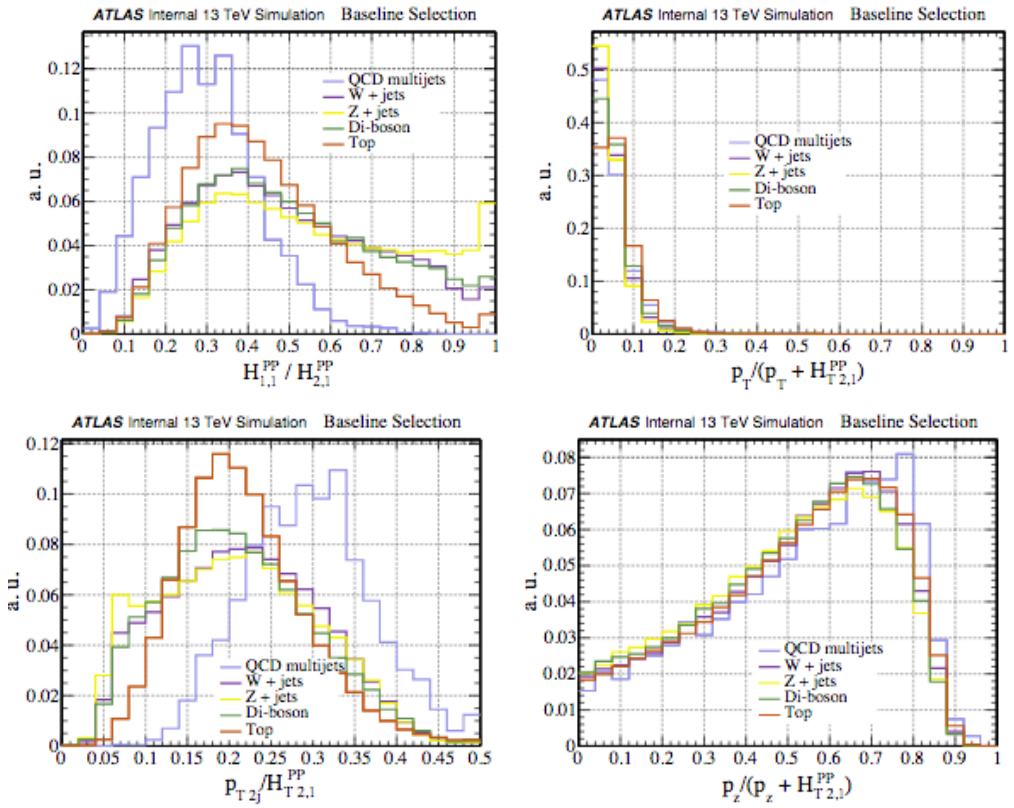

Figure 9.4: Distribution of ratios of scale variables used in the di-squark search. As can be seen, both a lower and upper cut in the $H_{1,1}^{PP}/H_{2,1}^{PP}$ is needed to remove the QCD and Top backgrounds. This would also reduce the Boson backgrounds, in the lower cut case and a particular class of Z+jets in the upper cut case [89].

Figure 9.4 shows the distributions of $H_{1,1}^{PP}/H_{2,1}^{PP}$ and illustrates why these variables are chosen for the squark signal identification.

9.4 Strong gluino production $\tilde{g}\tilde{g} \to qqqq\tilde{\chi}_1^0\tilde{\chi}_1^0$

With gluino decays we get higher jet multiplicities in the final state as shown in Fig. 9.5 and Fig. 9.6. Although a combinatoric ambiguity must be resolved as to which squark to associate with each jet, more visible particles allow for better resolution of the under-constrained neutralino kinematics. To resolve this combinatoric ambiguity we use the *jigsaw rule* to choose a $\tilde{q} - jet$ pairing that minimizes the function $M_{V_a}^2 + M_{V_b}^2$, this is equivalent to pairing particles that are travelling close together as to be expected for a common decay source.

The next *jigsaw rule* to be applied is to resolve the invisible particle masses as done in the previous section as the smallest Lorentz invariant function of visible four-vectors. This turns out to be $M_I^2 = m_V^2 - 4m_{V_aV_b}$. The second *jigsaw rule* relevant to the rapidities of visible and invisible particles to remove the $p_{I,z}^{\text{lab}}$ dependence is also applicable here. Lastly, the contra-boost invariance technique explained in the previous section is used to specify the neutralino's four-vectors using the constraint that $M_{\tilde{g}_a} = M_{\tilde{g}_b}$ is used. These rules remove the ambiguities and unknown degrees of freedom associated with the E_T^{miss} and we can now define a set of observables to study the quantities of interest like the invariant gluino masses.

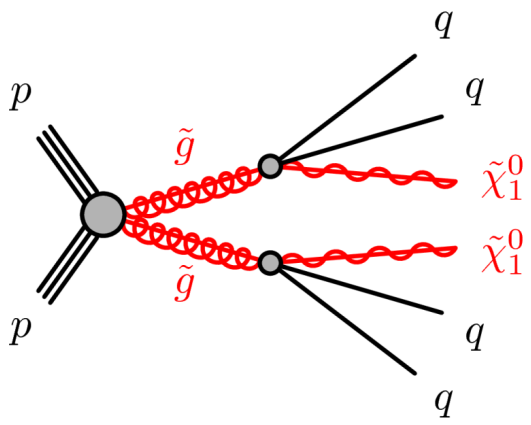

Figure 9.5: The decay topology of a gluino pair production in a direct decay. Four visible particles are reconstructed in the final state, along with two invisible particles which are constrained by the measured E_T^{miss}.

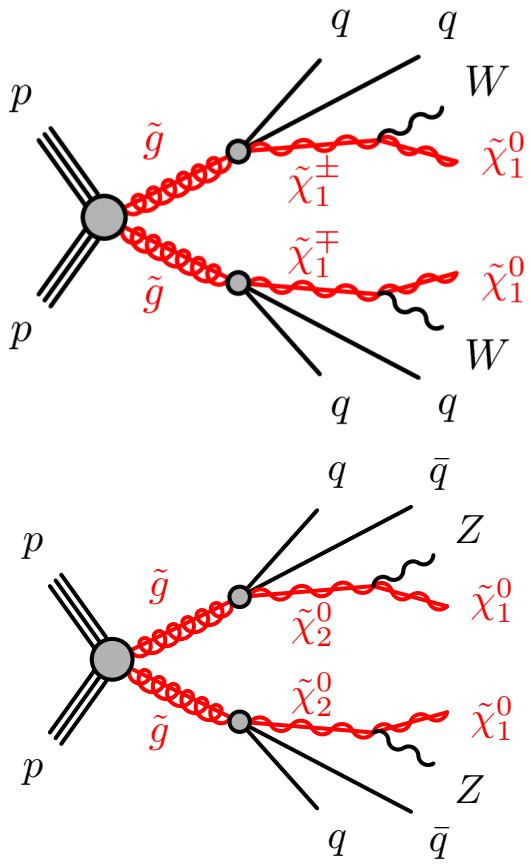

(a)

Figure 9.6: The decay topology for gluino pair production in a one-step decay.

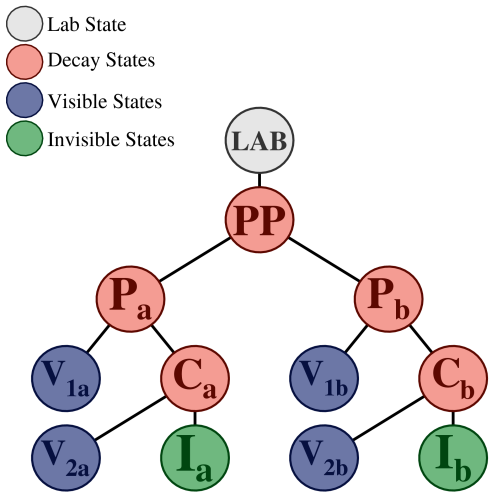

Figure 9.7: The decay tree for gluino pair production with an additional level of decay to include more than two visible particles.

For gluino pair-production the the variables used in this search are:

- $H_{1,1}^{PP}$: The same as described in Section 9.3.
- $H_{\mathrm{T}\ 4,1}^{PP}$: analogous to the transverse scale variable described in Section 9.3 but more appropriate for four-jet final states expected from gluino pair production.
- $H_{1,1}^{PP}/H_{4,1}^{PP}$: analogous to $H_{1,1}^{PP}/H_{2,1}^{PP}$ for the squark search.
- $H_{\mathrm{T}\ 4,1}^{PP}/H_{4,1}^{PP}$: a measure of the fraction of the momentum that lies in the transverse plane.
- $p_{PP,\ z}^{\mathrm{lab}}/(p_{PP,\ z}^{\mathrm{lab}} + H_{\mathrm{T}\ 4,1}^{PP})$: analogous to $p_{PP,\ z}^{\mathrm{lab}}/(p_{PP,\ z}^{\mathrm{lab}} + H_{\mathrm{T}\ 2,1}^{PP})$ above.
- $\min_i\ (p_{\mathrm{T}\ \mathrm{j}2i}^{PP}/H_{\mathrm{T}\ 2,1i}^{PP})$: represents the fraction of a hemisphere's overall scale due to the second-highest-p_T jet (in the PP frame) compared to

the overall scale, independently for each hemisphere. The smaller of the values in the two hemispheres is used, corresponding to the index i.

- $\max_i$ $(H_{1,0}^{P_i}/H_{2,0}^{P_i})$: testing balance of solely the jets momentum in a given hemisphere's approximate sparticle rest frame (P_i, index i indicating each hemisphere) provides additional discrimination against a small but otherwise signal-like subset of background events with a vector boson and associated jets.

Figure 9.8 shows some of the distributions of designed variables to explain the importance of choosing these variables as our signal discriminating selection criteria.

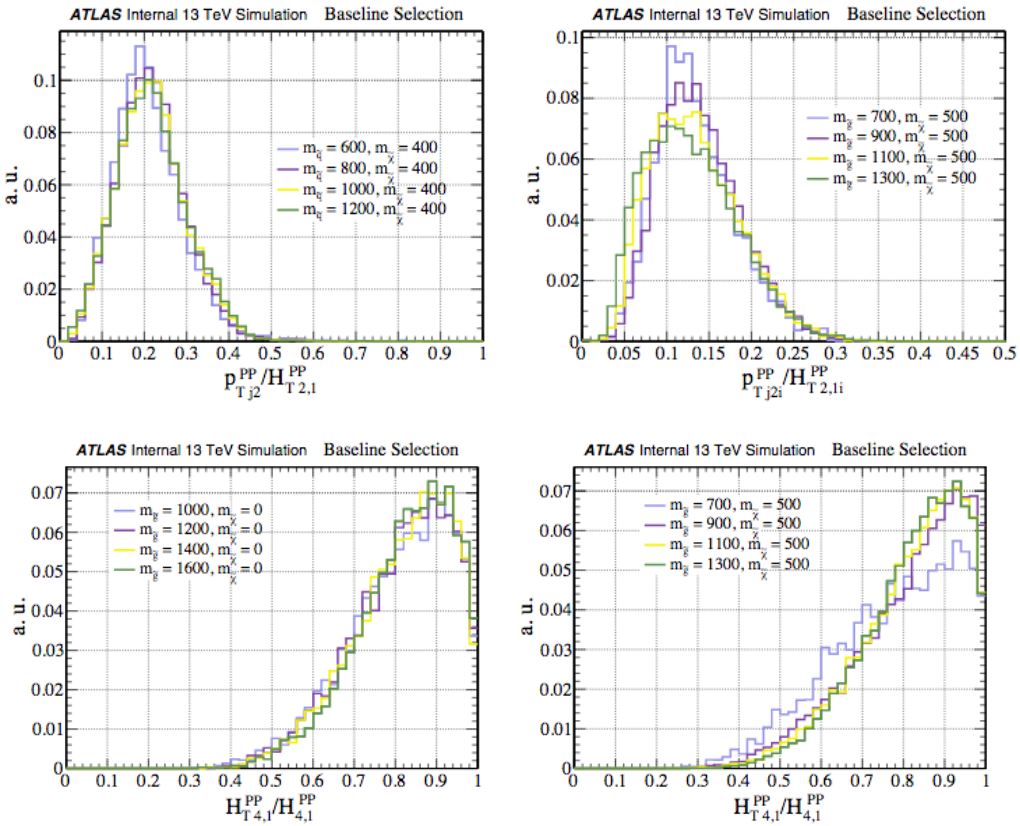

Figure 9.8: The distributions $p_{T\,j2i}^{PP}/H_{T\,2,1i}^{PP}$ (top) $H_{T\,4,1}^{PP}/H_{4,1}^{PP}$ (bottom) for di-gluino production [89].

9.5 Compressed Spectrum searches

In this search we consider cases where the initial sparticles are pair produced and decay to SM reconstructible particles and one, or more, weakly-interacting ones. The masses of the parent particles are identical as well as the masses of the invisible particles $\tilde{\chi}_1^0$. The mass splitting $m_{\tilde{P}} - m_{\tilde{\chi}_1^0}$ however

is very small in this case and the decay products do not come out with a large enough transverse momenta. Here we make use of the strong initial state radiations (ISR) jets which causes the system of initially produced sparticles to recoil in the opposite direction. By the imposition of a simple decay tree as shown in Fig. 9.9 we attempt to identify visible (V) and invisible (I) systems that are the result of an intermediate state corresponding to the system of sparticles and their decay products (S). Reconstructed E_T^{miss} from the detector is used to identify ISR. In the limit where the invisible system receives no momenta from the parent particle decay, E_T^{miss} solely results from the recoil against the ISR:

$$E_T^{\text{miss}} \approx -p_T^{\text{ISR}} \times \frac{m_{\tilde{\chi}_1^0}}{m_{\tilde{P}}} \tag{9.6}$$

where p_T^{ISR} is the total transverse momentum of the ISR system.

Since E_T^{miss} is the main discriminant in this analysis, transverse view of the reconstructed event is used which ignores the longitudinal momentum of the jets. So the all the frames seen in Fig. 9.9 are transverse approximations.

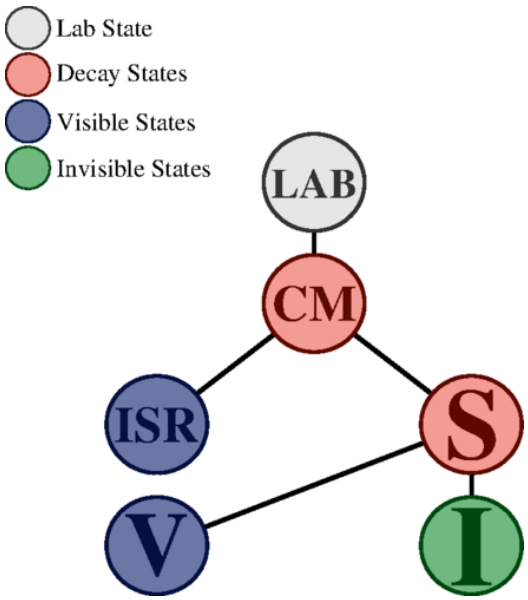

Figure 9.9: Strong sparticle production with ISR decay tree for use with small mass-splitting spectra. A signal S particle decaying to a set of visible momenta **V** and invisible momenta **I** recoils off a jet radiation system **ISR**.

The *jigsaw rule* applied here is that the objects that are close in space-time are grouped together to effectively minimize the S and ISR systems and remove combinatoric ambiguities. The total (transverse) mass of the CM frame is then given as:

$$M_{\rm CM} = \sqrt{M_{\rm ISR}^2 + (p_{\rm ISR}^{\rm CM})^2} + \sqrt{M_S^2 + (p_S^{\rm CM})^2} \tag{9.7}$$

with $p_{\rm ISR}^{\rm CM}$ and $p_S^{\rm CM}$ are the magnitudes of **ISR** and **S** systems in the CM frame respectively. They are dependant on the combination of the objects assignments and are equal in magnitude due to the minimization done above. As we can see, $M_{\rm CM}$ is independent of this assignment. Over each poten-

tial partitioning of **V** and **ISR** system, the $p_{\mathrm{ISR/S}}^{\mathrm{CM}}$ is effectively maximized simultaneously as the minimization on the M_S and the M_{ISR}. This is similar to reconstructing E_T^{miss} and performing a jet-clustering around it using the transverse mass as a distance metric [91].

We can then construct a set of experimental observables that are sensitive to the mass-splitting between parent and child sparticles and that are capable of discriminating against SM background.

- $p_{\mathrm{T}\ S}^{\mathrm{CM}}$: the magnitude of the vector-summed transverse momenta of all S-associated jets ($|\vec{p}_{\mathrm{T}\ S}^{\mathrm{CM}}|$) and E_T^{miss} evaluated in the CM frame.

- $R_{\mathrm{ISR}} \equiv \vec{p}_I^{\mathrm{CM}} \cdot \hat{p}_{\mathrm{T}\ S}^{\mathrm{CM}} / p_{\mathrm{T}\ S}^{\mathrm{CM}}$: serves as an estimate of $m_{\tilde{\chi}}/m_{\tilde{g}/\tilde{q}}$. This is the fraction of the momentum of the S system that is carried by its invisible system I, with momentum $\vec{p}_I^{\mathrm{CM}}$ in the CM frame. As $p_{\mathrm{T}\ S}^{\mathrm{CM}}$ grows it becomes increasingly hard for backgrounds to possess a large value in this ratio – a feature exhibited by compressed signals.

- $M_{\mathrm{T}\ S}$: the transverse mass of the S system.

- N_{jet}^V: number of jets assigned to the visible system (V) and not associated with the ISR system.

- $\Delta\phi_{\mathrm{ISR},\ I}$: the azimuthal opening angle between the ISR system and the invisible system in the CM frame.

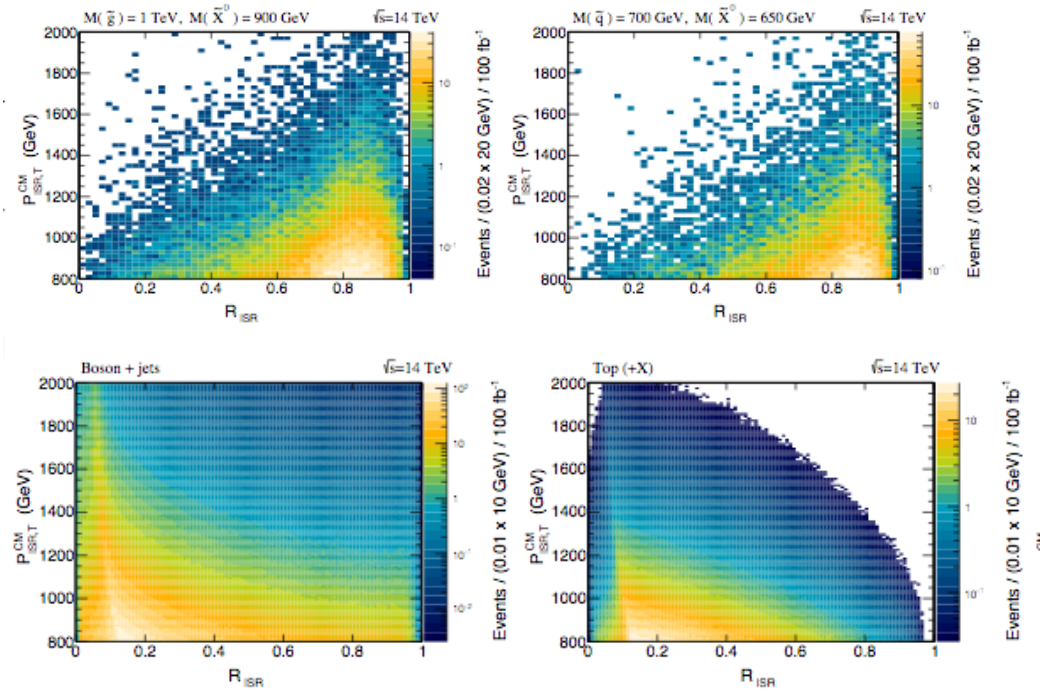

Figure 9.10: (down row) Distribution of $p^{\mathrm{CM}}_{\mathrm{ISR,T}}$ as a function of R_{ISR} from (left to right) boson+jets and top+X backgrounds. (up row) Distribution of $p^{CM}_{\mathrm{ISR,T}}$ as a function of R_{ISR} from (left to right) gluino and squark pair-production signal samples [91].

Figure 9.10 shows different behaviour of squark and gluino signals as compared to the boson+jets and top+X backgrounds. Increasing $p^{\mathrm{CM}}_{\mathrm{ISR,T}}$ results in a narrowing of R_{ISR} for compressed signals and for backgrounds the two variables are highly uncorrelated. Hence stricter cuts on $p^{\mathrm{CM}}_{\mathrm{ISR,T}}$ yield better discrimination from R_{ISR}.

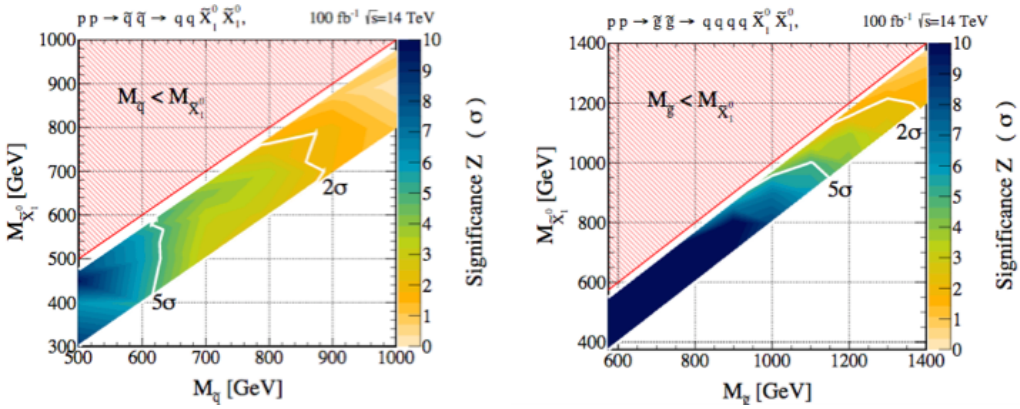

Figure 9.11: Projected exclusion and discovery reach for squarks (right-hand) and gluino pair production (left-hand) in the compressed regions with 25 GeV $\geq \Delta m \leq$ 200 GeV [91].

Figure 9.11 illustrates the projected sensitivities for putative gluino and squark signals with compressed mass spectra with an integrated luminosity of 100 fb^{-1} at centre-of-mass energy of $\sqrt{s}$ = 14 TeV. These sensitivities were calculated using optimizing cuts on the variables mentioned before. This plot shows that gluino masses in compressed scenarios above 1 TeV can be discovered with exclusion significance for masses of 1.4 TeV in some cases. Also squark masses of 600 GeV and mass splitting up to 200 GeV can be discovered with greater than 5σ significance while they can be excluded for masses between $\approx$ 800 and 900 GeV.

9.6 QCD rejection variables

In order to reject fake E_T^{miss} coming from jet mismeasurements, the E_T^{miss} is combined with jets using a jet-clustering algorithm where a recursive min-

imization is done on the reconstructed four-vectors of jets and E_T^{miss} (on event-by-event basis) assembled in a binary decay tree as shown in Fig. 9.12.

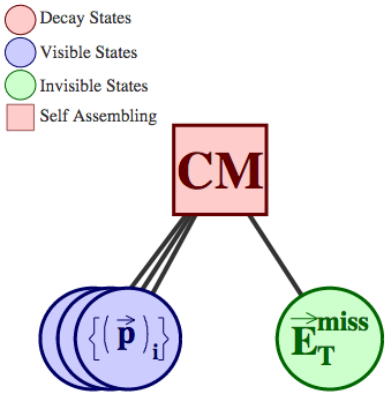

Figure 9.12: Diagram of decay tree containing a *self assembling* frame. This frame will take all of its children (including the individual elements comprising p_i) and arrange them in a binary decay tree by recursively minimizing the masses of the two children at each step. The *self assembling* frame selects which elements of the p_i is the E_T^{miss} closest to momentum space and whose potential mis-measurements are most-likely to have caused the E_T^{miss}.

The jets appearing with the E_T^{miss} have their transverse momenta compared with the E_T^{miss} using the observable:

$$R_{\text{QCD}} = \frac{\max(\vec{p}_{\text{T}}^{\,\text{jets}} \cdot \vec{E}_{\text{T}}^{\,\text{miss}}, 0)}{(E_T^{\text{miss}})^2 + \max(\vec{p}_{\text{T}}^{\,\text{jets}} \cdot \vec{E}_{\text{T}}^{\,\text{miss}}, 0)}, \tag{9.8}$$

where $\vec{p}_{\text{T}}^{\,\text{jets}}$ is the transverse momentum of the E_T^{miss}-associated jets in the lab-frame. An angular discriminant called "Δ_{QCD}" is defined for the same purpose. It uses the $\cos(\phi_{\text{j}}, E_T^{\text{miss}})$, the decay angle of the jets/E_T^{miss} system calculated using the transverse jet(s) and E_T^{miss} four-vectors.

$$\Delta_{\mathrm{QCD}} = \frac{1 + \cos(\phi_{\mathrm{j},\ E_T^{\mathrm{miss}}}) - 2R_{\mathrm{QCD}}}{1 + \cos(\phi_{\mathrm{j},\ E_T^{\mathrm{miss}}}) + 2R_{\mathrm{QCD}}}. \tag{9.9}$$

This variable tends to have values in the interval $[-1, 0]$ for severe jet-mismeaurements while E_T^{miss} coming from weakly interacting particle tends to have a value in $[0, 1]$ as shown in Fig. 9.13.

QCD rejection can also be done by using the variables from RJ reconstructed variables. When the E_T^{miss} has a suspicious provenance, an additional imbalance is introduced between E_T^{miss} and the visible objects, this appears in the calculation of $p_{T,PP}^{\mathrm{lab}} = E_T^{\mathrm{miss}} + p_{V,T}^{\mathrm{lab}}$. This momentum is used to calculate the boost from the lab frame to the PP rest frame. If we mis-measure E_T^{miss} and over-boost then the sum of the visible momenta in the resulting frame, $\overrightarrow{p}_V^{PP}$ will tend to the direction opposite the boost whereas there would be no correlation if the boost was correct. Similarly, if there were an under-boost $\overrightarrow{p}_V^{PP}$ will align to the boost. These two extrema correspond directly to π and 0 in the variable $\Delta\phi_R$ which is designed to look for this effect. Fig. 9.14 shows this alignment more so with increasing $R_{p_T^{CM},\sqrt{S_R}}$. QCD events can be rejected be applying cuts on $R_{p_T^{\mathrm{CM}},\sqrt{S_R}}$, $\Delta\phi_R$.

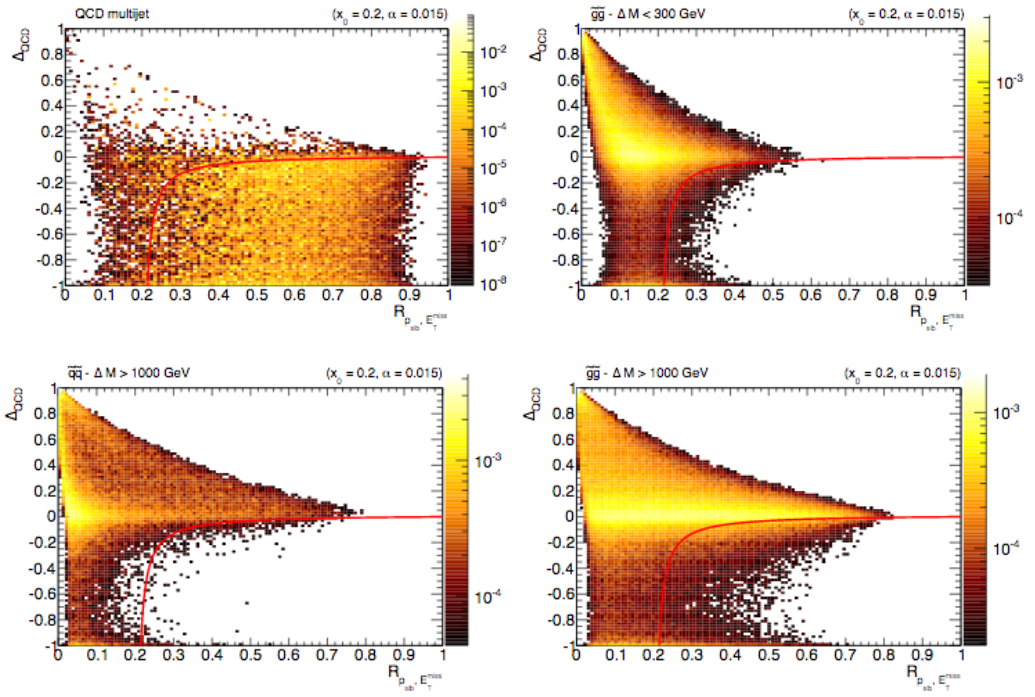

Figure 9.13: QCD rejection using the variables $\Delta_{\text{QCD}}, R_{\text{QCD}}$ for simulated background and signal models. The upper left plot shows the distribution for QCD multi-jet events, while the upper right plot contains the distribution for an ensemble of simulated di-gluino models. The latter is restricted to signal models where the mass difference between the gluino and LSP is less than 300 GeV. The bottom row of plots contain simulated signals where the mass different between the parent sparticle and LSP is greater than 1 TeV, with di-squarks (left) and di-gluinos (right). The red curve indicates a potential cut, with the R_{QCD} term offset for the cut ($x_0 = 0.2$) and the amount of bend ($\alpha = 0.015$) indicated in the upper right of the plots. These parameters correspond to a default working point that is relatively performant for all of the signals considered but not optimal for any.

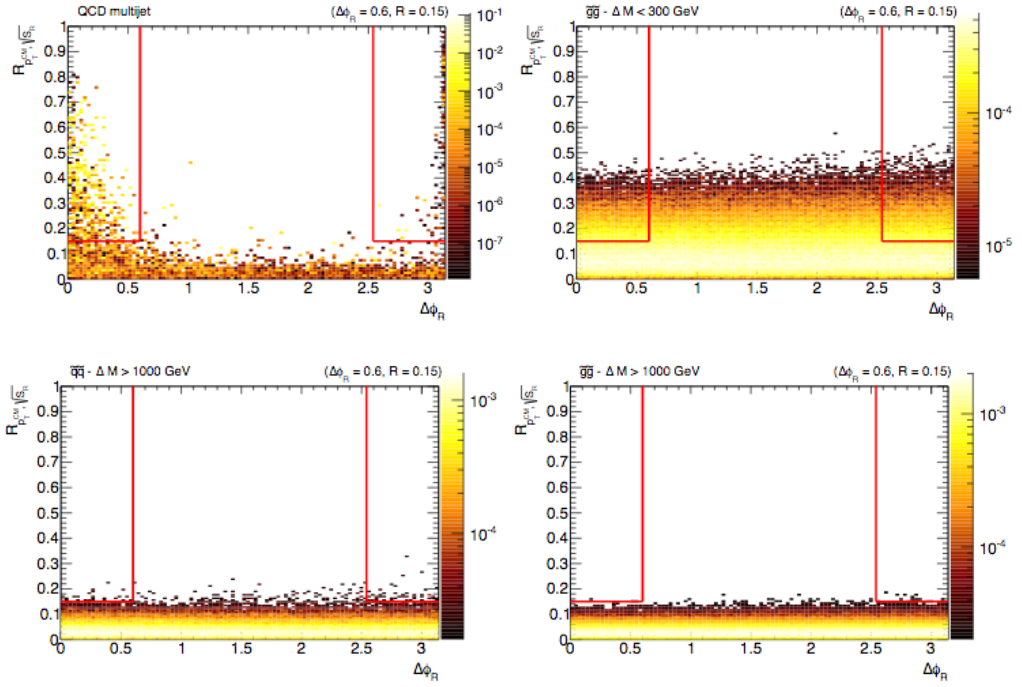

Figure 9.14: Two-dimensional distributions QCD rejection variables $R_{p_T^{\mathrm{CM}},\sqrt{S_R}}$, $\Delta\phi_R$ for simulated signal and background samples. The upper left plot shows the distribution for QCD multi-jet events, while the upper right plot contains the distribution for an ensemble of simulated di-gluino models. The latter is restricted to signal models where the mass difference between the gluino and LSP is less than 300 GeV. The bottom row of plots contain simulated signals where the mass different between the parent sparticle and LSP is greater than 1 TeV, with di-squarks (left) and di-gluinos (right). The red lined boxes indicate a potential cut, with the width of the cut ($\Delta\phi_R = 0.6$) and the height of the cut ($R_{p_T^{CM},\sqrt{S_R}} = 0.15$) indicated in the upper right of the plots. These parameters correspond to a default working point that is relatively performant for more compressed scenarios but not optimal for large mass splittings.

9.7 Simplified Models

The philosophy behind Simplified Models is simple; write an effective Lagrangian that requires minimum field content to produce a specific SUSY signature. This Lagrangian introduces the smallest possible set of new particles and their couplings by keeping the number of free parameters to $\mathcal{O}$(a few). It is possible then to provides the maximal reach in both mass and $\sigma \times BR$ [92]. A significant criticism of Simplified Models is that they each assume a 100% branching ratio to a specific signature. If an excess is seen in one channel then these models would try to explain it through one specific signature. We could then apply the cumulative results of all possible decay chains to see which model best fits the signal seen. But since no information is available on how the branching ratios are distributed and since each model assumes it provides the full excess of events seen, this method is too simplified to explain the nature of NP. So simplified models can tell us where to look for NP signals but they can't fully explain what it is [87].

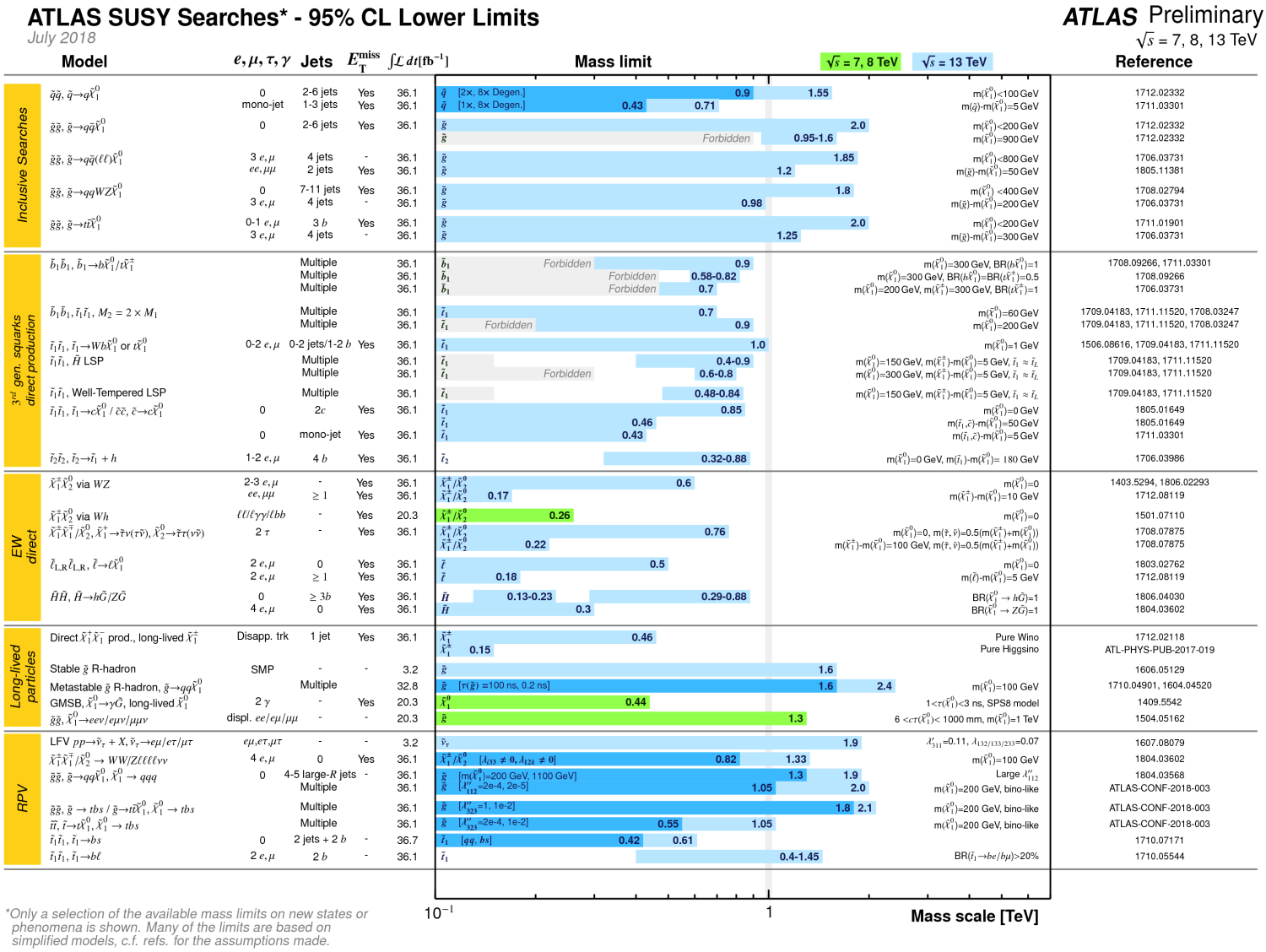

Figure 9.15: Mass reach of the ATLAS searches for SUSY. Results are quoted for the nominal cross section in both a region of near-maximal mass reach and a demonstrative alternative scenario, in order to display the range in model space of search sensitivity [90].

Part IV

Results and Conclusion

"Everything should be made as simple as possible but not simpler."

Albert Einstein

Chapter 10

Search for squarks and gluinos in the 0 Lepton Channel

The analysis described in this part of the thesis is published in Ref. [93]. Details are provided in this chapter on the design of the analysis.

10.1 Monte Carlo Samples

Simplified models and pMSSM models are both used as representative SUSY signals for this analysis. Signal samples are used to describe squark and gluino pair production, followed by the direct or one-step decays of squarks and direct or one-step decays of gluinos as shown in Figure 10.1. These samples were generated with up to two (simplified models) or one (pMSSM models) extra partons in the matrix element using the Madgraph event generator interface with PYTHIA 8.

The simulation of the W or Z/γ boson production is performed using

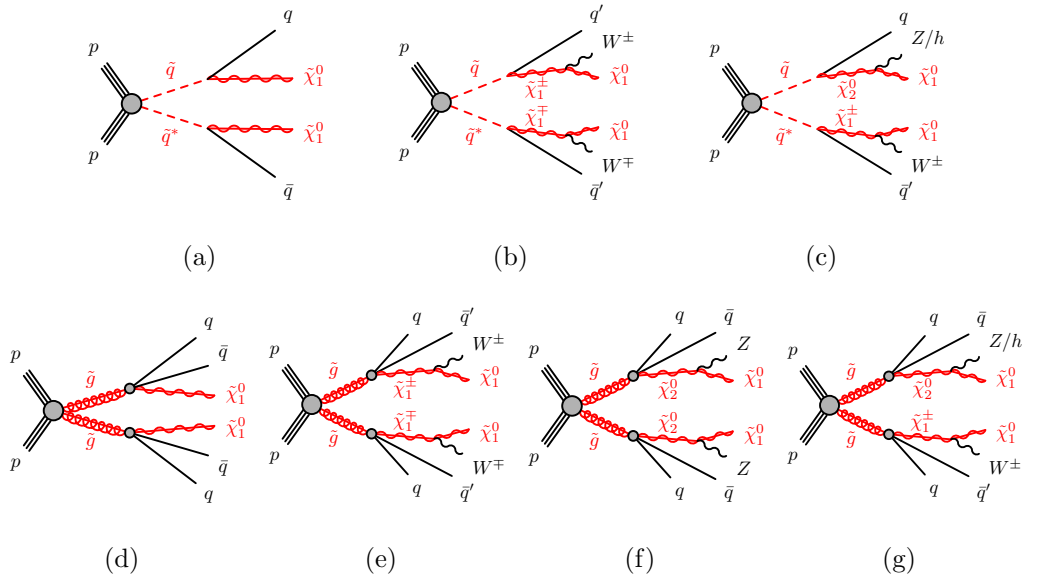

Figure 10.1: The decay topologies of squark pair production (a,b,c) and gluino pair production (d, e, f, g) in the simplified models with direct (a) or one-step (b,c) decays of squarks and direct (d) or one-step (e, f, g) decays of gluinos.

Sherpa event generator. Simulated events containing a photon in association with jets were generated requiring a photon transverse momentum above 35 GeV. For the generation of $t\bar{t}$ and single-top processes Powheg-Box v2 generator was used. Diboson processes (WW, WZ, ZZ) were simulated again using the Sherpa generator. For processes with four charged leptons (4ℓ), three charged leptons and a neutrino (3ℓ+1ν) or two charged leptons and two neutrinos (2ℓ+2ν), the matrix elements contain all diagrams with four electroweak couplings, and were calculated for up to one (4ℓ, 2ℓ+2ν) or no partons (3ℓ+1ν) at NLO. For processes in which one of the bosons decays

Table 10.1: The SUSY signals and the SM background MC simulation samples used in this analysis. The generators, the order in α_s of cross-section calculations used for yield normalization, PDF sets, parton showers and tunes used for the underlying event are shown.

Physics process	Generator	Cross-section normalization	PDF set	Parton shower	Tune
SUSY processes	MG5_aMC@NLO 2.2.2–2.3.3	NLO+NLL	NNPDF2.3LO	pythia 8.186	A14
$W \to \ell\nu$ + jets	sherpa 2.2.1	NNLO	NNPDF3.0NNLO	sherpa	sherpa default
$Z/\gamma^* \to \ell\bar{\ell}$ + jets	sherpa 2.2.1	NNLO	NNPDF3.0NNLO	sherpa	sherpa default
γ + jets	sherpa 2.1.1	LO	CT10	sherpa	sherpa default
$t\bar{t}$	Powheg-Box v2	NNLO+NNLL	CT10	pythia 6.428	Perugia2012
Single top (Wt-channel)	Powheg-Box v2	NNLO+NNLL	CT10	pythia 6.428	Perugia2012
Single top (s-channel)	Powheg-Box v2	NLO	CT10	pythia 6.428	Perugia2012
Single top (t-channel)	Powheg-Box v1	NLO	CT10f4	pythia 6.428	Perugia2012
Single top (Zt-channel)	MG5_aMC@NLO 2.2.1	LO	CTEQ6L1	pythia 6.428	Perugia2012
$t\bar{t} + W/Z/WW$	MG5_aMC@NLO 2.2.3	NLO	NNPDF2.3LO	pythia 8.186	A14
WW, WZ, ZZ	sherpa 2.1.1	NLO	CT10	sherpa	sherpa default

hadronically and the other leptonically, matrix elements were calculated for up to one (ZZ) or no (WW, WZ) additional partons at NLO. All diboson samples also simulated up to three additional partons at LO using the Comix and OpenLoops matrix-element generators, and were merged with the Sherpa parton shower.

A summary of all the MC samples used is given in Table.10.1.

10.2 Physics Object Definitions

The reconstructed primary vertex of the event is required to be consistent with the luminous region and to have at least two associated tracks with $p_T > 400$ MeV. When more than one such vertex is found, the vertex with the largest $\sum p_T^2$ is chosen. Jet candidates are reconstructed using the anti-

k_t jet clustering algorithm with a jet radius parameter of 0.4 starting from clusters of calorimeter cells. The jets are corrected for energy from pile-up using the method: a contribution equal to the product of the jet area and the median energy density of the event is subtracted from the jet energy. Further corrections, referred to as the jet energy scale corrections, are derived from MC simulation and data, and are used to calibrate the average energies of jets to the scale of their constituent particles. Only corrected jet candidates with $E_T^{\text{miss}} > 20$ GeV and $|\eta| < 2.8$ are retained.

Jet Vertex Tagger (JVT) s a jet moment which aims to distinguish between jets arising from the hard-scatter and the pile up. By cutting hard on JVT of each jet, better rejection of pile-up jets can be achieved, although this comes at a cost of a decreased acceptance for jets coming from the hard-scatter.

10.2.1 Overlap removal

Since electrons and jets are calorimetric objects it is not uncommon for an electron to also be reconstructed as a jet or vice versa. In addition, for the purpose of this analysis, electrons and muons in a jet (e.g. from hadron decays) are not relevant to classify the event. To this effect, an "overlap removal" procedure is applied to avoid double counting and/or remove non isolated leptons.

Most overlap criteria are based on the simple geometric $\Delta R = \sqrt{(\Delta\phi)^2 + (\Delta\eta)^2}$ variable. The criteria is applied in the following order:

- If a baseline electron and a baseline muon share the same ID track, the electron is ignored.

- If a baseline electron and a jet are found within $\Delta R < 0.2$, and a jet is not b-tagged with MV2c10 85% efficiency working point, the object is interpreted as an electron and the overlapping "jet" is ignored.

- If a baseline electron and a jet are found within $\Delta R < 0.4$, and the jet is not flagged as "pile-up jet" ($p_T > 60$ GeV $\parallel \eta > 2.4 \parallel$ JVT > 0.59), the the object is interpreted as a jet and the nearby "electron" is ignored.

- If a baseline muon and a jet are found within $\Delta R < 0.2$, the object is treated as a muon and the overlapping "jet" is ignored if the jet and the muon satisfy either of the following criteria:

  - The number of tracks with $p_T > 500$ MeV that are associated to the jet is less than three.

  - The jet is not b-tagged with MV2c10 85% efficiency working point.

- If a baseline muon and a jet are found within $\Delta R < \min(0.4, 0.04 + 10$ GeV$/ p_T^{muon})$, the object is treated as a jet and the overlapping "muon" is removed if the jet is not flagged as pile-up jet.

Table 10.2: Summary of the jet selection criteria

Cut	Value/Description
Baseline Jet	
Algorithm	Anti-k_T Topo R = 0.4
Acceptance	$p_T > 25$ GeV, $\eta < 2.8$
Pile-up Suppression	$p_T > 60$ GeV $\parallel$ $\eta > 2.4$ $\parallel$ JVT > 0.59
b-jet	
b-tagging algorithm	MVc210 at 77% efficiency point
Acceptance	$p_T > 60$ GeV, $\eta < 2.5$
Reclustered Jet	
Algorithm	Anti-k_T R= 1.0
Input	Baseline jets with $p_T > 25$ GeV

Table 10.3: Summary of the electron selection criteria. The signal selections are applied on top of the preselection.

Cut	Value/Description
Baseline Electron	
Algorithm	AuthorElectron
Acceptance	$p_T > 7$ GeV, $\eta^{\text{clust}} < 2.47$
Quality	LooseLH
Overlap	ΔR(e,jet) > 0.4
Signal Electron	
Acceptance	$p_T > 7$ GeV
Quality	TightLL
Isolation	GradientLoose
Track	$\lvert z_0^{PV}.sin\theta\rvert < 0.5$ mm
	$\lvert d_0^{PV}\rvert/\sigma(d_0^{PV}) < 5$

Table 10.4: Summary of the muon selection criteria. The signal selections are applied on top of the preselection.

Cut	Value/Description
Baseline muon	
Acceptance	$p_T > 7$ GeV, $\|\eta\| < 2.7$
Quality	Medium
Overlap	$\Delta R(\mu,\text{jet}) > 0.4$
Signal muon	
Acceptance	$p_T > 7$ GeV
Isolation	GradientLoose
Track	$\|z_0^{PV}.sin\theta\| < 0.5$ mm
	$\|d_0^{PV}\|/\sigma(d_0^{PV}) < 3$

Table 10.5: Summary of the photon selection criteria. The signal selections are applied on top of the preselection.

Cut	Value/Description
Baseline photon	
Acceptance	$p_T > 25$ GeV, $\|\eta\| < 2.37$
Quality	Loose
Overlap	$\Delta R(\gamma,\text{jet}) > 0.4$
Signal muon	
Quality	Tight
Isolation	FixedCutTight

The E_T^{miss} definitions are the same as given in Section 5.7.

For the analysis documented here,

- No event is selected if it contains a baseline electron or muon with $p_{\text{T}} >$ 7 GeV.

- No event is selected if it contains a jet that does not satisfy the quality

selection criteria defined in Tab 10.2.1.

- Events are rejected if no jets $p_T > 50$ GeV are found.

10.3 Signal regions optimization procedure

In order to determine suitable signal regions, a brute-force optimization of a significance metric was performed, utilizing a selection of RJ variables that were found to exhibit properties beneficial to the analysis approach, specific to each final state. For each different kinematic target (squarks-like regions, gluinos-like regions and the compressed models in each, respectively) all relevant variables are input into a global optimization, considering each combination of cuts on all the variables simultaneously. However, in order to understand the performance of each cut, this was performed in an iterative manner, studying multiple combinations of cuts and values in order to identify redundancies. This method was chosen to demonstrate to the analysts the tractability of a given cut in the presence of others that were found to be performant. Furthermore, this provides justification for each individual cut that is applied. The optimization is performed using a Z_{Bi} significance metric, with varying integrated luminosity and fixed systematic uncertainty scenarios.

10.4 Signal Regions

Various signal regions are defined in the RJR-based approach to be most sensitive to a variety of potential SUSY signals. A choice is made to limit

the number of dimensionful variables to only two when defining the signal regions targeting models with the gluino and squark pair production. The different types of signals are grouped according to sparticle mass splittings, each with dedicated optimizations. The two chosen scale variables are $H_{1,1}^{PP}$ and either $H_{T2,1}^{PP}$ (for models targeting squark pair production) or $H_{T4,1}^{PP}$ (for models targeting gluino pair production). These serve to select events with large missing momentum and a high collective scale for the reconstructed jets. In order to further suppress SM backgrounds, a variety of additional constraints on dimensionless variables are imposed.

The procedure adopted is such that, as the mass splitting between parent sparticle and the LSP increases, the criteria applied to the scale variables are tightened, while the criteria for dimensionless variables are loosened. In searching for the squark pair production, the overall balance of the events is studied with $H_{1,1}^{PP}/H_{2,1}^{PP}$. The range selected in this ratio rejects those events where the missing transverse momentum dominates the scale (upper bound) and ensures the sufficient balance between the scales of visible and invisible particles (lower bound). The selection on the $p_{\mathrm{T\,j2}}^{PP}/H_{\mathrm{T}\,2,1}^{PP}$ ratio serves to ensure that each of the jets contributes to the overall scale significantly. This particular ratio is a powerful criterion against imbalanced events with W/Z+jets, where one of the jets has a much higher momentum than the sub-leading jet.

For signals of gluino pair production, the same principles are followed. Tight requirements are placed on $H_{1,1}^{PP}/H_{4,1}^{PP}$ and $H_{\mathrm{T}\,4,1}^{PP}/H_{4,1}^{PP}$ to target scenarios with more compressed spectra. A selection is applied to the ratio $p_{PP,\,z}^{\mathrm{lab}}/\left(p_{PP,\,z}^{\mathrm{lab}} + H_{\mathrm{T}\,4,1}^{PP}\right)$ to test the size of the total z-component of mo-

mentum relative to the overall scale, requiring that it should be small. A lower bound is placed on $p_{\mathrm{T\ j2}}^{PP}/H_{\mathrm{T\ 2,1}}^{PP}$. This provides a very strong constraint against events where the two hemispheres are well balanced but one of the jets dominates the scale variable contribution. In order to reject events where the E_T^{miss} results from mismeasurements of jets, a requirement on the variable Δ_{QCD} is applied, rejecting events where this is deemed likely.

Additionally, separate SRs are defined for models with extremely compressed spectra. Following the pattern of successive SRs targeting larger mass splitting scenarios, several regions designed to be sensitive to various mass splittings utilize the ISR-boosted compressed decay tree described in the previous chapter. These regions target mass splittings between parent squarks and gluinos and $\tilde{\chi}_1^0$ from roughly 25 GeV to 200 GeV.

Each of the SR selection requirements is optimized to exploit expected differences in masses, kinematics, and jet multiplicities, and each represents its own counting experiment. Six signal regions (categorized into three groups) have been developed to have sensitivity to different regions of the squark-LSP mass plane. The increasing SRS[1-4] are designed for increasing squark-LSP mass splittings. The a/b versions of each are designed for lower and higher scales respectively where only the cuts on variables with mass-full units are changed. Seven signal regions (categorized into three groups) have been developed to have sensitivity to different regions of the gluino-LSP mass plane. As for the squark-sensitive regions, the increasing SRG[1-4] are designed for increasing gluino-LSP mass splittings. The a/b versions of each are designed for lower and higher scales respectively where only the cuts on mass-sensitive variables changed. Five signal regions have been developed to target differ-

ent mass splitting between parent sparticles (squarks and gluinos) and LSPs, ranging from a few GeV splitting to 200 GeV.

The selection criteria of the resulting 19 signal regions are summarized in Table 10.7. The entries for $|\eta_{\mathrm{j1,j2}}|$ and $|\eta_{\ \mathrm{j1,2},a,b}|$ correspond to upper bounds on the pseudorapidities of the leading two jets in each event and the leading two jets in each hemisphere a, b, respectively, while $|\eta_{\mathrm{j}V}|$ corresponds to the jets associated with the system V.

Table 10.6: Selection criteria used to define signal regions in the RJR-based squark searches.

Targeted signal	$\tilde{q}\tilde{q},\ \tilde{q} \to q\tilde{\chi}_1^0$						
Requirement	Signal Region						
	RJR-S1		**RJR-S2**		**RJR-S3**		**RJR-S4**
$H_{1,1}^{PP}/H_{2,1}^{PP} \geq$	0.55		0.5		0.45		–
$H_{1,1}^{PP}/H_{2,1}^{PP} \leq$	0.9		0.95		0.98		
$p_{\mathrm{T\,j2}}^{PP}/H_{\mathrm{T}\ 2,1}^{PP} \geq$	0.16		0.14		0.13		0.13
$\lvert\eta_{\mathrm{j1,j2}}\rvert \leq$	0.8		1.1		1.4		2.8
$\Delta_{\mathrm{QCD}} \geq$	0.1		0.05		0.025		0
$p_{PP,\ \mathrm{T}}^{\mathrm{lab}}/\left(p_{PP,\ \mathrm{T}}^{\mathrm{lab}} + H_{\mathrm{T}\ 2,1}^{PP}\right) \leq$	0.08						
	RJR-S1a	**RJR-S1b**	**RJR-S2a**	**RJR-S2b**	**RJR-S3a**	**RJR-S3b**	**RJR-S4**
$H_{\mathrm{T}\ 2,1}^{PP}$ [GeV] $>$	1000	1200	1400	1600	1800	2100	2400
$H_{1,1}^{PP}$ [GeV] $>$	800	1000	1200	1400	1700	1900	2100

Table 10.7: Selection criteria used to define signal regions in the RJR-based search. Each SR is labeled with the 'G' for the targeted gluino regions.

Targeted signal	$\tilde{g}\tilde{g}$, $\tilde{g} \to q\bar{q}\tilde{\chi}_1^0$						
Requirement	Signal Region						
	RJR-G1		**RJR-G2**		**RJR-G3**		**RJR-G4**
$H_{1,1}^{PP}/H_{4,1}^{PP} \geq$	0.45		0.3		0.2		–
$H_{\mathrm{T}\ 4,1}^{PP}/H_{4,1}^{PP} \geq$	0.7		0.7		0.65		0.65
$\min\left(p_{\mathrm{T}\ \mathrm{j}2i}^{PP}/H_{\mathrm{T}\ 2,1i}^{PP}\right) \geq$	0.12		0.1		0.08		0.07
$\max\left(H_{1,\ 0}^{P_i}/H_{2,\ 0}^{P_i}\right) \leq$	0.96		0.97		0.98		0.98
$\lvert\eta_{\mathrm{j}1,2,a,b}\rvert \leq$	1.4		2.0		2.4		2.8
$\Delta_{\mathrm{QCD}} \geq$	0.05		0.025		0		0
$p_{PP,\ z}^{\mathrm{lab}}/\left(p_{PP,\ z}^{\mathrm{lab}} + H_{\mathrm{T}\ 4,1}^{PP}\right) \leq$	0.5		0. 55		0.6		0.65
$p_{PP,\ \mathrm{T}}^{\mathrm{lab}}/\left(p_{PP,\ \mathrm{T}}^{\mathrm{lab}} + H_{\mathrm{T}\ 4,1}^{PP}\right) \leq$	0.08						
	RJR-G1a	**RJR-G1b**	**RJR-G2a**	**RJR-G2b**	**RJR-G3a**	**RJR-G3b**	**RJR-G4**
$H_{\mathrm{T}\ 4,1}^{PP}$ [GeV] $>$	1200	1400	1600	2000	2400	2800	3000
$H_{1,1}^{PP}$ [GeV] $>$	700		800		900		1000

Table 10.8: Selection criteria defined for signal regions in compressed spectrum covered by the analysis, denoted by 'C'.

Targeted signal	compressed spectra in $\tilde{q}\tilde{q}$ ($\tilde{q} \to q\tilde{\chi}_1^0$); $\tilde{g}\tilde{g}$ ($\tilde{g} \to q\bar{q}\tilde{\chi}_1^0$)				
Requirement	Signal Region				
	RJR-C1	**RJR-C2**	**RJR-C3**	**RJR-C4**	**RJR-C5**
$R_{\mathrm{ISR}} \geq$	0.95	0.9	0.8	0.7	0.7
$p_{\mathrm{T}\ S}^{\mathrm{CM}}$ [GeV] $\geq$	1000	1000	800	700	700
$\Delta\phi_{\mathrm{ISR},\ I}/\pi \geq$	0.95	0.97	0.98	0.95	0.95
$\Delta\phi(\mathrm{jet}_{1,2}, E_T^{\mathrm{miss}})_{\mathrm{min}} \geq$	–	–	–	0.4	0.4
$M_{\mathrm{T}\ S}$ [GeV] $\geq$	–	100	200	450	450
$N_{\mathrm{jet}}^V \geq$	1	1	2	2	3
$\lvert\eta_{jV}\rvert \leq$	2.8	1.2	1.4	1.4	1.4

10.5 The M_{eff}-based approach

Another approach called the M_{eff} based analysis is also done complementary to the Recursive Jigsaw technique. This method uses M_{eff}, E_T^{miss}, psuedorapidities and event shape variables like aplanarity as it's discrimination criteria. The two analysis cover the same final states containing only hadronic jets and large missing momenta. These two approaches are complementary because of differences in selected event populations and the strategy for balancing the signal-to-background ratio against systematic uncertainties. Signal selection here uses requirements on the M_{eff} variable which is defined for this analysis as the sum over all jets with $p_{\mathrm{T}} > 50$ GeV and $E_{\mathrm{T}}^{\mathrm{miss}}$ to suppress

SM backgrounds, which tend to have low jet multiplicity.

Although the two analysis use different kinematic variables, there are a fraction of events that are common to regions defined in the analyses for both the SM backgrounds and the SUSY signals. For models with large $\tilde{q}/\tilde{g}$ masses, the stringent requirements on the similarly behaving M_{eff} and $H_{\text{T}}{}^{PP}_{2,1}/H_{\text{T}}{}^{PP}_{4,1}$ variables result in a larger overlap between the M_{eff}-based and RJR-based signal regions. Conversely, signal regions designed for increasingly compressed mass spectra have looser M_{eff} and $H_{\text{T}}{}^{PP}_{2,1}/H_{\text{T}}{}^{PP}_{4,1}$, and backgrounds must be suppressed with other, complementary, kinematic requirements. As these additional kinematic observables can be quite different between Meff-based and RJR-based approaches, the orthogonality of these respective SRs increases with decreasing sparticle mass splittings as can be seen in Fig. 10.2.

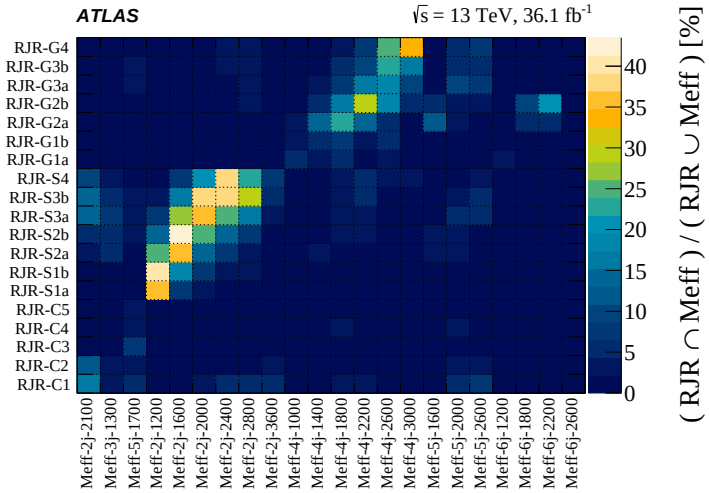

Figure 10.2: Fractional overlap of data events selected in M_{eff}-based and RJR-based SRs. M_{eff}-based SRs are listed along the x-axis with RJR-based regions on the y-axis. The intersection events falling in each pair of regions, normalized by the union, is shown on the z-axis.

Each of the axes listing the various SRs are organized in the same order, with SRs targeting compressed mass spectra in the lower left of the figure, followed by squark regions with increasing sparticle masses, and then gluinos with increasing mass. This ordering results in a diagonal pattern of larger overlap, as SRs targeting the same signals are more similar. The SRs searching for evidence of squark production (RJR-Sx and M_{eff}-2j-x) have fractions of overlapping events between 25% and 45%, while those targeting gluino production (RJR-Gx and M_{eff}-4j-x) have smaller intersections, ranging from a few percent to 35%. This decrease in overlap for gluino SRs follows from increasing differences between the selections used in the M_{eff}-based and RJR-based approaches. While observables such as $E_{\text{T}}^{\text{miss}}/M_{\text{eff}}(N_{\text{j}})$ and aplanarity are sensitive to global event properties, the RJR-based analysis for gluinos

attempts to decompose the event into two hemispheres representing each gluino. Kinematic variables used in the definitions of SRs are calculated from each hemisphere independently, providing complementarity to those describing the total event. Using this additional information in the RJR-based selections leads to generally tighter SRs, adding increased sensitivity for intermediate mass splittings.

10.6 Background estimation

A variety of SM background processes contribute to the event counts in the signal regions. The largest backgrounds in both searches presented here are: Z+jets, W+jets, top quark pair, single top quark, diboson and multi-jet production. Non-collision backgrounds are negligible.

10.6.1 Electroweak background estimation

Generally, the largest background results from an irreducible component of Z+jets events in which $Z \to \nu\bar{\nu}$ decays generate large E_T^{miss}. Similarly, most of the W+jets background is composed of $W \to \tau\nu$ events in which the τ-lepton decays to hadrons, with additional contributions from $W \to e\nu, \mu\nu$ events in which no baseline electron or muon is reconstructed, with E_T^{miss} due to neutrinos. Top quark pair production, followed by semileptonic decays, in particular $t\bar{t} \to b\bar{b}\tau\nu qq'$ (with the τ-lepton decaying to hadrons), as well as single-top-quark events, can also generate large E_T^{miss} and satisfy the jet and lepton-veto requirements. Each of these primary backgrounds is estimated using dedicated control regions CRY, CRW and CRT, as described in the

following section, while diboson production is estimated with MC simulated data normalized using NLO cross-section predictions.

Fake-lepton backgrounds are ignored in CRW, CRT and VRZ. For CRW (and even more for CRT), mainly because the fake-lepton background decreases quickly with E_T^{miss}. This is checked by data-driven fake-lepton event estimation using early data. The fake-photon background in CRY is studied with ABCD technique using photon ID and isolation variable, and also shape fit of isolation variables. This is found to be 5% of the original background but has no dependance on kinematic variables.

10.6.2 QCD multi-jet background estimation

The baseline multi-jet background estimation method is data driven approach called the "jet smearing method", and is used to provide transfer functions between the multi-jet control regions (CRQs) and their associated signal regions. The jet smearing method is a data-driven method for estimating backgrounds in event topologies where missing eneregy mainly originates from the jet mismeasurement.

The multi-jet background in the signal regions is due to missing transverse momentum from misreconstruction of jet energies in the calorimeters, jets misidentified as electrons, jets lost due to the JVT requirement, as well as neutrinos from semileptonic decays of heavy-flavor hadrons. After applying the requirements based on Δ_{QCD}, $p_{\text{T j2}}^{PP}/H_{\text{T 2,1}}^{PP}$ and $\Delta_\phi(\text{jet}, E_T^{\text{miss}})_{\text{min}}$ in the RJR-based search, as indicated in Tables 10.7 and 10.8, the remaining multi-jet background is negligible.

10.7 Control regions

In order to estimate the expected background yields, control regions are defined for each of the signal regions in four different final states. They are chosen to be orthogonal to the SR selections in order to provide independent data samples enriched in particular background sources, and are used to normalize the background MC simulation. The CR selections are optimized to maintain adequate statistical precision while minimizing the systematic uncertainties arising from the extrapolation of the CR event yield to estimate the background in the SR. Requirements on discriminating variables are chosen to match those used in the SRs as closely as possible. The basic CR definitions in both searches are listed in Table 10.9.

Table 10.9: Control region definitions as well as the main targeted SR backgrounds, the process used to model the background, and the main CR requirement(s) used to select this process. The transverse momenta of high-purity leptons (photons) used to select CR events must exceed 150 GeV.

CR	SR background	CR process	CR selection
CRγ	$Z \to \nu\bar{\nu}$+jets	γ+jets	Isolated photon
CRQ	Multi-jet	Multi-jet	$\Delta_{\mathrm{QCD}} < 0$ reversed requirement on $H_{1,1}^{PP}$ (RJR-S/G) or $R_{\mathrm{ISR}} < 0.5$ (RJR-C)
CRW	$W \to \ell\nu$+jets	$W \to \ell\nu$+jets	30 GeV ¡ 100 GeV, b-veto
CRT	$t\bar{t}$(+EW) and single top	$t\bar{t} \to b\bar{b}qq'\ell\nu$	30 GeV $< m_{\mathrm{T}}(\ell, E_T^{\mathrm{miss}}) <$ 100 GeV, b-tag

The γ+jets region (labeled as CRγ in Table 10.9) is used to estimate the contribution of $Z \to \nu\bar{\nu}$+jets background events to each SR by selecting a

sample of γ+jets events with $p_T(\gamma) > 150\ GeV$ and then treating the reconstructed photon as invisible in the E_T^{miss} calculation. For $p_T(\gamma)$ significantly larger than m_Z the kinematic properties of such events strongly resemble those of Z+jets events.

The W and top regions in both searches (labeled as CRW and CRT in Table 10.9) aim to select samples rich in $W \to \ell\nu$+jets and semileptonic $t\bar{t}$ background events, respectively. They use events with one high-purity lepton with $p_{\text{T}} > 27$ GeV, and differ in their number of b-jets (zero or ≥ 1, respectively). In both searches, the requirement on the transverse mass m_{T} formed by the $E_{\text{T}}^{\text{miss}}$ and a selected lepton is applied, as indicated in Table 10.9. The lepton is treated as a jet with the same momentum to model background events in which a hadronically decaying τ-lepton is produced. This estimation procedure is used to try to get a better idea of the $W(\to \ell\nu)$+jets and $t\bar{t}$ cross section in a restricted kinematic phase space, by normalizing the MC to the data for the electron and muon channels, respectively. The propagation of the number of background events from the control region to the signal region is done purely by Monte Carlo which takes into account the impact of all the differences in selection criteria between the control and signal regions.

The multi-jet background in both searches is estimated using a data-driven technique, which applies a resolution function to well-measured multi-jet events in order to estimate the impact of jet energy mismeasurements and heavy-flavor semileptonic decays on *met* and other variables. The resolution function of jets is initially estimated from MC simulation by matching 'truth' jets reconstructed from generator-level particles including muons and neutrinos to detector-level jets with $\Delta R < 0.1$ in multi-jet samples, and then is

modified to agree with data in dedicated samples to measure the resolution function.

All CRs corresponding to RJR-S (RJR-G) SRs are required to satisfy $H_{1,1}^{PP} > 800$ (700) GeV. Additionally, $H_{\mathrm{T}\,2,1}^{PP} > 1000$ GeV (for RJR-S), $H_{\mathrm{T}\,4,1}^{PP} > 1200$ GeV (for RJR-G) and $M_{\mathrm{T}\,S} > 0$ (for RJR-C) are required for CRW, CRT and CRQ regions as well. In CRW and CRT, the requirements on all the other variables used for the RJR-SR selections are chosen such that the loosest value in the SR category (RJR-S, RJR-G or RJR-C) indicated in Table 10.7 and Table 10.8 is used. No requirement on $p_{PP,\,z}^{\mathrm{lab}} / \left(p_{PP,\,z}^{\mathrm{lab}} + H_{\mathrm{T}\,N,1}^{PP}\right)$ is used for the CRQ selections in all RJR-SRs, where $N = 2$ or 4.

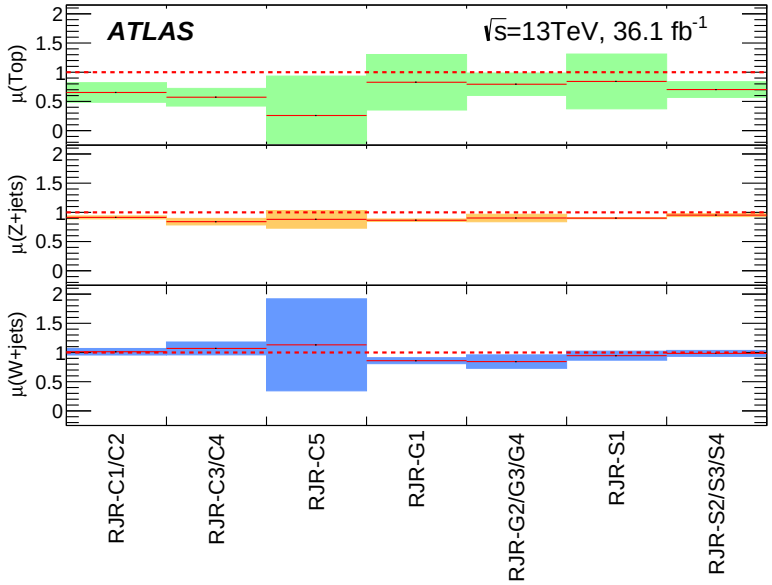

(a)

Figure 10.3: Fitted normalization factor per process as a function of the channel. The dashed horizontal lines at 1 correspond to pure MC estimates with the vertical size of the colored regions corresponding to the total uncertainty in each background source.

The normalization factors determined from the background-only fits in each CR for each background process are shown in Figure 10.3. The measured top normalization factors decrease with increasingly tight $M_{\mathrm{T}\ S}$ and $N_{\mathrm{jet}}^{\ V}$ requirements. This behavior follows from the simulated top MC samples exhibiting generally harder kinematics than observed in data. The normalization factors for W+jets and Z+jets processes are generally stable with changing kinematic selections but with a clear indication that they become

systematically smaller with increasingly strict requirements on the jet multiplicity. This is due to the MC simulation predicting jet multiplicities higher than observed in data events.

Figure 10.4 and 10.5 show the $H_{\mathrm{T}}^{PP}{}_{2,1}$ and $H_{\mathrm{T}}^{PP}{}_{4,1}$ variable distributions in control regions corresponding to RJR-S1a and RJR-G1a signal region selections, respectively. Figure 10.6 shows the $p_{\mathrm{T}}^{\mathrm{CM}}{}_{S}$ discriminating variable distributions in control regions corresponding to RJR-C1 signal region selections.

In all CRs, the data distributions are consistent with the MC background prediction within uncertainties after normalizing the dominant process in each CR.

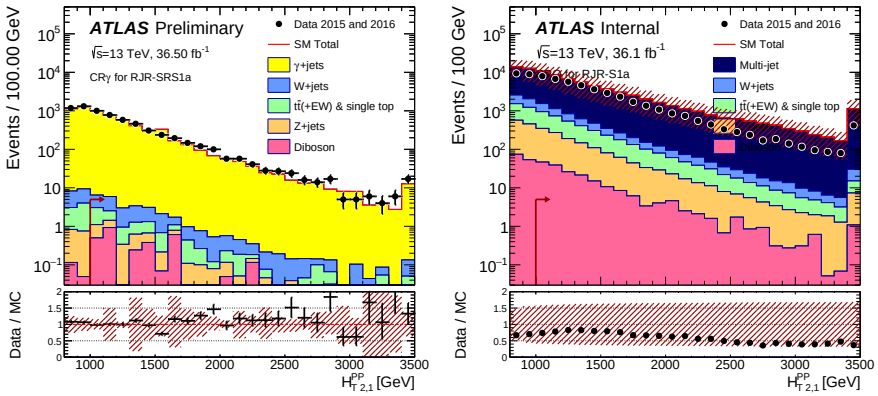

(a)

(b)

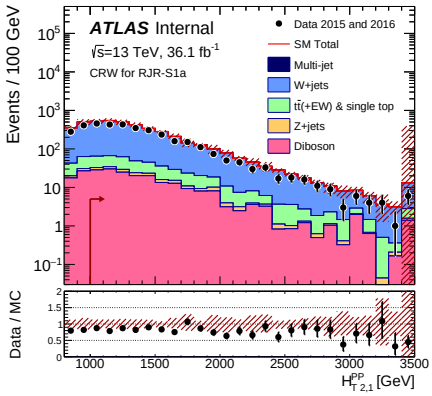

(c)

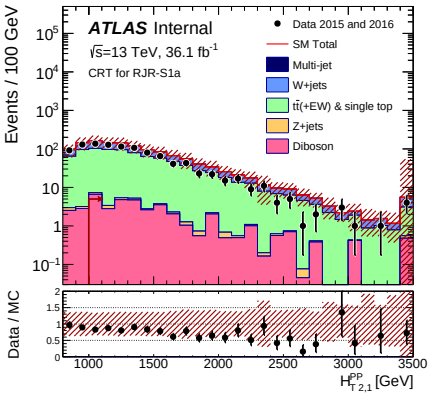

(d)

Figure 10.4: Observed $H_{\mathrm{T}\ 2,1}^{PP}$ distribution in control regions (a) CRγ, (b) CRQ, (c) CRW and (d) CRT after selecting events for the corresponding control regions as explained in the text for RJR-S1a region and after applying all selection requirements except those on the plotted variable. The arrows indicate the values at which the requirements are applied. The histograms show the MC background predictions, normalized using cross-section times integrated luminosity and the dominant process in each CR is normalized using data. In the case of γ+jets background, a κ factor is also applied. The last bin includes overflow events. The hatched (red) error bands indicate the combined experimental, MC statistical and theoretical modeling uncertainties.

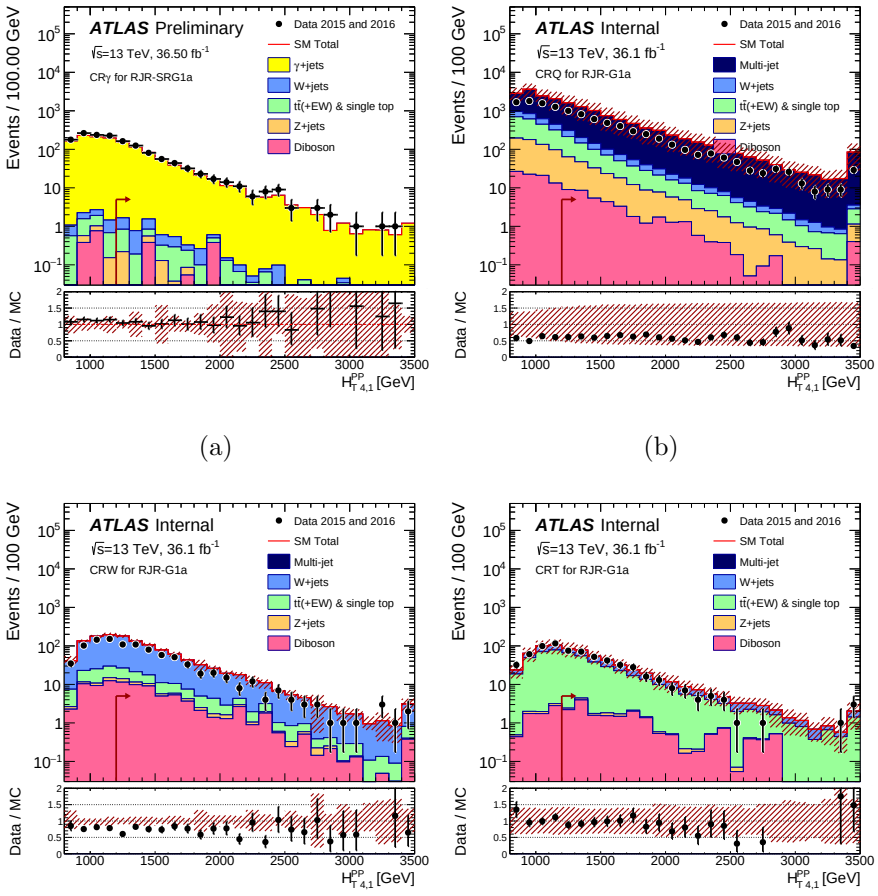

Figure 10.5: Observed $H_{\mathrm{T}\ 4,1}^{PP}$ distribution in control regions (a) CRγ, (b) CRQ, (c) CRW and (d) CRT after selecting events for the corresponding control regions as explained in the text for RJR-G1a region and after applying all selection requirements except those on the plotted variable. The arrow indicate the values at which the requirements are applied. The histograms show the MC background predictions, normalized using cross-section times integrated luminosity and the dominant process in each CR is normalized using data.

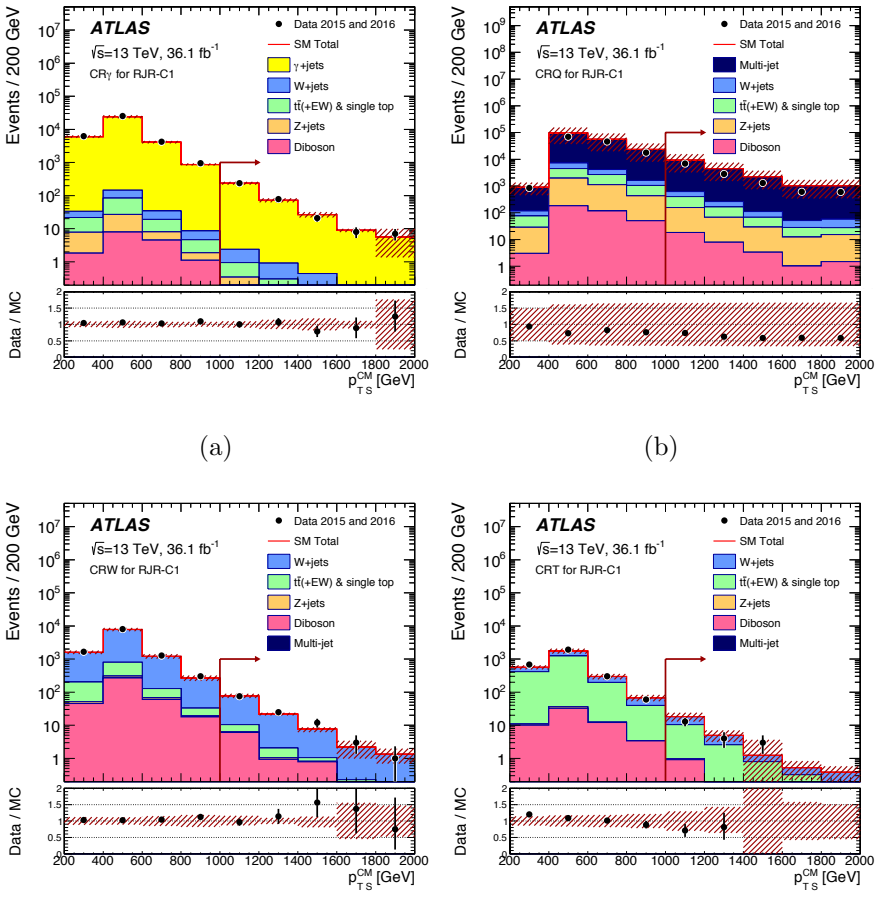

Figure 10.6: Observed $p_{\mathrm{T}\,S}^{\mathrm{CM}}$ distribution in control regions (a) CRγ, (b) CRQ, (c) CRW and (d) CRT after selecting events for the corresponding control regions as explained in the text for RJR-C1 region and after applying all selection requirements except those on the plotted variable. The arrows indicate the values at which the requirements are applied. The histograms show the MC background predictions, normalized using cross-section times integrated luminosity and the dominant process in each CR is normalized using data.

10.8 Validation Regions

The background estimation procedure is validated by comparing the numbers of events observed in the VRs to the corresponding SM background predictions obtained from the background-only fits. Several VRs are defined, with requirements distinct from those used in the CRs and that maintain low expected signal contamination. Like the CRs, the majority of the VRs are defined in final states with leptons and photons, allowing the different expected background contributions to the SRs to be validated almost separately with high-purity selections.

The CRγ estimates of the $Z(\to \nu\bar{\nu})$+jets background are validated using samples of $Z(\to \ell\bar{\ell})$+jets events selected by requiring high-purity lepton pairs of opposite sign and identical flavor for which the dilepton invariant mass lies within 25 GeV of the Z boson mass (VRZ). In VRZ regions, the leptons are treated as contributing to E_T^{miss}. Additional VRs are designed to validate the $Z(\to \nu\bar{\nu})$+jets: the VRZc region, which selects events with no leptons but inverts the $\Delta\phi_{\text{ISR},\,I}$ requirement of the SR selection (Table 10.7 and 10.8) and VRZca, which further loosens some other criteria to match the CRW and CRT regions. The VRZc regions have a purity of $Z(\to \nu\bar{\nu})$+jets of 50%–70%. In order to increase yields in the dilepton final state RJR-VRZ regions, two additional regions, RJR-VRZa and RJR-VRZb are constructed with $H_{1,1}^{PP}$ and $H_{\text{T}\,2,1}^{PP}$ (or $H_{\text{T}\,4,1}^{PP}$ where appropriate) loosened, respectively, relative to the values used for the RJR-CRW and RJR-CRT regions.

The CRW and CRT estimates of the W+jets and top quark backgrounds are validated using the same selections as for the corresponding CRs, except that the requirements on $H_{1,1}^{PP}$ and $M_{\text{T}\;S}$ (VRWa, VRTa) or $H_{\text{T}\,2,1}^{PP}$ and $H_{\text{T}\,4,1}^{PP}$

(VRWb, VRTb) are omitted. Two additional VRs that require the presence of a high-purity lepton and either veto (VRW) or require the presence of at least one b-jet (VRT), and require no additional SR selection criteria, are also used in the analysis.

The VRQ regions use the same selection as the corresponding CRQ, except that the requirements on $H_{1,1}^{PP}$, $H_{\mathrm{T}\ 2,1}^{PP}$ (or $H_{\mathrm{T}\ 4,1}^{PP}$ where appropriate) and $M_{\mathrm{T}\ S}$ are omitted depending on the region. Additional VRs with inverted Δ_{QCD} (VRQa), $H_{1,1}^{PP}$ (VRQb) for RJR-S and RJR-G signal regions, and with $0.5 < R_{\mathrm{ISR}} <$ SR requirement (VRQc) for the RJR-C region (Table 10.8), are also used.

The distributions of the main discriminating variables in the validation regions VRW, VRZ and VRT are shown in Fig. 10.7, 10.8 and 10.9 for squark gluino and compressed signal regions. In general, good agreement in distribution shape is observed in all regions, with normalization differences consistent with scale factors.

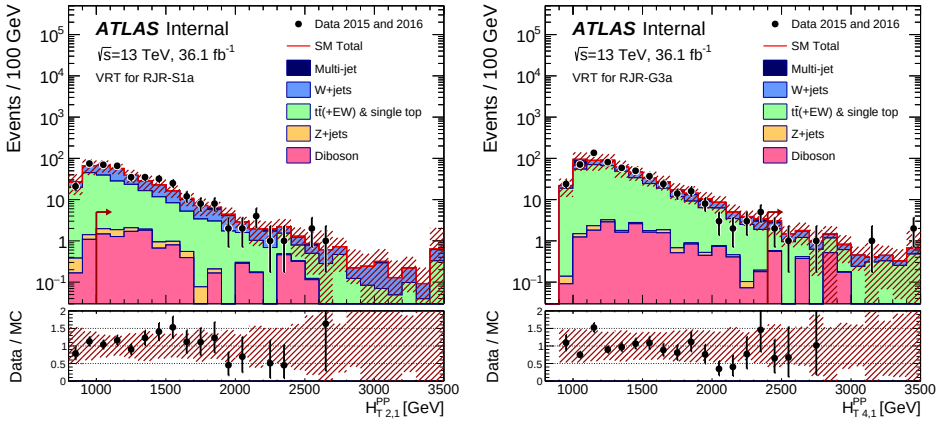

(a)

(b)

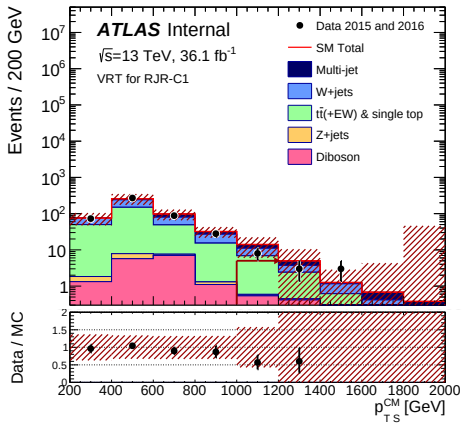

(c)

Figure 10.7: For validation region VRT, (a) discriminating variable $H_{\mathrm{T}\ 2,1}^{PP}$ distribution for squark signal region RJR-S1a, (b) discriminating variable $H_{\mathrm{T}\ 4,1}^{PP}$ distribution for gluino signal RJR-G3a, (c) discriminating variable $p_{\mathrm{T}\ S}^{\mathrm{CM}}$ distribution for compressed signal region RJR-C1. The histograms denote the MC background expectations, normalised to luminosity. The hatched (red) error bands indicate the combined experimental, MC statistical and theoretical modeling uncertainties.

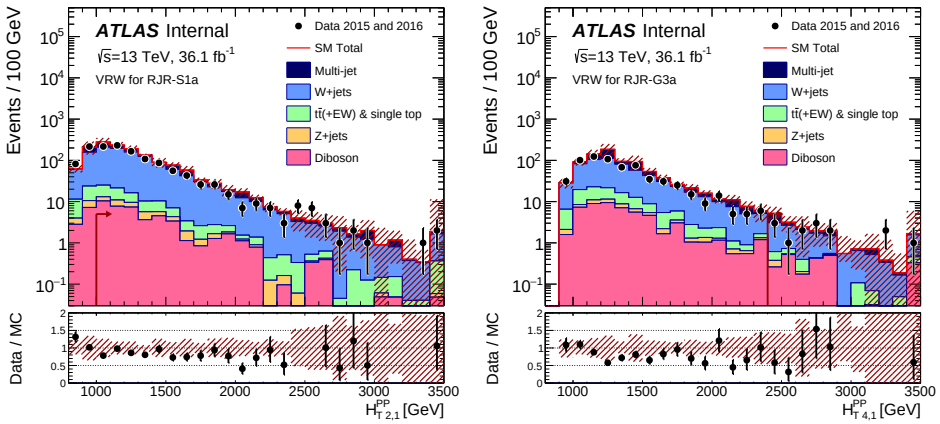

(a)

(b)

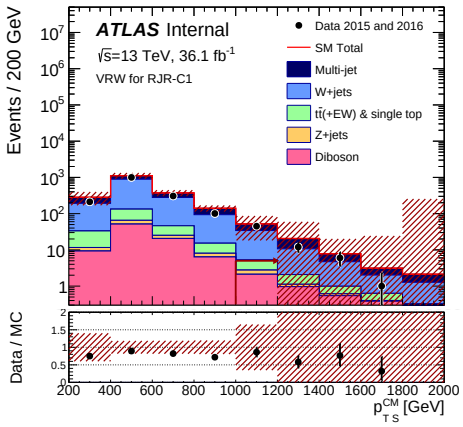

(c)

Figure 10.8: For validation region VRW, (a) discriminating variable $H_{\mathrm{T}\ 2,1}^{PP}$ distribution for squark signal region RJR-S1a, (b) discriminating variable $H_{\mathrm{T}\ 4,1}^{PP}$ distribution for gluino signal RJR-G3a, (c) discriminating variable $p_{\mathrm{T}\ S}^{\mathrm{CM}}$ distribution for compressed signal region RJR-C1.The histograms denote the MC background expectations, normalised to luminosity. The hatched (red) error bands indicate the combined experimental, MC statistical and theoretical modeling uncertainties.

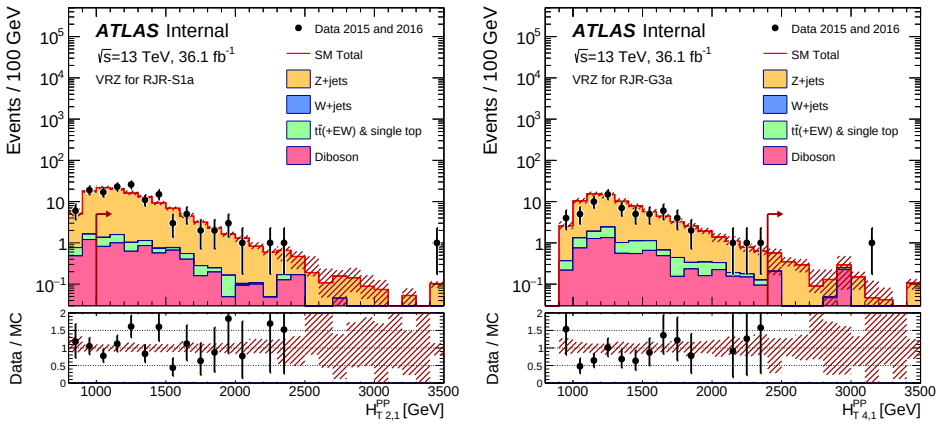

(a) (b)

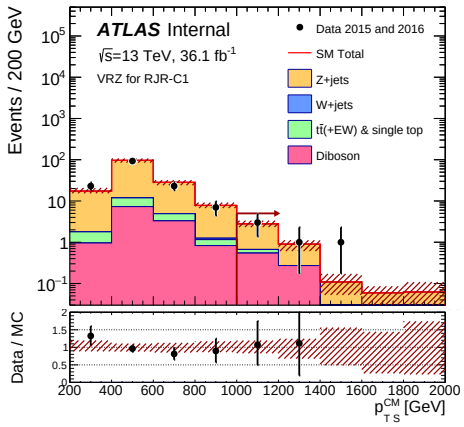

(c)

Figure 10.9: For validation region VRZ, (a) discriminating variable $H_{\mathrm{T}\ 2,1}^{PP}$ distribution for squark signal region RJR-S1a, (b) discriminating variable $H_{\mathrm{T}\ 4,1}^{PP}$ distribution for gluino signal RJR-G3a, (c) discriminating variable $p_{\mathrm{T}\ S}^{\mathrm{CM}}$ distribution for compressed signal region RJR-C1.The histograms denote the MC background expectations, normalised to luminosity. The hatched (red) error bands indicate the combined experimental, MC statistical and theoretical modeling uncertainties.

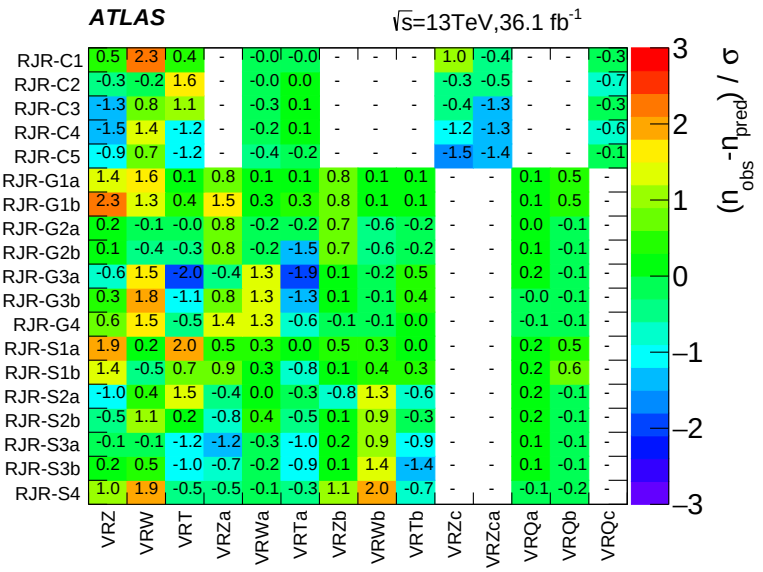

(a)

Figure 10.10: Differences between the numbers of observed events in data and the SM background predictions for each VR used, expressed as a fraction of the total uncertainty, which combines the uncertainty in the background predictions, and the expected statistical uncertainty of the test obtained from the number of expected events. Empty boxes (indicated by a '-') are when the VR is not used for the corresponding SR selection.

The results of the validation procedure are shown in Figure 10.10, where the difference in each VR between the numbers of observed and expected events, expressed as fractions of the one-standard deviation (1σ) uncertainties in the latter, are summarized. No significant systematic biases are observed for both searches, with the largest discrepancies being 2.3σ in VRW associated with the SR RJR-G1b out of 194 VRs.

10.9 Systematic uncertainties

Systematic uncertainties in background estimates arise from the use of extrapolation factors that relate observations in the control regions to background predictions in the signal regions, and from the MC modeling of minor backgrounds.

The overall background uncertainties, detailed in Figure 10.11, range from 10% in SRs RJR-S1a, RJR-S2a, RJR-G1a and RJR-C2 to 30% in SR RJR-G4.

For the backgrounds estimated with MC simulation-derived extrapolation factors, the primary common sources of systematic uncertainty are the jet energy scale (JES) calibration, jet energy resolution (JER), theoretical uncertainties, and limited event yields in the MC samples and data CRs. Correlations between uncertainties (for instance between JES or JER uncertainties in CRs and SRs) are taken into account where appropriate.

JES and JER are estimated using the methods explained in Refs. [94–96].An additional uncertainty in the modeling of energy not associated with reconstructed objects, used in the calculation of E_T^{miss} and measured with unassociated charged tracks, is also included.

The combined JES, JER and E_T^{miss} uncertainty ranges from 1% in RJR-C4 to 14% in RJR-G4.

The Jet mass Scale uncertainty is estimated using the same procedure as Ref. [97].

A 20% uncertainty is conservatively assigned to the Jet mass resolution (JMR).

Uncertainties arising from theoretical modeling of background processes

are estimated by comparing samples produced with different MC generators or by varying the scales. Uncertainties in W/Z+jets production are estimated by increasing and decreasing the renormalization, factorization and resummation scales by a factor of two, and by increasing and decreasing the nominal CKKW matching scale, 20 GeV, by 10 GeV and 5 GeV, respectively.

Uncertainties in the modeling of top quark pair production are estimated by comparing samples generated with POWHEG-BOX and MG5_aMC@NLO, and by comparing the nominal sample with samples generated using different shower tunes. Uncertainties associated with PDF modeling of top quark pair production are found to be negligible. Uncertainties in diboson production due to PDF, renormalization and factorization scale uncertainties (estimated by increasing and decreasing the scales used in the MC generators by a factor of two for all combinations and taking the envelope of them) are accounted for.

These combined uncertainties range from 8% in RJR-S1a to 18% in RJR-G4, with the smaller range largely due to the absence of 6-jet SRs. Uncertainties associated with the modeling of Z+jets production are largest in RJR-S2b and RJR-S3b SR (8%). The impact of lepton reconstruction uncertainties, and of the uncertainties related to the b-tag/b-veto efficiency, on the overall background uncertainty is found to be negligible for all SRs.

The uncertainties arising from the data-driven correction procedure applied to events selected in the CRγ region, described in Section 10.6, are included in Figure 10.11 under 'CR statistical uncertainty'. Other uncertainties due to CR data sample size range from 4% to 20% for RJR SRs. The statistical uncertainty arising from the use of MC samples is largest in

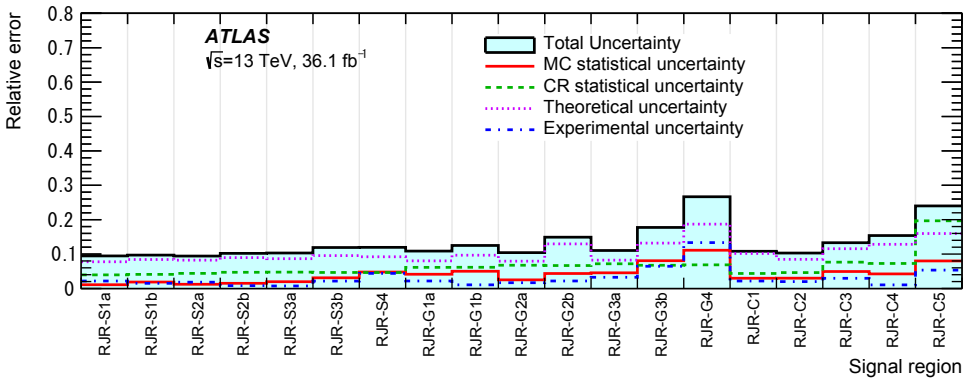

(a)

Figure 10.11: Breakdown of the largest systematic uncertainties in the background estimates. The individual uncertainties can be correlated, such that the total background uncertainty is not necessarily their sum in quadrature.

RJR-G4 (12%). Uncertainties related to the multi-jet background estimates are taken into account by applying a uniform 100% uncertainty to the multi-jet yield in all SRs. In most of the SRs these uncertainties are negligible, and the maximum resulting contribution to the overall background uncertainty is less than 1%. Experimental uncertainties (JES, JER, JMS, JMR and E_T^{miss}) and MC statistical uncertainty in the SUSY signals are estimated in the same way as for the background and are less than a few percent for most of the signals. The signal cross-section uncertainty is estimated by computing the changes when the renormalization and factorization scale, PDF and the strong coupling constant (α_s) are varied. The uncertainties in the amount of ISR and FSR in the SUSY signals are estimated by varying generator tunes

in the simulation as well as scales used in the matrix-element generator as a function of the mass difference, Δm, between gluino (or squark) and $\tilde{\chi}_1^0$. This uncertainty reaches 20% in the limit of no mass difference and is negligible for $\Delta m > 200$ GeV.

10.10 HistFitter

HistFitter [98] is a statistical tool that is used by the SUSY analysis at ATLAS to fit, interpret and present binned likelihood fits and follow-up with their statistical interpretation. HistFitter is a programmable and flexible framework, it starts with an object-oriented configuration file, customized to the analysis. Then builds probability density functions that are automatically fitted to data and interpreted with statistical tests. Although the user-interface and it's underlying configuration file are written in python, the executing external computational software that histfitter sits on are compiled in C++.

So the Histfitter package gives us [98]:

- a **programmable framework** performing a complete analysis from a simple configuration file.
- an **analysis strategy**: common physics analysis strategies like the Control regions, Validation or signal regions are woven into it's framework design.
- **Bookkeeping**: it can keep track of numerous data models, from histogram production until final statistical results. This is very useful

when working with large collections of signal hypotheses

- **Presentation and interpretation**: multiple methods are provided to determine statistical significance of signal hypotheses, and produce publication quality tables and plot summarizing the fit results.

We programme HistFitter to build and test a set of data models. To do this, we take the user defined configuration file and the raw input data. The processing sequence of HistFitter is split in three stages as shown by Fig. 10.12.

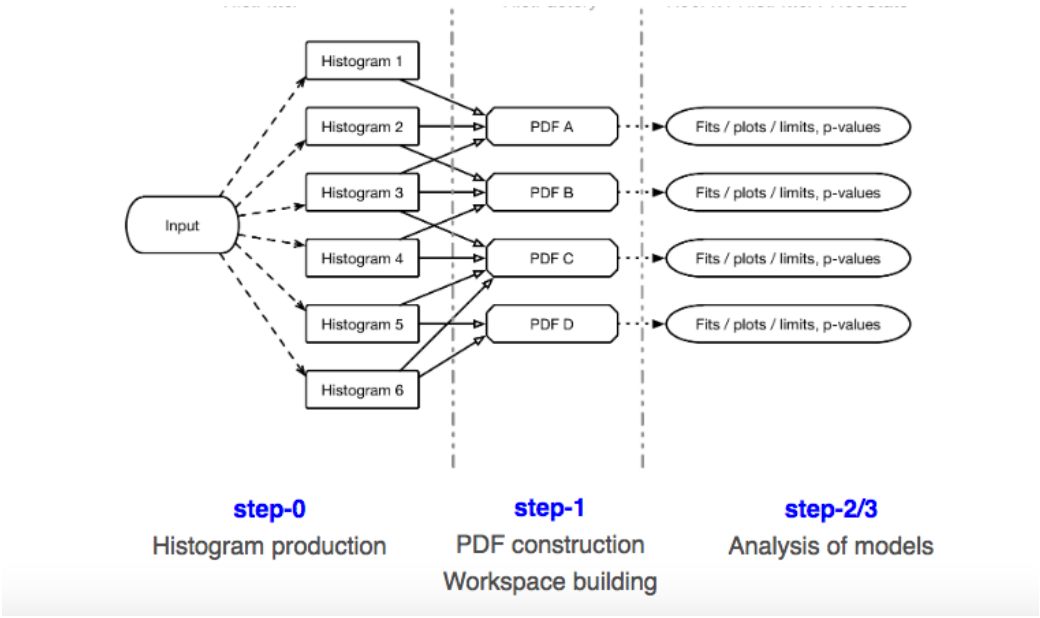

Figure 10.12: Overview of the HistFitter processing sequence.

- Step 0: Using the user-defined python configuration, HistFitter prepares initial histograms with ROOT and the input data that models the physics process the analysis is looking for.

- Step 1: The generated histograms are combined to construct a corresponding PDF following the recommendations in the config file. Each PDF is stored in a workspace, together with the dataset and model configuration.

- Step 2: An analysis of the model is done by performing fits of the data, statistical tests and producing pull plots and yield tables.

HistFitter provides the functionality to perform hypothesis tests of the data, and to interpret the corresponding results in the form of histograms and tables. Different fit strategies are used dependent on the combination of CRs, VRs and SRs and on the fact that we include a signal model or not. Histfitter basically designs and implements fit strategies requested by the analysis.

The three most common used likelihood fit strategies are as follows:

Background only fits:

As the name suggests only background samples or control regions are used in this fit so the dominant background processes are normalized to the observed event counts in these regions. Basically this fit is used in two places: First the background predictions are used to validate the correct background event yields in the signal and validation regions and give an unbiased comparison between the predicted and observed number of events in these regions. And secondly when you have an independent background estimate in SR you can run hypothesis testing on it for any signal model. The scale factors represent the normalization of background components relative to MC predictions ($\mu(W+\text{jets})$, $\mu(Z+\text{jets})$, $\mu(\text{Top})$), and are simultaneously determined in the fit to all the CRs associated with a SR. The expected background

in the SR is based on the yields predicted by simulation for W/Z+jets and background processes containing top quarks, corrected by the scale factors derived from the fit. In the case of multi-jet background, the estimate is based on the data-driven method described in Section 10.6. The systematic and MC statistical uncertainties in the expected values are included in the fit as nuisance parameters that are constrained by Gaussian distributions with widths corresponding to the sizes of the uncertainties considered and by Poisson distributions, respectively.

Model dependent fits:

This fit is run for a specific signal model. If we see no signal excess in our results then we can use this fit to put exclusion limits on our model, if we do see excess of events we can use this fit to measure properties like signal strength μ of the model. For an analysis a grid of signal points is created varying some model parameters e.g in our for case the masses of the supersymmetric particles. Then we generate signal samples for these points and run the model dependent fit on all of the CRs and SRs. The fit can be run on all these regions simultaneously as long as they are orthogonal and non-overlapping to increase the exclusion sensitivity. Correlations between signal and background systematic uncertainties are taken into account where appropriate. Signal-yield systematic uncertainties due to detector effects and the theoretical uncertainties in the signal acceptance are included in the fit.

Model Independent fits:

This fit is used for setting model independent upper limits on the number of events greater than the predicted number of events in each signal region defined by the analysis. So for anyone studying a particular model can look

at the predictions of these fits and see if their model is excluded or not for that signal region. Both CRs and SRs are used in this fit but there is no signal contamination in the CRs and the events in the SRs are dumped in a single bin to remove any model dependency. The number corresponding to the event yield is only used an input to the fit. This fit proceeds in the same way as the background-only fit, where yields in the CRs are used to constrain the predictions of backgrounds in each SR, while the SR yield is also used in the likelihood with an additional nuisance parameter describing potential signal contributions. The observed and expected upper limits at 95% confidence level (CL) on the number of events from BSM phenomena for each signal region (S^{95}_{obs} and S^{95}_{exp}) are derived using the CL_s prescription, neglecting any possible signal contamination in the CRs. These limits, when normalized by the integrated luminosity of the data sample, may be interpreted as upper limits on the visible cross-section of BSM physics ($\langle\epsilon\sigma\rangle^{95}_{\text{obs}}$), where the visible cross-section is defined as the product of production cross-section, acceptance and efficiency. The model-independent fit is also used to compute the one-sided p-value (p_0) of the background-only hypothesis, which quantifies the statistical significance of an excess.

Chapter 11

Results, interpretation and exclusion limits

11.1 Exclusion Results

Distributions of the final discriminating variables, $H_{\mathrm{T}\,2,1}^{PP}$ ($H_{\mathrm{T}\,4,1}^{PP}$ where appropriate) in selected RJR-S and RJR-G regions, and $p_{\mathrm{T}\,S}^{\mathrm{CM}}$ in selected RJR-C regions, after applying all other selection requirements except those based on the plotted variable, are shown in Figures 11.1, 11.2, 11.3, 11.4 and 11.5. Examples of SUSY signals are also shown for illustration. These signals correspond to the processes to which each SR is primarily sensitive: $\tilde{q}\tilde{q}$ production for the lower jet-multiplicity SRs and $\tilde{g}\tilde{g}$ production for the higher jet-multiplicity SRs. In these figures, data and background distributions largely agree within uncertainties.

The number of events observed in the data and the number of SM events expected to enter each of the signal regions, determined using the background-

only fit, are shown in Table 11.1, 11.2, 11.3 and in Figure 11.6. The pre-fit background predictions are also shown in Table 11.1, 11.2 and 11.3 for comparison. The background normalizations for each SR are fit to reproduce the event yields observed in the CRs. This is in particular seen in Figure 10.3, leading to agreement between data and post-fit background predictions in most of the SRs. The most significant observed excess across the signal regions with a p-value for the background-only hypothesis of 0.01, corresponding to a significance of 2.5 standard deviations, occurs in SR RJR-S1a (Table 11.1).

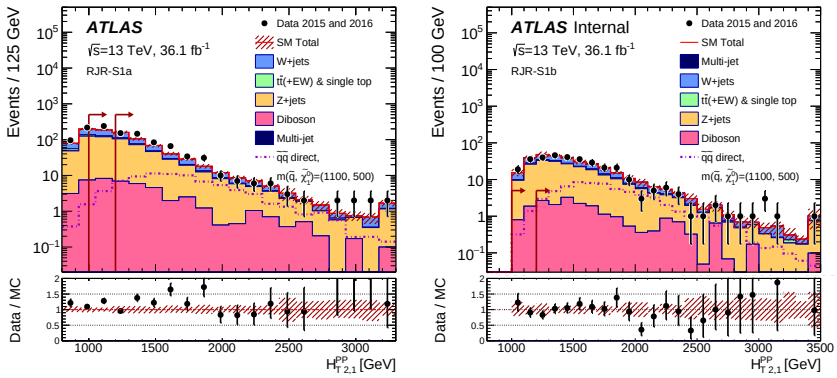

(a) (b)

(c) (d)

Figure 11.1: Observed $H_{\mathrm{T}\,2,1}^{PP}$ distributions for the squark regions after applying all selection requirements except those on the plotted variable.

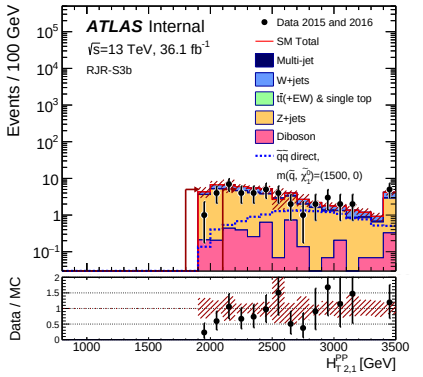

(a)

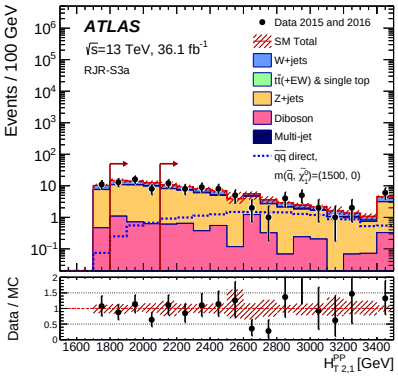

(b)

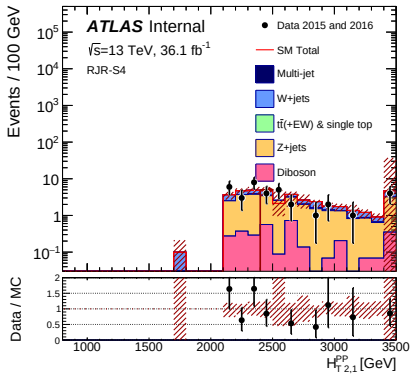

(c)

Figure 11.2: Observed $H_{\mathrm{T}\,2,1}^{PP}$ distributions for the squark regions after applying all selection requirements except those on the plotted variable.

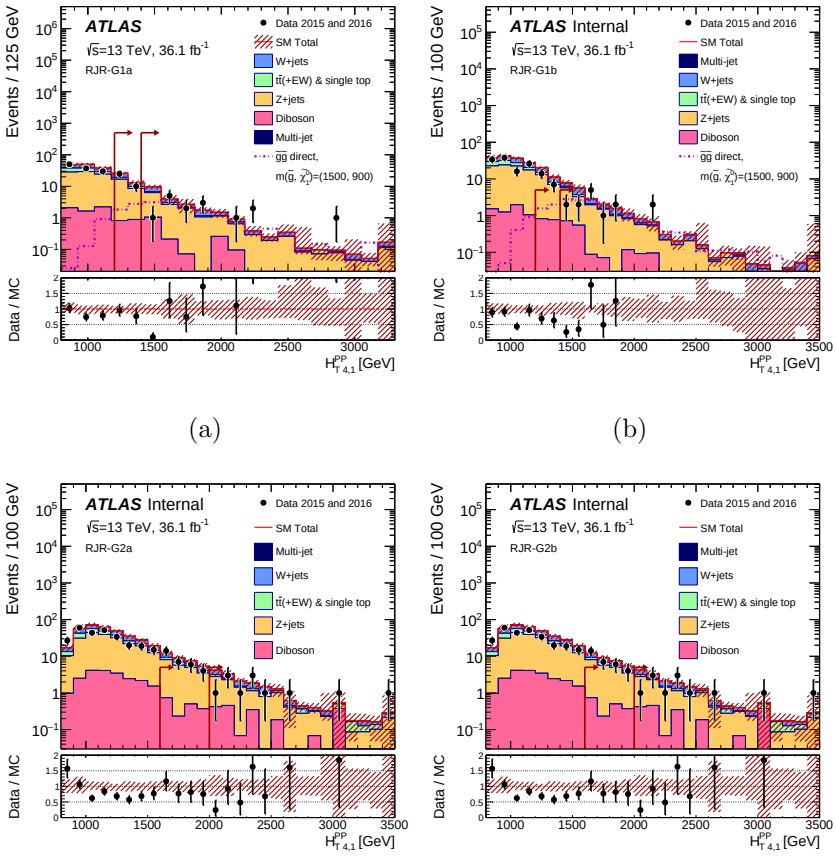

(a) (b)

(c) (d)

Figure 11.3: Observed $H_{\mathrm{T}\ 4,1}^{PP}$ distributions for the gluino regions after applying all selection requirements except those on the plotted variable.

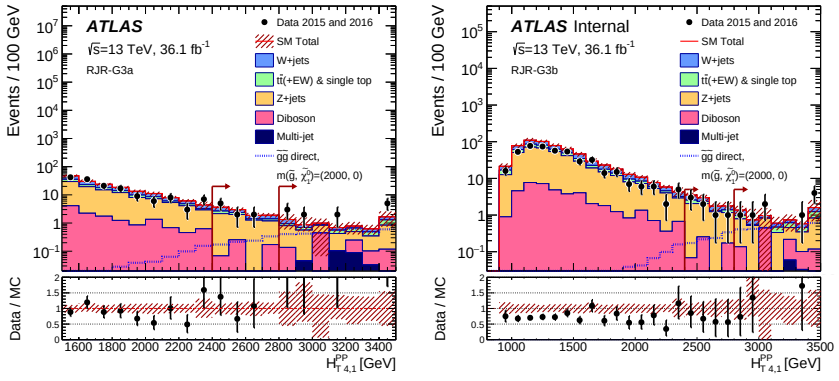

(a) (b)

(c)

Figure 11.4: Observed $H_{\mathrm{T}\ 4,1}^{PP}$ distributions for the gluino regions after applying all selection requirements except those on the plotted variable.

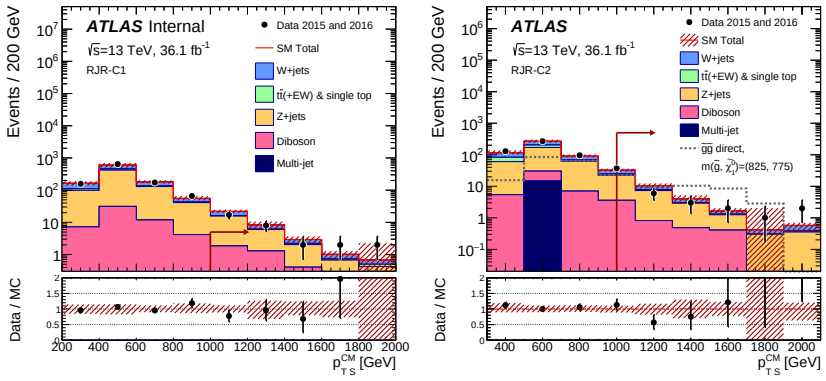

(a)

(b)

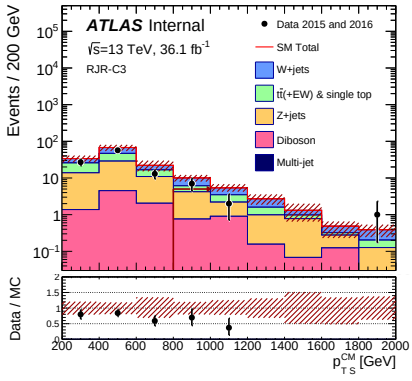

(c)

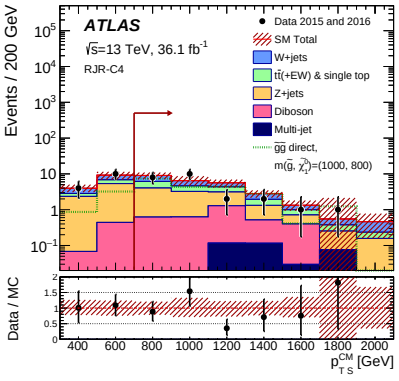

(d)

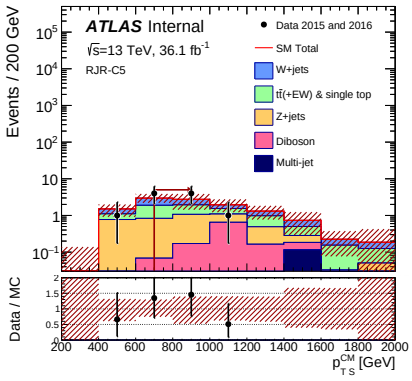

(e)

Figure 11.5: Observed $p_{\mathrm{T}}{}_S^{CM}$ distributions for the compressed regions as defined in the signal regions, after applying all selection requirements except those on the plotted variable.

These histograms show the MC background predictions prior to the fits described in the text, normalized using cross-section times integrated luminosity. The last bin includes the overflow. The hatched (red) error bands indicate the combined experimental and MC statistical uncertainties. The arrows indicate the values at which the requirements on the plotted variable are applied. When two arrows are shown, these correspond to the looser SR variation 'a' and the tighter variation 'b'. Expected distributions for benchmark signal model points, normalized using NLO+NLL cross-section times integrated luminosity, are also shown for comparison (masses in GeV).

Now to do hypothesis testing on our new physics specific signal model, it is tested against the background-only assumption. Signal model predicted events are present in all CRs and SRs, as implemented in the model-dependent signal/exclusion limit fit which we discussed previously in the histfitter section. HistFitter package helps to visualize the results of this hypothesis testing. The signal strength μ is set as a parameter of interest for this fit. When μ is zero it corresponds to the background-only model, and when μ is one it corresponds to the background plus signal model. First we run a fit for background + signal regions using the signal strength μ as a free parameter to check that the fit is not failing potential hypotest results would be stored by the histfitter and it's parameters can be stored.

Then repeated hypothesis tests are run for a multitude of signal models making up a specific model grid, e.g. by modifying parameters for a specific supersymmetric signal model. The results in form observed and predicted CLs and p-values for every signal model are collected in a data text file. At this point only those hypotest results are saved who had a successful initial

free fit. After this another macro is used to convert this text file to a ROOT file and convert these entries into two dimensional histograms which show CLs and p-values against supersymmetric particle's masses. Lastly, another macro which utilizes a linear algorithm is used to interpolate the CLs values where the CLs value is equal to 0.05.

The p-values are the probabilities to obtain a value equal to or larger than that observed in the data. The p_0 is the probability of the observation to be consistent with the background. For an observed number of events lower than expected, the p-value is truncated at 0.5. In addition to p-values, the number of equivalent Gaussian standard deviations (Z) is given in parentheses. Also shown are 95% CL upper limits on the visible cross-section ($\langle\epsilon\sigma\rangle^{95}_{\rm obs}$) defined as the product of acceptance, reconstruction efficiency and of production cross section, the upper limits on the visible number of signal events ($S^{95}_{\rm obs}$) and the number of signal events ($S^{95}_{\rm exp}$) given the expected number of background events (and $\pm1\sigma$ excursions of the expected number).

In the absence of a statistically significant excess, limits are set on contributions to the SRs from BSM physics. Upper limits at 95% CL on the number of BSM signal events in each SR and the corresponding visible BSM cross-section are derived from the model-independent fits using the CLs prescription. Limits are evaluated using MC pseudo-experiments. The results are presented in Table 11.1, 11.2 and 11.3.

Table 11.1: Numbers of events observed in the signal regions used for squarks compared with background predictions obtained from the fits described in the text.

Signal Region	**RJR-S1a**	**RJR-S1b**	**RJR-S2a**	**RJR-S2b**	**RJR-S3a**	**RJR-S3b**	**RJR-S4**
MC expected events							
Diboson	37	17	23	10.3	7.2	3.5	2.0
Z/γ^*+jets	495	189	222	102	70	30.5	17.9
W+jets	220	77	84	36	22.6	9.2	5.3
$t\bar{t}$(+EW) + single top	32	9.2	10.9	4.7	2.6	1.17	0.68
Fitted background events							
Diboson	37 ± 8	17 ± 4	23 ± 5	10.3 ± 2.6	7.2 ± 1.5	3.5 ± 1.1	2.0 ± 0.5
Z/γ^*+jets	450 ± 40	170 ± 14	211 ± 17	97 ± 8	67 ± 5	29.0 ± 2.4	17.0 ± 1.5
W+jets	208 ± 27	73 ± 9	83 ± 12	35 ± 5	22.3 ± 3.0	9.0 ± 1.3	5.2 ± 0.9
$t\bar{t}$(+EW) + single top	27 ± 26	7.4 ± 2.0	7.6 ± 3.2	3.3 ± 1.2	1.9 ± 0.5	0.82 ± 0.34	$0.49^{+0.51}_{-0.49}$
Multi-jet	18 ± 17	1.3 ± 1.3	0.6 ± 0.6	0.31 ± 0.31	0.27 ± 0.27	0.03 ± 0.03	0.03 ± 0.03
Total MC	1830	370	378	172	120	45.9	27.7
Total bkg	740 ± 50	268 ± 18	326 ± 22	146 ± 10	98 ± 6	42.4 ± 3.0	24.7 ± 2.1
Observed	880	325	365	170	102	46	23
$\langle \epsilon\sigma \rangle^{95}_{\rm obs}$ [fb]	6.45	2.76	1.89	1.38	0.69	0.51	0.30
$S^{95}_{\rm obs}$	233	99.5	68.3	49.9	24.7	18.3	10.7
$S^{95}_{\rm exp}$	120^{+44}_{-34}	50^{+18}_{-13}	50^{+14}_{-10}	32^{+14}_{-8}	24^{+11}_{-6}	$15.5^{+5.9}_{-3.4}$	$11.6^{+4.5}_{-3.9}$
p_0 (Z)	0.01 (2.52)	0.01 (2.34)	0.14 (1.07)	0.10 (1.30)	0.50 (0.00)	0.50 (0.00)	0.50 (0.00)

Table 11.2: Numbers of events observed in the signal regions used for gluinos compared with background predictions obtained from the fits described in the text.

Signal Region	**RJR-G1a**	**RJR-G1b**	**RJR-G2a**	**RJR-G2b**	**RJR-G3a**	**RJR-G3b**	**RJR-G4**
MC expected events							
Diboson	3.1	1.6	2.8	1.34	0.80	0.37	0.24
Z/γ^*+jets	28.7	13.1	28.1	9.4	8.8	3.0	2.09
W+jets	14.0	6.4	14.6	5.0	4.7	1.7	1.0
$t\bar{t}$(+EW) + single top	6.0	2.0	6.5	2.0	3.1	1.5	1.1
Fitted background events							
Diboson	3.1 ± 0.7	1.6 ± 0.5	2.8 ± 0.8	1.34 ± 0.33	0.80 ± 0.27	0.36 ± 0.29	0.24 ± 0.11
Z/γ^*+jets	24.8 ± 2.7	11.3 ± 1.4	25.4 ± 2.9	8.4 ± 1.2	7.9 ± 1.1	2.7 ± 0.7	1.89 ± 0.35
W+jets	12.0 ± 1.7	5.5 ± 0.9	12.3 ± 2.1	4.2 ± 0.8	3.9 ± 0.7	1.5 ± 0.6	0.85 ± 0.29
$t\bar{t}$(+EW) + single top	4.8 ± 0.9	1.6 ± 1.4	5.2 ± 1.9	1.6 ± 0.6	2.4 ± 0.9	1.2 ± 1.0	0.9 ± 0.8
Multi-jet	0.25 ± 0.25	0.13 ± 0.13	0.5 ± 0.5	0.2 ± 0.2	0.5 ± 0.5	0.26 ± 0.25	$0.18^{+0.18}_{-0.18}$
Total MC	66.8	30.9	80.4	28.9	44.4	21.1	14.4
Total bkg	45 ± 4	20.1 ± 2.3	46 ± 4	15.8 ± 1.8	15.6 ± 1.7	6.0 ± 1.4	4.1 ± 0.9
Observed	42	16	52	15	21	12	6
$\langle\epsilon\sigma\rangle^{95}_{\rm obs}$ [fb]	0.44	0.25	0.63	0.26	0.42	0.38	0.22
$S^{95}_{\rm obs}$	15.9	8.9	22.7	9.4	15.2	13.9	7.8
$S^{95}_{\rm exp}$	$16.6^{+6.7}_{-5.0}$	$11.0^{+4.1}_{-2.7}$	$16.7^{+6.8}_{-4.8}$	$9.9^{+4.1}_{-2.5}$	$10.7^{+3.4}_{-3.1}$	$10.3^{+2.7}_{-2.1}$	$6.3^{+1.9}_{-2.1}$
p_0 (Z)	0.50 (0.00)	0.50 (0.00)	0.19 (0.89)	0.50 (0.00)	0.11 (1.21)	0.07 (1.50)	0.24 (0.72)

Table 11.3: Numbers of events observed in the signal regions used in the compressed analysis compared with background predictions obtained from the fits described in the text.

Signal Region	**RJR-C1**	**RJR-C2**	**RJR-C3**	**RJR-C4**	**RJR-C5**
MC expected events					
Diboson	4.5	3.4	1.6	2.7	0.8
Z/γ^*+jets	24.8	20.7	7.8	10.3	2.3
W+jets	9.8	7.4	8.3	8.0	2.4
$t\bar{t}$(+EW) + single top	1.32	1.6	5.5	6.9	3.39
Fitted background events					
Diboson	4.5 ± 1.0	3.4 ± 0.8	1.6 ± 0.5	2.7 ± 0.7	0.8 ± 0.5
Z/γ^*+jets	22.6 ± 2.3	18.9 ± 2.0	6.5 ± 1.2	8.6 ± 1.2	2.1 ± 0.6
W+jets	9.9 ± 1.9	7.5 ± 1.4	8.9 ± 1.4	8.6 ± 1.4	2.7 ± 2.1
$t\bar{t}$(+EW) + single top	$0.86^{+1.00}_{-0.86}$	1.0 ± 0.7	3.2 ± 1.5	4.0 ± 2.4	$0.89^{+2.17}_{-0.89}$
Multi-jet	0.06 ± 0.06	0.33 ± 0.33	0.5 ± 0.5	0.8 ± 0.8	$0.25^{+0.26}_{-0.25}$
Total MC	43.9	53.3	54.8	84.0	28.0
Total bkg	37.9 ± 3.5	31.2 ± 2.9	20.7 ± 2.6	24.8 ± 3.3	6.7 ± 1.3
Observed	36	29	12	24	10
$\langle \epsilon\sigma \rangle^{95}_{\text{obs}}$ [fb]	0.38	0.35	0.18	0.42	0.30
S^{95}_{obs}	13.8	12.7	6.4	15.2	10.7
S^{95}_{exp}	$15.3^{+5.7}_{-4.7}$	$14.0^{+5.0}_{-4.2}$	$11.2^{+4.4}_{-3.5}$	$15.2^{+4.5}_{-3.5}$	$7.8^{+2.7}_{-2.0}$
p_0 (Z)	0.50 (0.00)	0.50 (0.00)	0.50 (0.00)	0.50 (0.00)	0.14 (1.06)

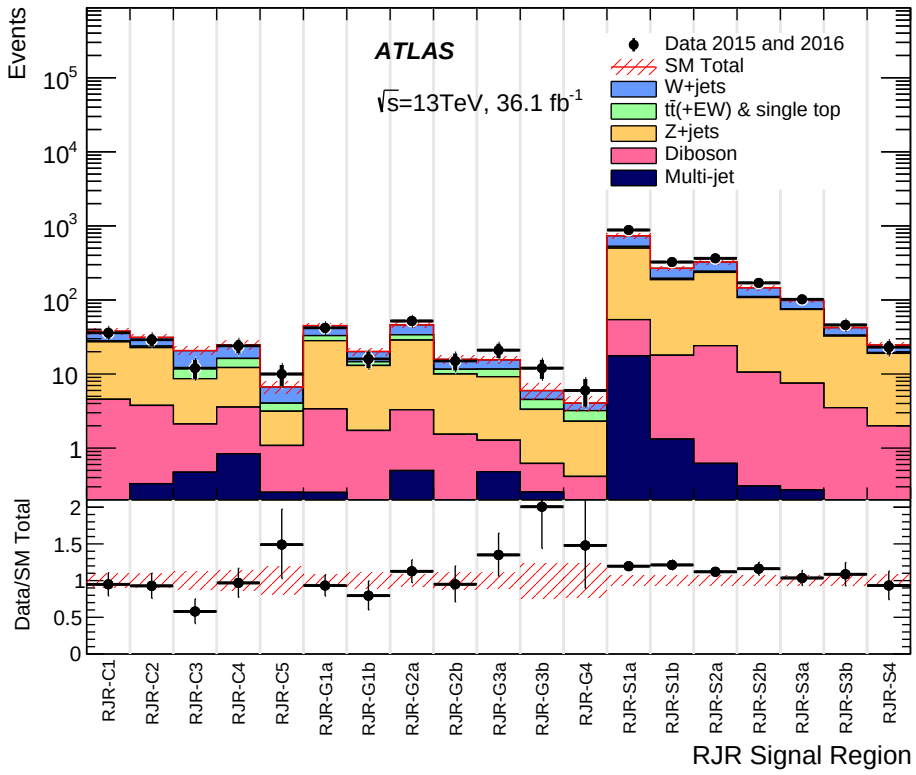

(a)

Figure 11.6: Comparison of the observed and expected event yields as a function of signal region. The background predictions are those obtained from the background-only fits, presented in Table 11.1, 11.2 and 11.3. The lower panel shows the ratio of observed data yields to the total predicted background. The hatched (red) error bands indicate the combined experimental and MC statistical uncertainties.

11.2 Exclusion Reach

We started by defining signal regions, control regions and validation regions for our analysis then included systematic uncertainties and and the event yields and upper limits on the observed and expected supersymmetric signals. Using all of this information, the model-dependent fits in all the SRs are used to set limits on specific classes of SUSY models using asymptotic formulae. The final observed and expected 95% CL exclusion limits are obtained from the signal regions with the best expected CLs value. Fine structures in the limit lines arise due to transitions between best SR's which then also have an impact on the interpolations between grid points.

The limits plots shown below have Recursive Jigsaw exclusion limits drawn in conjunction with M_{eff}-based search. They are combined such that the final observed and expected 95% CL exclusion limits are obtained from the signal regions with the best expected CL_S value. The blue dashed lines show the expected limits at 95% CL, with the light (yellow) bands indicating the 1σ excursions due to experimental and background-only theoretical uncertainties. Observed limits are indicated by medium dark (maroon) curves where the solid contour represents the nominal limit, and the dotted lines are obtained by varying the signal cross-section by the renormalization and factorization scale and PDF uncertainties. Results are compared with the observed limits obtained by the previous ATLAS searches with one or no leptons, jets and missing transverse momentum. In Figure 11.7, limits are shown for two classes of simplified models in which only direct production of first- and second-generation mass-degenerate squark or gluino pairs are considered. Limits are obtained by using the signal region with the best

expected sensitivity at each point. In these simplified-model scenarios, the upper limit of the excluded first- and second-generation squark mass region is 1.55 TeV assuming massless $\tilde{\chi}_1^0$, as obtained from the signal region RJR-S4. The observed exclusion limit is worse than the expected limit in the region with squark ($\tilde{\chi}_1^0$) mass of 1 TeV (500 GeV). The corresponding limit on the gluino mass is 2.03 TeV. The best sensitivity in the region of parameter space where the mass difference between the squark (gluino) and the lightest neutralino is small, is obtained from the dedicated RJR-C signal regions. In these regions with very compressed spectra and where the mass difference is less than 50 GeV, squark (gluino) masses up to 650 GeV (1 TeV) are excluded. In Figure 11.7(b), the compressed-mass region with a gluino mass below 700 GeV is fully excluded by this analysis; small deviations in the exclusion contour in this region, suggesting non-excluded areas, are due to interpolation effects.

In Figure 11.8, limits are shown for pair-produced first- and second-generation squarks or gluinos each decaying via an intermediate $\tilde{\chi}_1^{\pm}$ to a quark (for squarks) or two quarks (for gluinos), a W boson and a $\tilde{\chi}_1^0$. Two sets of models of mass spectra are considered for each case. One is with a fixed $m_{\tilde{\chi}_{\pm}^1} = (m_{\tilde{q}} + m_{\tilde{\chi}_1^0})/2$ (or $(m_{\tilde{g}} + m_{\tilde{\chi}_1^0})/2$), the other is with a fixed $m_{\tilde{\chi}_1^0}$=60 GeV. In the former models with squark pair production, $m_{\tilde{q}}$ up to 1.15 TeV are excluded for a massless $\tilde{\chi}_1^0$, as is $m_{\tilde{g}}$ up to 1.98 TeV with gluino pair production. In the regions with very compressed spectra with mass difference between the gluino (or squark) and $\tilde{\chi}_1^0$ less than 50 GeV, RJR-C signal regions also exclude squark (gluino) masses up to 600 GeV (1 TeV). In the latter models, M_{eff} analysis extend the limits on squark (gluino) masses

up to 1.1 TeV (1.85 TeV) in the regions with small mass difference between the squark (gluino) and $\tilde{\chi}_1^{\pm}$.

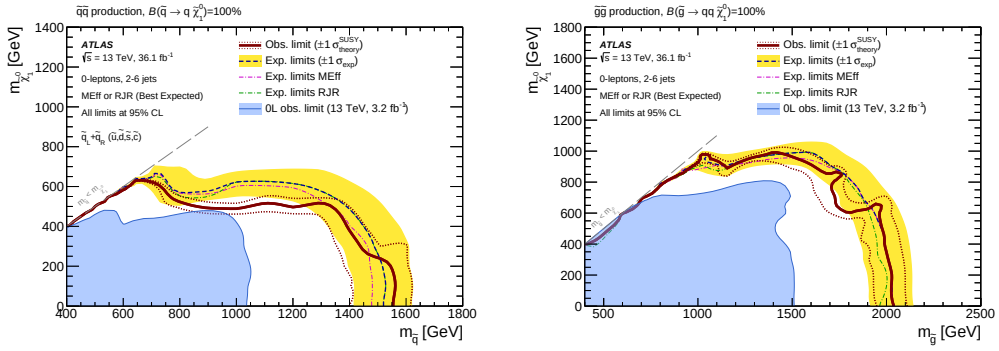

(a) (b)

Figure 11.7: Exclusion limits for direct production of (a) first- and second-generation squark pairs with decoupled gluinos and (b) gluino pairs with decoupled squarks. Gluinos (first- and second-generation squarks) are required to decay to two quarks (one quark) and a neutralino LSP. Exclusion limits are obtained by using the signal region with the best expected sensitivity at each point. Expected limits from the M_{eff}- and RJR-based searches separately are also shown for comparison. The blue dashed lines show the expected limits at 95% CL, with the light (yellow) bands indicating the 1σ excursions due to experimental and background-only theoretical uncertainties. Observed limits are indicated by medium dark (maroon) curves where the solid contour represents the nominal limit, and the dotted lines are obtained by varying the signal cross-section by the renormalization and factorization scale and PDF uncertainties. Results are compared with the observed limits obtained by the previous ATLAS searches with jets, missing transverse momentum, and no leptons.

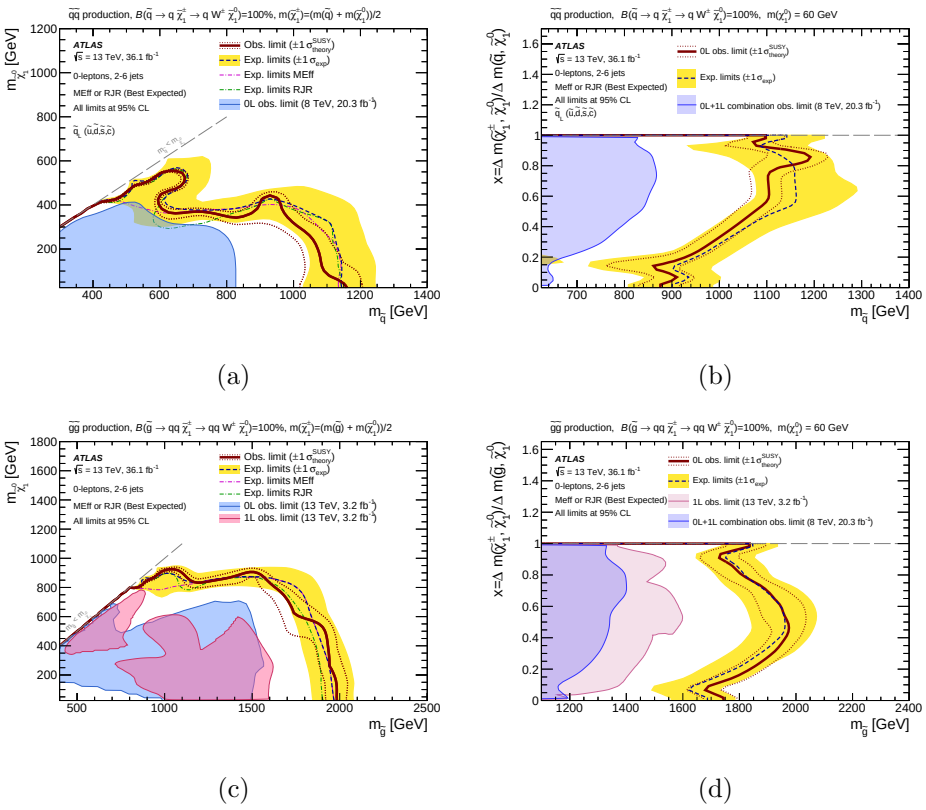

Figure 11.8: Exclusion limits for direct production of (a,b) first- and second-generation left-handed squark pairs with decoupled gluinos and (c,d) gluino pairs with decoupled squarks. Gluinos (first- and second-generation squarks) are required to decay to two quarks (one quark) and an intermediate $\tilde{\chi}_1^{\pm}$, decaying to a W boson and a $\tilde{\chi}_1^0$. Models with (a,c) a fixed $m_{\tilde{\chi}_1^{\pm}} = (m_{\tilde{g}} + m_{\tilde{\chi}_1^0})/2$ (or $(m_{\tilde{q}} + m_{\tilde{\chi}_1^0})/2$) and varying values of $m_{\tilde{g}}$ (or $m_{\tilde{q}}$) and $m_{\tilde{\chi}_1^0}$, and (b,d) a fixed $m_{\tilde{\chi}_1^0} = 60$ GeV and varying values of $m_{\tilde{g}}$ (or $m_{\tilde{q}}$) and $m_{\tilde{\chi}_1^{\pm}}$ are considered.

In Figure 11.9, limits are shown for gluino pair production decaying via an intermediate $\tilde{\chi}_2^0$ to two quarks, a Z boson and a $\tilde{\chi}_1^0$. The mass of the $\tilde{\chi}_1^0$ is set to 1 GeV. In these models, gluino masses below 2.0 TeV are excluded for $\tilde{\chi}_2^0$ masses of $\sim$ 1 TeV, as obtained from the M_{eff} analysis.

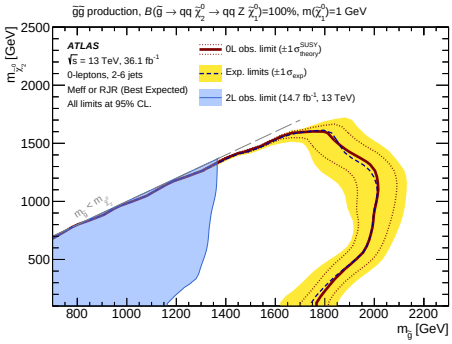

Figure 11.9: Exclusion limits for pair-produced gluinos each decaying via an intermediate $\tilde{\chi}_2^0$ to two quarks, a Z boson and a $\tilde{\chi}_1^0$ for models with a fixed $m_{\tilde{\chi}_1^0} = 1$ GeV and varying values of $m_{\tilde{g}}$ and $m_{\tilde{\chi}_2^0}$. Exclusion limits are obtained by using the signal region with the best expected sensitivity at each point. The blue dashed lines show the expected limits at 95% CL, with the light (yellow) bands indicating the 1σ excursions due to experimental and background-only theoretical uncertainties. Observed limits are indicated by medium dark (maroon) curves where the solid contour represents the nominal limit, and the dotted lines are obtained by varying the signal cross-section by the renormalization and factorization scale and PDF uncertainties. Results are compared with the observed limits obtained by the previous ATLAS search in events containing a leptonically decaying Z boson, jets and missing transverse momentum.

In Figure 11.10, results are presented in the models with mixed decays of intermediate $\tilde{\chi}_1^{\pm}$ and $\tilde{\chi}_2^0$ for squark pair and gluino pair production. The highest limits on the squark mass are 1.34 TeV and on the gluino mass are 2.02 TeV, which are similar to the models with 100% branching fraction for $\tilde{\chi}_1^{\pm}$ ($\tilde{\chi}_2^0$) to a W (Z) boson and $\tilde{\chi}_1^{\pm}$. In Figure 11.10(b), the limits are extended by the M_{eff} analysis in the region with small mass differences between the gluino and $\tilde{\chi}_2^0$.

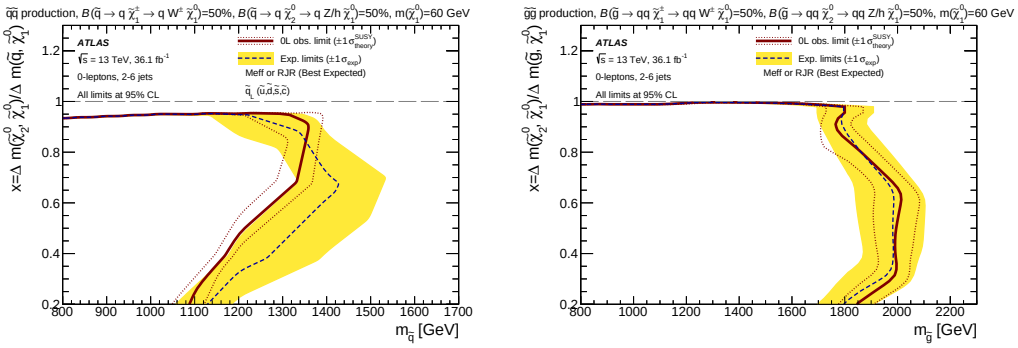

(a) (b)

Figure 11.10: Exclusion limits for direct production of (a) first- and second-generation left-handed squark pairs with decoupled gluinos and (b) gluino pairs with decoupled squarks. Gluinos (first- and second-generation squarks) are required to decay to two quarks (one quark) and a intermediate $\tilde{\chi}_1^{\pm}$ or $\tilde{\chi}_2^0$ with a 50% branching fraction, respectively, with $\tilde{\chi}_1^{\pm}$ decays to a W boson and a $\tilde{\chi}_1^0$, and $\tilde{\chi}_2^0$ decays to a Z or a h boson and $\tilde{\chi}_1^0$. Models with fixed $m_{\tilde{\chi}_1^0} =$ 60 GeV are considered while varying $m_{\tilde{g}}$ (or $m_{\tilde{q}}$) and $m_{\tilde{\chi}_1^0}$. Exclusion limits are obtained by using the signal region with the best expected sensitivity at each point. The blue dashed lines show the expected limits at 95% CL, with the light (yellow) bands indicating the 1σ excursions due to experimental and background-only theoretical uncertainties. Observed limits are indicated by medium dark (maroon) curves where the solid contour represents the nominal limit, and the dotted lines are obtained by varying the signal cross-section by the renormalization and factorization scale and PDF uncertainties.

In Figure 11.11, results are interpreted in simplified pMSSM models assuming only first- and second-generation squarks, gluino and $\tilde{\chi}_1^0$. The $\tilde{\chi}_1^0$ is

assumed to be purely bino. Models with a fixed $m_{\tilde{\chi}_1^0} = 0$, 695, 995 GeV are considered while varying $m_{\tilde{g}}$ and $m_{\tilde{q}}$. In the limit of high squark mass, gluino masses up to 2 TeV are excluded for massless $\tilde{\chi}_1^0$, which is consistent with the simplified models of gluino pair production with decoupled squarks. With a gluino mass of 6 TeV, squark masses up to 2.2 TeV are excluded for a massless $\tilde{\chi}_1^0$, much higher than in the simplified models of squark pair production with decoupled gluinos. This is due to the large cross-section of squark pair production via gluino exchange diagrams.

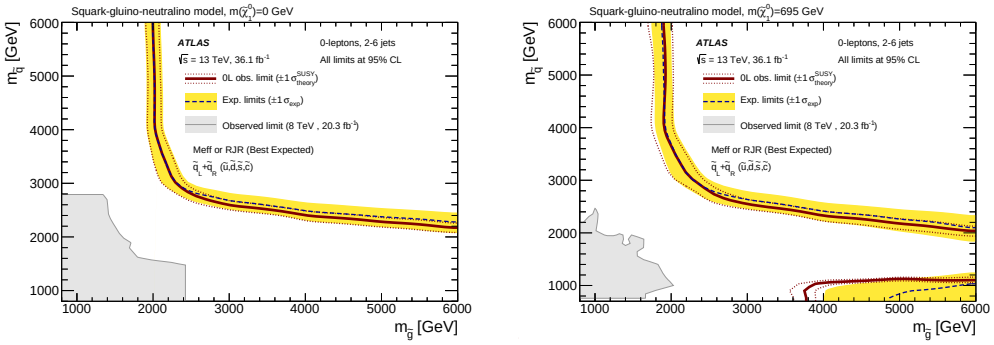

(a) (b)

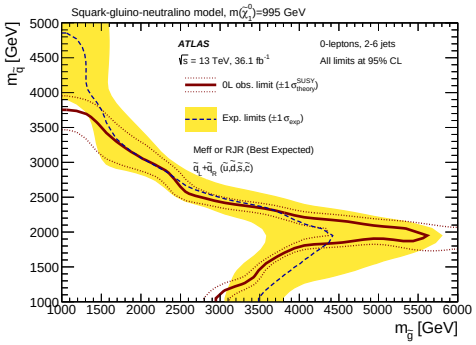

(c)

Figure 11.11: Exclusion limits for inclusive squark–gluino production in pMSSM models with (a) $m_{\tilde{\chi}_1^0}$ = 0 GeV, (b) $m_{\tilde{\chi}_1^0}$ = 695 GeV and (c) $m_{\tilde{\chi}_1^0}$ = 995 GeV varying values of $m_{\tilde{g}}$ and $m_{\tilde{q}}$ and assuming purely bino $\tilde{\chi}_1^0$. Exclusion limits are obtained by using the signal region with the best expected sensitivity at each point. The blue dashed lines show the expected limits at 95% CL, with the light (yellow) bands indicating the 1σ excursions due to experimental and background-only theoretical uncertainties. Observed limits are indicated by medium dark (maroon) curves where the solid contour represents the nominal limit, and the dotted lines are obtained by varying the signal cross-section by the renormalization and factorization scale and PDF uncertainties. Results (a,b) are compared with the observed limits obtained by the previous ATLAS searches with no leptons, jets and missing transverse momentum.

Chapter 12

Conclusion

SUSY is a well motivated theoretical description of nature beyond the SM that can correct for the deficiencies left by it. R-parity conserving supersymmetric models are highly motivated by the experimental evidence supporting no proton decay. R-parity conserving supersymmetric signature produce pair produced particles and a stable weakly interacting particles in the final states.

In this thesis a summary for the search of R-parity conserving supersymmetric quarks and gluons was presented in an all hadronic channel with only jets and missing energy in the final states. This search was performed on the 36.1 fb^{-1} dataset at CM energy $\sqrt{s} = 13$ TeV collected by the ATLAS detector during the p-p collisions done at LHC in 2015 + 2016. The p-p collisions had the highest CM energy ever achieved in a laboratory.

A novel technique called "Recursive Jigsaw" was used to look for SUSY in these channels. "Recursive Jigsaw" is a successor of the Razor and Super-Razor methodology, it uses decay tree topology to resolve every system into it's rest frames and subsequent restframes for the decaying particles. It then

applies a set of inter-changeable *jigsaw rules* to remove the kinematic and combinatoric ambiguities associated with that system. This technique helps us in making educated assumptions about the unknown degrees of freedom of the system and produces more handles/observables to study the weakly interacting particles coming out of the p-p collisions.

The signal regions were divided into three categories depending on the signal studied; the squark regions, the gluino regions and the compressed regions where visible particles (jets) were boosted against the ISR in the system. E_T^{miss} was used as a discriminant here against the high QCD background. The RJ technique compared favourably against the conventional analysis technique, the "M_{eff}" approach. It also produced a better exclusion reach for the compressed signal region than the conventional approach.

Simplified models were used to illustrate the reach of the SUSY signatures. These models use the assumption of a 100% production and branching ratio for the signals. No excesses were seen in any signal regions and model-dependent and model-independent limits were set on the R-parity conserving squark and gluino models.

With this dataset, a large part of the parameter space in the gluino and squark production has been ruled out, especially for the simplified models. However there is a much larger parameter space to be probed for the more sophisticated models. With much higher luminosities for the LHC after the third technical development stop, the promise of SUSY still exists.

References

[1] G. Aad *et al.* [ATLAS Collaboration], "Observation of a new particle in the search for the Standard Model Higgs boson with the ATLAS detector at the LHC," Phys. Lett. B **716**, 1 (2012) [arXiv:1207.7214 [hep-ex]].

[2] T. Schucker, "Higgs-mass predictions," arXiv:0708.3344 [hep-ph].

[3] B. Allanach, "Lectures on Beyond Standard Model Physics",The European Schools of High-Energy Physics (ESHEP) 2018.

[4] G. Gabrielse and D. Hanneke, "New measurement of the electron magnetic moment and the fine structure constant," AIP Conf. Proc. **869**, 68 (2006).

[5] M. Zeman, "Measurement of the Standard Model W+W production cross-section using the ATLAS experiment on the LHC", https://tel.archives-ouvertes.fr/tel-01141822.

[6] F.E. Close, "The cosmic onion", Heinemann Education Books (1983)

[7] D. Griffiths, Introduction to Elementary Particles. Wiley-VCH Verlag GmbH (2008)

[8] C.M.G Lattes et al, Nature, 159, 694 (1947)

[9] C.D Anderson, American Journal of Physics, 29, 825 (1961)

[10] F. Reines and C.L. Cowan Jr, Physical Review 92, 8301, (1953)

[11] M. Gell-Mann, Physical Review, 92, 883 (1953)

[12] D. Cline and C. Rubbia, "Antiproton-proton colliders and Intermediate Bosons," Phys. Today **33N8**, 44 (1980).

[13] G. Aad *et al.* [ATLAS Collaboration], "Evidence for the spin-0 nature of the Higgs boson using ATLAS data," Phys. Lett. B **726** (2013) 120 [arXiv:1307.1432 [hep-ex]].

[14] The Economist, "A timeline of the Standard Model of particle physics", url:https://www.economist.com/graphic-detail/2012/07/04/worth-the-wait

[15] M. Tanabashi *et al.* [Particle Data Group], "Review of Particle Physics," Phys. Rev. D **98**, no. 3, 030001 (2018).

[16] P.A.M Dirac, "The Principals of Qunatum Mechanics", http://digbib.ubka.uni-karlsruhe.de/volltexte/wasbleibt/57355817/57355817.pdf

[17] W. Heisenberg, "Physical Priciples of Quantum Theory", Dover Publications Inc. (1949)

[18] W. Pauli, "General Principles of Quantum Mechanics", Springer-Verlag (1980)

[19] G.t'Hooft, "Under the spell of the gauge principle" , https://doi-org.ezproxy.cern.ch/10.1142/1948

[20] S.L Glashow, "Gauge Theory of Weak and Electromagnetic Interactions", Nuclear Physics, 22, 579 (1961)

[21] S. Weinberg, "Conceptual Foundations of the Unified Theory of Weak and Electromagnetic Interactions," Rev. Mod. Phys. **52**, 515 (1980) [Science **210**, 1212 (1980)].

[22] ATLAS Experiment, "Summary plots from the ATLAS Standard Model physics group", url:https://twiki.cern.ch/twiki/bin/view/AtlasPublic/StandardModelPublicResults

[23] P. Labelle, "Supersymmetry Demystified", New York, NY : McGraw-Hill, (2010)

[24] S. Dawson, "The MSSM and why it works," hep-ph/9712464.

[25] S. P. Martin, "A Supersymmetry primer," Adv. Ser. Direct. High Energy Phys. **21**, 1 (2010) [Adv. Ser. Direct. High Energy Phys. **18**, 1 (1998)] [hep-ph/9709356].

[26] I. J. R. Aitchison, "Supersymmetry and the MSSM: An Elementary introduction," hep-ph/0505105.

[27] J. Conlon, "A Bluffers Guide to Supersymmetry", url:https://www-thphys.physics.ox.ac.uk/people/JosephConlon/LectureNotes/SUSYNotes.pdf

[28] J. L. Hewett *et al.*, "Fundamental Physics at the Intensity Frontier," arXiv:1205.2671 [hep-ex].

[29] S. R. Coleman and J. Mandula, "All Possible Symmetries of the S Matrix," Phys. Rev. **159**, 1251 (1967).

[30] Joseph Conlon, "Lectures on supersymmetry", http://www-thphys.physics.ox.ac.uk/people/JosephConlon/LectureNotes/SUSYNotes.pdf.

[31] R.Dijkgraaf, "Mathematics of M-theory", url:https://www.math.uni-bielefeld.de/ rehmann/ECM/cdrom/3ecm/pdfs/pant3/dijkgr.pdf.

[32] F. Wilczek, "Beyond the standard model: An Answer and twenty questions," hep-ph/9802400.

[33] R. Aaij *et al.* [LHCb Collaboration], "Angular analysis of the $B^0 \to K^{*0}\mu^+\mu^-$ decay using 3 fb^{-1} of integrated luminosity," JHEP **1602** (2016) 104 [arXiv:1512.04442 [hep-ex]].

[34] F. Mahmoudi, "Direct and indirect searches for New Physics," arXiv:1205.3099 [hep-ph].

[35] D. Stockinger, "The Muon Magnetic Moment and Supersymmetry," J. Phys. G **34**, R45 (2007) [hep-ph/0609168].

[36] K. A. Olive, "Searching for supersymmetric dark matter," hep-ph/0208092.

[37] J. A. McFayden, "Searches for supersymmetric partners of third generation quarks and measurement of the $t\bar{t} + Z$ process using the ATLAS detector at the CERN Large Hadron Collider", CERN-THESIS-2013-280

[38] D. I. Kazakov, "Introduction to SUSY and SUSY phenomenology", Dubna International School of Advanced Theoretical Physics (2011) url:http://theor.jinr.ru/ diastp/summer11/lectures/Kazakov-4.pdf

[39] T. Gleisberg, S. Hoeche, F. Krauss, M. Schonherr, S. Schumann, F. Siegert and J. Winter, "Event generation with SHERPA 1.1," JHEP **0902**, 007 (2009) [arXiv:0811.4622 [hep-ph]].

[40] R. Garoby, "Plans for upgrading the CERN proton accelerator complex," J. Phys. Conf. Ser. **110**, 112003 (2008).

[41] "LHC Design Report Volume I The LHC Main Ring", 10.5170/CERN-2004-003-V-1

[42] ATLAS Experiment−Public Results, "LuminosityPublicResultsRun2".

[43] J. Stahlman, "Commissioning and Performance of the ATLAS Transition Radiation Tracker with First High Energy pp and Pb-Pb collisions at LHC," ATL-INDET-PROC-2011-005, ATL-COM-INDET-2011-055.

[44] G. Aad *et al.* [ATLAS Collaboration], "Expected Performance of the ATLAS Experiment - Detector, Trigger and Physics," arXiv:0901.0512 [hep-ex].

[45] J. Alison, "The Road to Discovery : Detector Alignment, Electron Identification, Particle Misidentification, WW Physics, and the Discovery of the Higgs Boson," CERN-THESIS-2012-295.

[46] G. Aad *et al.* [ATLAS Collaboration], "Muon reconstruction performance of the ATLAS detector in protonproton collision data at $\sqrt{s}$ =13 TeV," Eur. Phys. J. C **76**, no. 5, 292 (2016) [arXiv:1603.05598 [hep-ex]].

[47] The ATLAS Collaboration, "Electron reconstruction and identification in the ATLAS experiment using the 2015 and 2016 LHC protonproton collision data at $\sqrt{s} = 13$ TeV", ATL-COM-PHYS-2018-436

[48] A. M. Sirunyan *et al.* [CMS Collaboration], "Performance of reconstruction and identification of τ leptons decaying to hadrons and ν_τ in pp collisions at $\sqrt{s} = 13$ TeV," JINST **13**, no. 10, P10005 (2018) [arXiv:1809.02816 [hep-ex]].

[49] M. Rendel, "Search for Supersymmetry in Multileptonic Final States with collimated τ pairs with the ATLAS detector at the LHC", CERN-THESIS-2018-061

[50] G. Aad *et al.* [ATLAS Collaboration], "Measurement of the inclusive isolated prompt photon cross section in *pp* collisions at $\sqrt{s} = 7$ TeV with the ATLAS detector," Phys. Rev. D **83**, 052005 (2011) [arXiv:1012.4389 [hep-ex]].

[51] S. Batista et al., " Determination of jet calibration and energy resolution in proton-proton collisions at $\sqrt{s} = 8$ TeV using the ATLAS detector", ATL-COM-PHYS-2015-1086.

[52] T. J. Khoo, "The hunting of the squark : Experimental strategies in the search for supersymmetry at the Large Hadron Collider," CERN-THESIS-2013-037

[53] The ATLAS Collaboration, "Selection of jets produced in $\sqrt{s} = 13$ TeV proton-proton collisions with the ATLAS detector", To be submitted to: Eur. Phys. J. C

[54] [ATLAS Collaboration], "Performance of the ATLAS Secondary Vertex b-tagging Algorithm in 7 TeV Collision Data," ATLAS-CONF-2010-042.

[55] The ATLAS Collaboration, "Calibration of light-flavour b-jet mistagging rates using ATLAS proton-proton collision data at $\sqrt{s} = 13$ TeV", ATLAS-CONF-2018-006

[56] The ATLAS Collaboration, "E_T^{miss} performance in the ATLAS detector using the 2015+2016 LHC pp Collisions", ATLAS-CONF-2018-023

[57] G. Aad *et al.* [ATLAS Collaboration], "Performance of Missing Transverse Momentum Reconstruction in Proton-Proton Collisions at 7 TeV with ATLAS," Eur. Phys. J. C **72**, 1844 (2012) [arXiv:1108.5602 [hep-ex]].

[58] The ATLAS Collaboration, "ATLAS event at 13 TeV- First stable beam, 3 June 2015 - run: 266904", url:https://cds.cern.ch/record/2022598

[59] ATLAS Experiment, "Fact Sheet", url:http://atlasexperiment.org/fact-sheets-1-view.html

[60] A. Krasznahorkay [ATLAS Collaboration], "The evolution of the Trigger and Data Acquisition System in the ATLAS experiment," J. Phys. Conf. Ser. **523**, 012019 (2014).

[61] P. H. Beauchemin, "Real time data analysis with the ATLAS Trigger at the LHC in Run-2," arXiv:1806.08475 [hep-ex].

[62] ATLAS Experiment, "AthenaDevelopersGuide", url:http://www.lnf.infn.it/gatti/MANUALI/AthenaDeveloperGuide−8.0.0−draft.pdf

[63] C. Ay *et al.*, "Monte Carlo generators in ATLAS software," J. Phys. Conf. Ser. **219**, 032001 (2010).

[64] E. Schopf, "Search for Higgs boson decay to bottom and charm quarks", CERN-THESIS-2018-145

[65] J. C. Collins, D. E. Soper and G. F. Sterman, "Factorization for Short Distance Hadron - Hadron Scattering," Nucl. Phys. B **261**, 104 (1985).

[66] P. Skands, "Introduction to QCD," arXiv:1207.2389 [hep-ph].

[67] ATLAS Experiment, "ATLAS computing workbook".

[68] R. Jansky, "The ATLAS Fast Monte Carlo Production Chain Project," J. Phys. Conf. Ser. **664**, no. 7, 072024 (2015).

[69] A. Barr and G.Lester, "A Review of the Mass Measurement Techniques proposed for the Large Hadron Collider", J.Phys.G37:123001,2010

[70] Partha Konar et al," $\sqrt{s_{\min}}$ a global inclusive variable for determining the mass scale of new physics in events with missing energy at the LHC", JHEP03(2009)085

[71] D. Kim, K. T. Matchev, F. Moortgat and L. Pape, "Testing Invisible Momentum Ansatze in Missing Energy Events at the LHC," JHEP **1708**, 102 (2017) [arXiv:1703.06887 [hep-ph]].

[72] C. G. Lester and D. J. Summers, "Measuring masses of semiinvisibly decaying particles pair produced at hadron colliders," Phys. Lett. B **463**, 99 (1999) [hep-ph/9906349].

[73] A. J. Barr, T. J. Khoo, P. Konar, K. Kong, C. G. Lester, K. T. Matchev and M. Park, "Guide to transverse projections and mass-constraining variables," Phys. Rev. D **84**, 095031 (2011) [arXiv:1105.2977 [hep-ph]].

[74] G. Arnison et al., UA1 Collaboration, Phys. Lett.122B (1983) 103, Phys. Lett.129B (1983) 273

[75] P. Konar, K. Kong, K. T. Matchev and M. Park, "Superpartner Mass Measurement Technique using 1D Orthogonal Decompositions of the Cambridge Transverse Mass Variable M_{T2}," Phys. Rev. Lett. **105**, 051802 (2010) [arXiv:0910.3679 [hep-ph]].

[76] A. Barr, C. Lester and P. Stephens, "m(T2): The Truth behind the glamour," J. Phys. G **29**, 2343 (2003) [hep-ph/0304226].

[77] D. R. Tovey, "On measuring the masses of pair-produced semi-invisibly decaying particles at hadron colliders," JHEP **0804**, 034 (2008) [arXiv:0802.2879 [hep-ph]].

[78] M. Serna, "A Short comparison between m(T2) and m(CT)," JHEP **0806**, 004 (2008) [arXiv:0804.3344 [hep-ph]].

[79] G. Polesello and D. R. Tovey, "Supersymmetric particle mass measurement with the boost-corrected contransverse mass," JHEP **1003**, 030 (2010) [arXiv:0910.0174 [hep-ph]].

[80] K. T. Matchev and M. Park, "A General method for determining the masses of semi-invisibly decaying particles at hadron colliders," Phys. Rev. Lett. **107**, 061801 (2011) [arXiv:0910.1584 [hep-ph]].

[81] W. S. Cho, J. E. Kim and J. H. Kim, "Amplification of endpoint structure for new particle mass measurement at the LHC," Phys. Rev. D **81**, 095010 (2010) [arXiv:0912.2354 [hep-ph]].

[82] A. J. Barr, C. Gwenlan, C. G. Lester and C. J. S. Young, "A comment on 'Amplification of endpoint structure for new particle mass measurement at the LHC'," Phys. Rev. D **83**, 118701 (2011) [arXiv:1006.2568 [hep-ex]].

[83] M. M. Nojiri, Y. Shimizu, S. Okada and K. Kawagoe, "Inclusive transverse mass analysis for squark and gluino mass determination," JHEP **0806**, 035 (2008) [arXiv:0802.2412 [hep-ph]].

[84] G. L. Bayatian *et al.* [CMS Collaboration], "CMS technical design report, volume II: Physics performance," J. Phys. G **34**, no. 6, 995 (2007).

[85] C. Lester and A. Barr, "MTGEN: Mass scale measurements in pair-production at colliders," JHEP **0712**, 102 (2007) [arXiv:0708.1028 [hep-ph]].

[86] M. R. Buckley, J. D. Lykken, C. Rogan and M. Spiropulu, "Super-Razor and Searches for Sleptons and Charginos at the LHC," Phys. Rev. D **89**, no. 5, 055020 (2014) [arXiv:1310.4827 [hep-ph]].

[87] D. J. Bullock, "Searches for Supersymmetric Particles with the ATLAS Detector Using Boosted Decay Tree Topologies," CERN-THESIS-2016-096.

[88] P. Jackson and C. Rogan, "Recursive Jigsaw Reconstruction: HEP event analysis in the presence of kinematic and combinatoric ambiguities," Phys. Rev. D **96**, no. 11, 112007 (2017) [arXiv:1705.10733 [hep-ph]].

[89] B. Abeloos et al. "Search for squarks and gluinos with the ATLAS detector in final states with jets and missing transverse momentum at $\sqrt{s} = 13$ TeV: supporting documentation" ATL-COM-PHYS-2016-1518.

[90] ATLAS Experiment−Public Results, Summary plots from the ATLAS Supersymmetry physics group, https://atlas.web.cern.ch/Atlas/GROUPS/PHYSICS/CombinedSummaryPlots/SUSY/

[91] P. Jackson, C. Rogan and M. Santoni, "Sparticles in motion: Analyzing compressed SUSY scenarios with a new method of event reconstruction," Phys. Rev. D **95**, no. 3, 035031 (2017) [arXiv:1607.08307 [hep-ph]].

[92] T. Cohen, T. Golling, M. Hance, A. Henrichs, K. Howe, J. Loyal, S. Padhi and J. G. Wacker, "SUSY Simplified Models at 14, 33, and 100 TeV Proton Colliders," JHEP **1404**, 117 (2014) [arXiv:1311.6480 [hep-ph]].

[93] C. S. Rogan *et al.* [ATLAS Collaboration], "Search for squarks and gluinos in final states with jets and missing transverse momentum using 36 fb−1 of $\sqrt{s} = 13$ TeV pp collision data with the ATLAS detector", ATLAS-COM-CONF-2017-020

[94] M. Aaboud *et al.* [ATLAS Collaboration], "Jet energy scale measurements and their systematic uncertainties in proton-proton collisions at $\sqrt{s} = 13$ TeV with the ATLAS detector," Phys. Rev. D **96**, no. 7, 072002 (2017) [arXiv:1703.09665 [hep-ex]].

[95] G. Aad *et al.* [ATLAS Collaboration], "Jet energy measurement with the ATLAS detector in proton-proton collisions at $\sqrt{s} = 7$ TeV," Eur. Phys. J. C **73**, no. 3, 2304 (2013) [arXiv:1112.6426 [hep-ex]].

[96] G. Aad *et al.* [ATLAS Collaboration], "Measurements of top quark pair relative differential cross-sections with ATLAS in pp collisions at $\sqrt{s} = 7$ TeV," Eur. Phys. J. C **73**, no. 1, 2261 (2013) [arXiv:1207.5644 [hep-ex]].

[97] The ATLAS collaboration [ATLAS Collaboration], "Jet mass reconstruction with the ATLAS Detector in early Run 2 data," ATLAS-CONF-2016-035.

[98] M. Baak, G. J. Besjes, D. Cte, A. Koutsman, J. Lorenz and D. Short, "HistFitter software framework for statistical data analysis," Eur. Phys. J. C **75**, 153 (2015) [arXiv:1410.1280 [hep-ex]].